Doctoral theses at NTNU, 2020:86

Muhammad Zeeshan Khalid

Atomistic modeling of Fe-Al and α-AlFeSi intermetallic compound interfaces

Doctoral thesis

Muhammad Zeeshan Khalid

ISBN ISBN 978-82-326-4524-4 (printed ver.)
ISBN ISBN 978-82-326-4525-1 (electronic ver.)
ISSN 1503-8181

NTNU
Norwegian University of
Science and Technology

Doctoral theses at NTNU, 2020:86

NTNU
Norwegian University of Science and Technology
Thesis for the Degree of
Philosophiae Doctor
Faculty of Natural Sciences
Department of Materials Science and Engineering

NTNU
Norwegian University of
Science and Technology

NTNU

Muhammad Zeeshan Khalid

Atomistic modeling of Fe-Al and α-AlFeSi intermetallic compound interfaces

Thesis for the Degree of Philosophiae Doctor

Trondheim, March 2020

Norwegian University of Science and Technology
Faculty of Natural Sciences
Department of Materials Science and Engineering

NTNU
Norwegian University of
Science and Technology

NTNU
Norwegian University of Science and Technology

Thesis for the Degree of Philosophiae Doctor

Faculty of Natural Sciences
Department of Materials Science and Engineering

ISBN ISBN 978-82-326-4524-4 (printed ver.)
ISBN ISBN 978-82-326-4525-1 (electronic ver.)
ISSN 1503-8181

Doctoral theses at NTNU, 2020:86

Printed by NTNU Grafisk senter

To my brother, sisters and parents

First researcher in a lab: A model showing Homo erectus, earliest human species known to have control on fire. From inside the National Museum of Mongolian History in Ulaanbaatar, Mongolia. Source: http://www.defenseimagery.mil; VIRIN: 090812-M-7376M-073

Abstract

The joining of aluminum and steel has been considered an efficient solution for building light-weight technology, particularly in the automotive, aerospace and shipbuilding industries. It is an immense challenge to join these materials together due to the significant differences in the physical and chemical properties of aluminum and steel. The development of intermetallic compound (IMC) layers has a huge impact on the strength of the aluminum-steel joint. The development of IMCs at the aluminum and steel joint is greatly influenced by the welding methodology and temperature reached during the welding process. It is thermodynamically possible to develop certain IMCs depending on the composition and phase diagram of aluminum and steel alloys. For this reason, understanding the mechanical nature of the IMCs is pivotal to improve the welding methodologies.

In this Ph.D. project, atomistic simulations were performed on Fe_2Al_5, Fe_4Al_{13} and α-AlFeSi bulk and interface structures. We started with the construction of atomistic bulk structures of Fe_2Al_5 and Fe_4Al_{13} and calculated the mechanical properties using density functional theory (DFT) calculations. A comparative study was performed to identify the mechanical behavior of these compounds. Moreover, comparisons were also made with other experimental, semi-empirical and ab-initio methods to test the reliability of the calculations.

Due to the complex nature and large atomic structures of Fe-Al IMCs, using ab-initio methods could be very computationally expensive. To make computational calculations fast and accurate, a semi-empirical potential based method has also been used in this work. The main objective of this study was to test the reliability of modified embedded atoms method (MEAM) potentials and suitability for finding good initial structures for Fe-Al interfaces. To test the reliability of the MEAM calculations for Fe-Al compounds, a comprehensive comparative ana-

lysis was made based on the structural and mechanical properties with DFT, experiments and other classical and semi-empirical methods. Although the comparison of structural properties corresponded well with other methods, the mechanical properties showed a huge difference as compared to experiments and DFT. It was concluded that MEAM and semi-empirical methods are not reliable for inferring mechanical features of Fe-Al IMCs. However, MEAM was found to be reasonable for finding good initial guesses for the Fe-Al interface structures.

After the bulk calculations, a systematic study was performed to identify the virtual tensile and shear strengths of Fe-Al and α-AlFeSi interfaces using DFT. Interface structures were optimized using the fast inertial relaxation engine (FIRE), which was very successful in optimizing these complex interfaces with a large number of atoms. After the optimization of the interface structures, virtual tensile and shear strength calculations were performed. An extended version of the so-called Universal Binding Energy relation (UBER) was used to fit the energy-displacement curve for virtual tensile strength and a Fourier series for the virtual shear strength predictions. Based on the virtual tensile strength calculations, the Fe_2Al_5 // Fe interface showed the highest strength, whereas the Al // α-AlFeSi and Al // Fe_4Al_{13} interfaces showed the lowest virtual tensile strength. Moreover, a charge depletion zone was found on the second layer of the Fe_4Al_{13} side in the Al // Fe_4Al_{13} interface structure, which indicated a low strength zone, and practically becoming very detrimental for the joint strength of aluminum and steel. In terms of virtual tensile strength, the Fe_2Al_5 // Fe interface showed the highest tensile strength followed by Fe_4Al_{13} // Fe_2Al_5, α-AlFeSi // Fe_4Al_{13}, Al // α-AlFeSi and Al // Fe_4Al_{13}. Moreover, Fe_2Al_5 // Fe showed the lowest virtual shear strength followed by Al // α-AlFeSi, Al // Fe_4Al_{13}, Fe_4Al_{13} // Fe_2Al_5 and α-AlFeSi // Fe_4Al_{13}. The energy-displacement curve provided an opportunity to explore the brittle/ductile failure mechanism of interface structures. The interfacial brittle/ductile failure mechanism was characterized by the width of the instability region. By taking Al as a baseline, which showed the largest width of the instability region, all interface structures showed a brittle failure. However, α-AlFeSi // Fe_4Al_{13} was found to be the least brittle and Fe_2Al_5//Fe the most brittle interface structure.

List of Included Publications

Paper I
Khalid MZ, Friis J, Ninive PH, Marthinsen K and Strandlie A,"DFT calculations based insight into bonding character and strength of Fe_2Al_5 and Fe_4Al_{13} intermetallics at Al-Fe joints," *Procedia Manufacturing 15,* vol. 15, pp. 1407-1415, 2018.

Paper II
Khalid M. Z., Friis J., Ninive P. H., Marthinsen K., Strandlie A. (2019). Modified embedded atom method potential for Fe-Al intermetallic mechanical strength: A comparative analysis of atomistic simulations, Pre-print

Paper III
Khalid M. Z., Friis J., Ninive P. H., Marthinsen K., Strandlie A. (2019). Ab-initio study of atomic structure and mechanical behaviour of Al/Fe intermetallic interfaces, Computational Material Science, 174 (2020): 109481.

Paper IV
Khalid M. Z., Friis J., Ninive P. H., Marthinsen K., Ringdalen I.G., Strandlie A. (2019). First-principles study of tensile and shear strength of an Fe_2Al_5//Fe interface, Submitted to Modelling and Simulation in Materials Science and Engineering.

Paper V
Khalid M. Z., Friis J., Ninive P. H., Marthinsen K., Strandlie A. (2019). "First-principles study of tensile and shear strength of α-AlFeSi // Fe_4Al_{13} and Fe_2Al_5 // Fe_4Al_{13} intermetallic interfaces, Aimed for Computational Materials Science.

Appendix A
Khalid MZ, Friis J, Ninive PH, Marthinsen K and Strandlie A,"A First-Principles

Study of the Al (001)/Fe(0-11) Interface," *Materials Science Forum,* vol. 941, 2018.

Preface

This thesis is submitted in partial fulfillment of the requirements for the degree of Philosophiae Doctor at the Faculty of Natural Sciences of the Norwegian University of Science and Technology (NTNU), Norway. The doctoral thesis concludes my research work from October 2016 to October 2019.

The majority of the research work presented in this Ph.D. thesis has been conducted at NTNU in Gjøvik. I have spent one semester at NTNU in Trondheim from January 2017 to June 2017. The Ph.D. research was supported by the Center for Research-based Innovation SFI Manufacturing and Norwegian Research Council under the contract number, 237900, Norway.

The thesis consists of two parts. The first part provides an overview of the research field I have been working on during my Ph.D. studies as well as a brief summary of the contributions to the corresponding fields. The second part includes the research papers underpinning this thesis.

Acknowledgments

This thesis could not have been possible without the tremendous help and guidance which I got from my supervisors. Many thanks to Prof. Are Strandlie, who provided me an opportunity to work on this project, and helped me throughout my PhD. I am very thankful to Jesper Friis, who guided me at every step. His constructive criticism not only helped me to move in the right direction, but also allowed me to deepen my knowledge. Many thanks to Per Harald Ninive and Prof. Knut Marthinsen for their valuable contributions throughout my PhD project.

Many thanks to Ahmed Kedir for helping in Python coding, Tina Bergh for providing fancy TEM images and useful discussions about our projects. Siri Marthe for the nice discussions about the welding methodologies and Simen Nut Eliasson and Inga Ringdalen for helping me in performing molecular dynamic simulations during my stay in Trondheim.

Haris Ahmad for being my good friend, apartment mate and travel buddy and special thanks for helping me to settle in Gjøvik at the start of my PhD. Mohib for all the delicious food, which I ate at his place. It was totally awesome. All the amazing people of Computer science at NTNU in Gjøvik for the nice lunches. You all made my stay in Gjøvik memorable.

Thanks to all the lovely people and friends at NTNU in Gjøvik, who made me feel at home, and to everyone at NTNU in Trondheim, who made my stay in Trondheim enjoyable.

Muhammad Zeeshan Khalid
November 2019, Gjøvik

Contents

List of Figures

List of Abbreviations

ATK Atomistix toolkit

BCC Body centered cubic

CG Conjugate gradient

DFT Density functional theory

E_{XC} Exchange correlation energy

FCC Face centered cubic

FEM Finite element method

FIRE Fast inertial relaxation engine

GGA Generalized gradient approximation

IMC Intermetallic compound

LBFGS Limited-memory Broyden-Fletcher-Goldfarb-Shanno

LDA Local density approximation

MD Molecular dynamics

MEAM Modified embedded atom method

OR Orientation relationship

PBE Purdew-Burke-Ernzerhof

RGS Rigid grain shift

TEM Transmission electron microscopy

UBER Universal binding energy relation

VASP Vienna ab-initio simulation package

VRH Voigt-Reuss-Hill approximation

Part I

Overview of Research Field

Chapter 1

Motivation

> "Somewhere, something incredible is waiting to be known."
>
> Carl Sagan (1934-1996)

1.1 Introduction

Owing to the growing environmental pressure to reduce the weight of vehicles, there is considerable interest in the production of more mass-efficient multi-material structures by combining aluminum and steel in advanced automotive construction. [3] [4] [5] [6] [7]. Unfortunately, conventional fusion welding processes do not currently meet industrial requirements for dissimilar metal joining. This is primarily because of the high rate of intermetallic reactions occurring in the liquid phase, which further leads to poor properties and in particular low joint fracture toughness [3] [4] [5]. To tackle this problem many different welding methods have been developed, and controlling of intermetallic layers has been one of the critical tasks to be undertaken. The underlying reason is the brittle nature of the continuous IMC interface layers that severely affect the joints fracture energy if becoming greater than $\sim$100 nm thick [4] [5] [6] [7].

Various methods and studies have been proposed for joining these materials together, including fusion welding (e.g., resistance spot welding, resistance seam welding, arc welding) [8], solid-state bonding (e.g., explosive welding, friction welding, electromagnetic welding, roll bonding, diffusion bonding) [9], brazing (e.g., burner brazing, arc brazing, laser brazing) [10], mechanical joining (e.g., self-pierce riveting, flow drill screw, blind riveting) [11] and adhesive bonding

[12, 13]. For any method that requires high temperatures, a brittle layer of different kinds of Fe-Al IMCs present at the joint makes it difficult to obtain the desired joint strength. Although solid-state welding techniques can suppress the formation of Fe-Al IMCs at a joint due to low temperature, these methods can not completely limit the formation of IMCs and can only produce Fe-Al joints with limited strength.

It has been reported that the thickness of an Fe-Al IMC layer formed in a brazed interface can be limited to less than 10 μm, which is considered as the critical thickness for obtaining Fe-Al joints with good mechanical strength [14]. Analyses of the Fe-Al joints suggest that the micro-structures and distribution of the Fe-Al IMCs at the interface are dependent on the heat input and play an important role in determining the mechanical and/or corrosion behavior of the joints [15, 16]. In general, most of the experimental and theoretical studies on Fe-Al IMCs focus on the following issues, (i) heat input and thickness of the IMC layer [17] (ii) role played by the welding methodology [18, 19] (iii) tensile and shear strength of IMC layers at the joint [12] and (iv) extended heat treatment [20–22].

There is a wealth of experimental literature available reporting the thermodynamics of IMCs in the Fe-Al system. It is possible thermodynamically to produce a range of IMCs in the Fe-Al system [23, 24]. Therefore, it is quintessential to understand the basic mechanical and interfacial strength of these compounds as basis for better understanding of the choice of the appropriate joining process. The lack of convincing results for the interfacial strength of these compounds is not due to the lack of academic and industrial interests on this crucial subject but more related to the very small thickness of these layers (2.3 ± 0.6 μm) [25], which makes it utmost challenging experimentally to predict the interface strength of these compounds. To overcome this experimental limitation, atomistic simulations can provide important insights into the mechanical strength of Fe-Al interfaces.

So far to our best knowledge, nobody has studied the Fe-Al interfaces through atomistic simulations. The lack of atomistic studies of these interfaces is due to the complexity and large atomic structure of the intermetallic compounds such as Fe_4Al_{13}, α-AlFeSi, and Fe_2Al_5. Thus, it is a great challenge to develop an interface model which is periodic and with a low lattice misfit percentage. Hence, in this work, we are going to develop and study the IMCs interfaces, i.e. the different IMCs that typically form, their bulk properties and the structural and mechanical properties of related interface structures. The main topics of this thesis are described in the next section.

1.2 Main topics

1.2.1 Collaboration

A fundamental success criterion for computational materials science is close collaboration with experimentalists. This work is part of the activities in the Centre for Research based Innovation SFI Manufacturing. In this centre, we have a collaboration with physical metallurgy and TEM Gemini center groups at NTNU in Trondheim. Aluminum and steel have been welded together using a cold-metal transfer technique. To identify the IMCs at the aluminum-steel joint, transmission electron microscopy (TEM) observations were made. Identified IMC layers and their arrangement at the aluminum-steel joint are shown in Fig. 1.1. This work depends mainly on these observations.

1.2.2 Aluminum-steel joint strength

As discussed earlier, the main aim of this work is to predict the strength of the different interfacial structures formed by different IMCs. In this thesis, we develop interfaces according to TEM observations and predict their mechanical strength through density functional theory (DFT) and modified embedded atom method (MEAM) calculations. The calculated results from DFT can be used in finite element simulations (FEM) to estimate the overall mechanical behavior of an Fe-Al welded joint. However, FEM simulations will not be part of this thesis.

1.2.3 Building of complex interface structures

The systems to be studied consist of the following interface structures, (i) Al // Fe_4Al_{13}, (ii) Al // α-AlFeSi, (iii) α-AlFeSi // θ-Fe_4Al_{13}, (iv) θ-Fe_4Al_{13} // η-Fe_2Al_5 and (v) η-Fe_2Al_5 // Fe. Due to the large number of atoms in unit cells of Fe_2Al_5 (14 atoms), Fe_4Al_{13} (101 atoms) and α-AlFeSi (138 atoms), it is very challenging to develop interface structures with a low number of atoms and low lattice misfit. In order to find good lattice matches between different IMCs, a face-to-face matching technique has been implemented and used to predict low-misfit orientation relationships.

1.2.4 Density functional theory

To predict the mechanical and bonding strengths, a wide range of theoretical methodologies have been applied, including semi-empirical and tight-binding atomistic calculation methods [26], thermodynamic models, image models, and ab-initio calculations using Hartree-Fock (HF) and DFT approaches [27]. However, the most authoritative and widely used method is DFT, a method which has been very successful in calculating the electronic and mechanical properties of metals. This

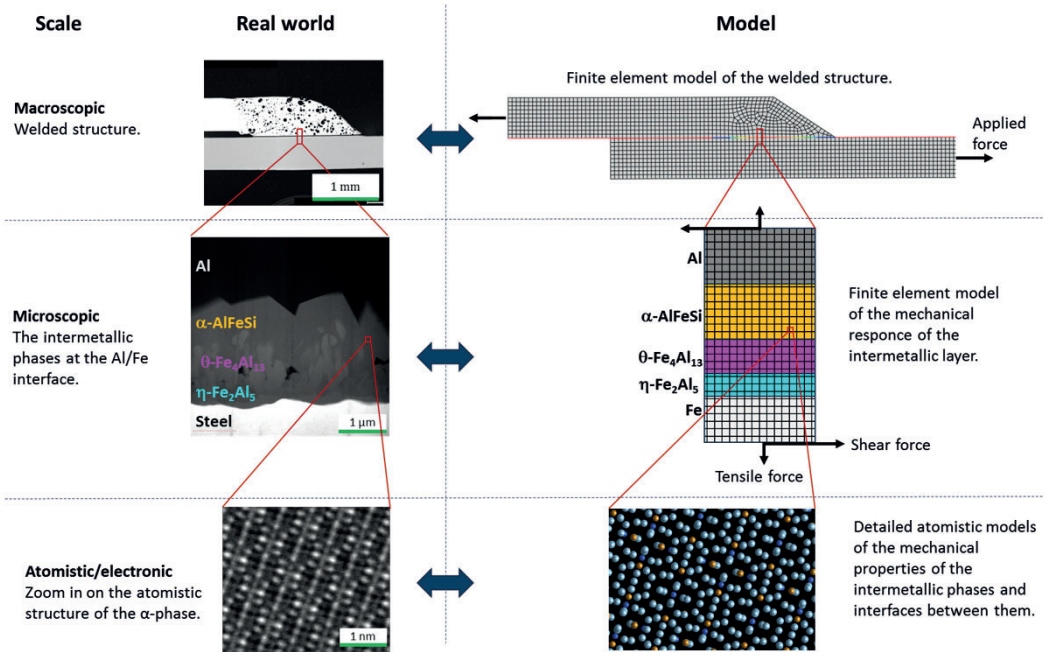

Figure 1.1: Schematic illustration of transition of macroscopic scale to atomic scale and vice versa.

work relies on the DFT methodology. The formalism of DFT will be presented in the next chapters. Since the computational cost directly depends on the number of atoms, it is important to keep the size of the unit cell in a computationally accessible manner. Therefore, material defects such as dislocations and grain boundaries are not considered in this thesis. Wherever possible, results of DFT calculations are compared with other theoretical and experimental studies.

1.2.5 DFT structural optimization

Finding stable equilibrium configurations of atomistic simulations is a major task. This involves the finding of a low potential energy atomic structure from an initial best guess. Finding a low energy configuration is a difficult task due to the large range of potential energy valleys. A variety of well-known optimization methods, such as steepest descent, conjugate gradient (CG), quasi-Newton or truncated Newton methods, Newton-Raphson, and the Fast Inertia Relaxation Engine (FIRE) [2, 28–30] are available for solving this problem. Different optimization algorithms are taken into consideration in this thesis, and some of them are found to be successful in optimizing large interface structures.

1.3 Open research question in Fe-Al welding

In order to improve and develop strategy for welding techniques, there is a need for improved understanding about the effect of the individual Fe-Al IMCs and their interfaces on the mechanical response of welded Fe-Al joints. This understanding is very challenging to get through experiments only due to the small thickness of IMC layers. There is therefore a need of theoretical simulations of these interfaces using realistic models based on atom-resolved TEM techniques, like high-angle annular dark-field scanning transmission electron microscopy (HAADF-STEM) that can contribute to build up such understanding. The aim of this work is to contribute to improved understanding and bridge the gap of missing information. Results obtained from these theoretical calculations will help to understand the basic mechanism and strengths of the individual Fe-Al IMCs and their relevant interfaces, and give indications of which IMCs can be accepted without compromising the overall joint strength and which should possibly be avoided.

1.4 Thesis organization

This thesis consists of two parts. Part 1 is an overview of the research field. This part consists of 4 chapters. The overall motivation and the main themes of this thesis are presented in Chapter 1. Chapter 2 describes the computational methodology and theoretical background of the density functional theory and modified embedded atom method, which were used in this thesis. The general theoretical background about the methodologies from the interface building to the mechanical properties simulations is presented in Chapter 3. In Chapter 4, a summary of the included articles and future perspectives are presented. Part II presents the main articles in the form of published and pre-print manuscript versions.

Chapter 2

Computational Methodology

"Quantum physics thus reveals a basic oneness of the universe."

Erwin Schrödinger (1887-1961)

2.1 The Schrödinger equation

One of the significant advances in the 20th century was the development of quantum mechanics and repeated experimental observations that validated the theory of matter with astonishing accuracy in the universe in which we live.

Let us consider a situation, where we look at the properties of a well-defined collection of atoms. In this scenario, the pivotal concern would be to know their energy and how it changes as atoms move around.

The Schrödinger equation for the electrons becomes:

$$\hat{H}\psi(r_1, r_2, r_3, ...r_N) = E\psi(r_1, r_2, r_3, ...r_N) \tag{2.1}$$

In Eq. (2.1), E is the ground state energy of electrons. The electronic Hamiltonian consists of three terms:

$$\hat{H} = -\frac{\hbar^2}{2m_e}\sum_{i=1}^{N_e}\nabla_i^2 + \sum_{i=1}^{N_e}V_{\text{ext}}(r_i) + \sum_{i=1}^{N_e}\sum_{j>1}U(r_i, r_j) \tag{2.2}$$

In Eq. (2.2), the first term on the right-hand side describes the kinetic energy of

the electrons, while the second and third terms describe the nuclei-electron attraction and electron-electron repulsion respectively. Since the ground-state energy is independent of time, it is called the time-independent Schrödinger equation.

2.1.1 Hartree product

The number of electrons is considerably larger than the number of nuclei since each atom possesses one nucleus and several electrons. An example is CO_2 holding 22 electrons (6+16=22). The full wave function is 66-dimensional (3 dimensions for each electron). Similarly, for a nanocluster of Pb which has 82 electrons per atom (100 atoms—8200 electrons), the Schrödinger equation becomes a 24600-dimensional problem. As a consequence, solving the Schrödinger equation can in practice be very complicated.

It is worth noting that the wave function of a particular set of coordinates cannot be directly observed. Since the electrons cannot be directly observed during the experiment, electrons can not be labeled or identified independently. However, we can measure the probability of N electrons at a particular set of positions $(r_1, r_2, r_3, ...r_N)$ leading to a unique non-interacting electron system with the same electron density, where N is the number of electrons. This electron density serves as the single-electron wave functions. The non-local component of U is taken into account by the kinetic energy of the reference non-interacting electron system. Furthermore, the electron density defines the so-called exchange interaction due to the Hartree-Fock formalism. The residual is defined as the correlation energy (defined as the difference between the true total energy and the Hartree Fock limit). The probability is equal to $\psi(r_1, r_2, r_3, ...r_N)\psi^*(r_1, r_2, r_3, ...r_N)$.

To simplify the many-electrons problem to many one-electron problems, each electron is treated as a point charge in the field of all other electrons. The electron density in terms of single-electron wave functions can then be defined as:

$$n(r) = 2\sum_i \psi_i^*(r)\psi_i(r) \tag{2.3}$$

where the factor 2 is due to electron spin.

2.1.2 Hohenberg–Kohn theorems

Theorem 1

The ground state energy is a unique functional of the electron density: $E[n(r)]$.

This theorem states a one-to-one mapping between the ground-state wave function and the ground-state electron density. Another way to restate the theorem is that the ground state electron density uniquely determines all properties including the

energy and wave function of the ground state.

The consequence of this theorem is that we can solve the Schrödinger equation by finding a function of three spatial variables (the electron density) instead of a function of 3N variables (the wave function). For the nanocluster problem described above the theorem reduces the problem from 24600 dimensions to just 3 dimensions.

Though the first theorem proves that a functional of the electron density exists, it does not say anything about what the functional is. The second theorem defines an important property of the functional.

Theorem 2

The electron density that minimizes the energy of the overall functional is the true ground-state electron density

$$E[n(r)] > E_0[n_0(r)] \tag{2.4}$$

This energy functional can be divided into two parts: (i) Known (ii) Unknown (XC)

$$E[\psi_i] = E_{\text{known}}[\psi_i] + E_{\text{XC}}[\psi_i] \tag{2.5}$$

$$\begin{aligned} E_{\text{known}}[\psi_i] = -\frac{\hbar^2}{2m_e}\sum_i \int \psi_i^* \nabla^2 \psi_i d^3r + \int V(r)n(r)d^3r \\ + \frac{e^2}{2}\int\int \frac{n(r)n'(r)}{r-r'} d^3r d^3r' + E_{\text{ion}} \end{aligned} \tag{2.6}$$

The terms on the right-hand side of Eq. (2.6) are the electron kinetic energies, the Coulomb interaction between electrons and nuclei, the Coulomb interaction between pairs of electrons, and the Coulomb interaction between pairs of nuclei, respectively.

$E_{XC}(\psi_i)$ is the exchange-correlation functional, which includes all quantum mechanical terms. Unfortunately, this functional is unknown, and it needs to be approximated. The two simplest XC-functional approximations are LDA (Local density approximation), and GGA (Generalized gradient approximation) [31].

2.1.3 Kohn-Sham scheme

The Kohn-Sham (KS) equation has the form

$$\left[-\frac{\hbar^2}{2m_e}\nabla^2 + V(r) + V_{\text{H}}(r) + V_{\text{XC}}(r)\right]\psi_i(r) = \epsilon_i(r)\psi_i(r) \tag{2.7}$$

The Kohn-Sham Eq. (2.7) is similar to the Schrodinger Eq. (2.1), and the only difference lies in the absence of summation. This is due to the Kohn-Sham equation

that contains single-electron wave functions only being dependent on three spatial variables.

On the left-hand side of Eq. (2.7) the three potentials V, V_{H}, and V_{XC} appear. The first potential defines the interaction between electrons and atomic nuclei, and the second potential is the Hartree potential given by:

$$V_{\mathrm{H}} = e^2 \int \frac{n(r')}{r - r'} d^3 r' \tag{2.8}$$

This describes the Coulomb repulsion between electrons. The third potential is the exchange-correlation potential. The exact form of this potential is not known, thus we must introduce approximate functional based upon electron density to describe this term. From the above discussion it can be concluded that in order to solve the Kohn-Sham equations, the following steps need to be followed:

1. Define the Hartree potential.
2. To define the Hartree potential we need to know the electron density.
3. To find the electron density, we must know the single-electron wave functions.
4. To know the wave functions we must solve the Kohn-Sham equation.

These steps define above have a circular loop. This circular loop can be broken by treating a problem in an iterative way as shown in Fig. 2.1. The procedure starts from an initial trial electron density, $n(r)$. In the second step, the single-electron wave function is obtained by solving the Kohn-Sham equation. In the third step, the electron density is calculated from the single-electron wave function called $n'(r)$. If the updated $n'(r)$ is similar to the initial electron density $n(r)$, the process is terminated and the true electron ground state is reached. Otherwise, the process begins again from step 2. Obtaining a converged electron density is very challenging for complex and large structures. For this reason, convergence criteria are defined for the updated $n'(r)$.

For the calculations of forces on each ion, it is first assumed that electrons adapt instantaneously to the ionic configuration (Born-Oppenheimer approximation). Now the total energy is a function of the ionic coordinates. Once the spatial distribution of the ions has been determined, the forces can be calculated by using the Hellman-Feynman theorem:

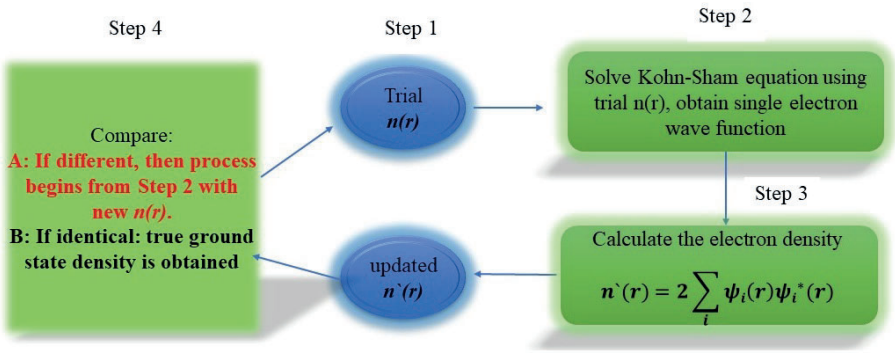

Figure 2.1: Self-consistency scheme for solving the Kohn-Sham equation [1].

$$F_i = -\frac{dE}{dr_I} = - < \psi_i | \frac{\partial \hat{H}}{\partial r_I} | \psi_i > \tag{2.9}$$

where r_I is the ionic distance.

Moving along the steepest descent of ionic forces, the ionic ground state can be calculated. We will then be able to displace ions from an initial state and consequently determine the forces on all other ions, the effective interatomic force constants and vibrational frequencies, etc.

2.1.4 Exchange-correlation functional

According to the KS theorem, the motion of particles can only be described after knowing the exchange-correlation function E_{XC}. The most used approximations are E_{XC} are the local density approximation (LDA) [32] and generalized gradient approximation (GGA) [33].

2.1.5 Local density approximation

The exchange-correlation functional E_{XC} in the LDA can be written as:

$$E_{\text{XC}}[n] = \int n(r)\epsilon_{\text{XC}}(n)d^3r \tag{2.10}$$

where $\epsilon_{\text{XC}}(n)$ is the exchange-correlation energy per particle between electrons in the uniform non-interacting electron gas with a charge density n [34]. Therefore, the local XC potential is defined as:

$$V_{\mathrm{XC}}(r) = \epsilon_{\mathrm{XC}}(n(r)) + n(r)\frac{\partial \epsilon_{\mathrm{XC}}(n)}{\partial n} \tag{2.11}$$

The function ϵ_{XC} is split into two terms: exchange, $\epsilon_{\mathrm{X}}(r)$ and correlation, $\epsilon_{\mathrm{C}}(n)$. The form of the exchange term is given as [35, 36],

$$\epsilon_{\mathrm{X}}(n) = -\frac{3}{4}\left(\frac{3}{\pi}\right)^{\frac{1}{3}} n(r)^{\frac{1}{3}} \tag{2.12}$$

For $\epsilon_{\mathrm{C}}(n)$, there is no analytical expression except for the high and low-density limits [35].

We can obtain the ground-state energy of a system by calculating $V_{\mathrm{XC}}(r)$ from $\epsilon_{\mathrm{XC}}(n)$.

2.1.6 Gradient expansion approximation

LDA has made it possible to apply DFT to many systems and has shown great success in the prediction of material properties. However, this method has also some shortcomings. Due to the high degree of inhomogeneity of the electronic charge density, LDA is not accurate enough to predict many system properties. Kohn-Sham (KS) discussed the solution to this problem in the original paper by adding new terms involving powers of $|\nabla n|$ and $\nabla^2 n$, which is commonly known as the gradient expansion approximation (GEA) [32]. Despite these new modifications, LDA outperformed the GEA method completely due to the inadequate conceptual basis [37].

2.1.7 Generalized gradient approximations

The shortcomings of LDA and GEA have been overcome to a great extent by the generalized gradient approximation (GGA) [38, 39]. In GGA, XC relates to both the charge density n and the electron density gradient $\nabla n(r)$, and is written as:

$$E_{\mathrm{XC}}^{\mathrm{GGA}}[n] = \int f_{\mathrm{XC}}(n(r), |\nabla n(r)|) d^3 r \tag{2.13}$$

This approach has greatly increased the performance and accuracy for the prediction of material properties of transition metals and molecular systems. The form $f_{\mathrm{XC}}(n(r), \nabla n(r))$ can be implemented in several ways. In this work, we use the PBE approach [33].

2.1.8 Simulation package and methodology

All first-principles calculations in this work have been carried out using the Vienna ab-initio simulation package (VASP) [40]. To describe the electron-ion interaction,

the GGA by Perdew, Burke and Ernzerhof (PBE) [33] was employed, and using the Projector Augmented-Wave method (PAW) [41] to smooth the wave functions close to the ion core. The cut-off energy was tuned to the system size so that the total energy difference is less than 1 meV/atom. A k-point sampling by using the Monkhorst-Pack scheme [42] to characterize the energy integration in the first irreducible Brillouin zone was employed. To take into account the magnetic effects of Fe atoms, spin-polarised calculations were performed by defining initial localized magnetic moment of 3 for each individual Fe atom. More details about the calculations can be found in the related papers.

2.2 Modified embedded atom method (MEAM)

A description of MEAM potentials has been published by Baskes et al. [43]. A brief introduction of MEAM potentials will be presented in this section. The core of atomistic simulations is to evaluate the interatomic forces and energy of a system as a function of atomic positions. In MEAM, the total energy of a system can be approximated as the sum of energy contributions of all atoms:

$$E = \sum_{i=1}^{n} F_i(\bar{\rho}_i) + \frac{1}{2}\sum_{i\neq j}^{n} \phi_{ij}(R_{ij}) \tag{2.14}$$

In the above equation F_i is the embedding function, which denotes the energy needed to embed an atom i in a background environment electron density $(\bar{\rho}_i)$ at site i, and $\phi_{ij}(R_{ij})$ is the repulsive pair potential between atoms i and j whose separation is given by R_{ij}. For calculation of the energy of a system, a material-independent form of the two terms given on the right-hand side of Eq. (2.14) should be given.

The embedding function $F_i(\bar{\rho}_i)$ is given as:

$$F_i(\bar{\rho}_i) = A_i E_i^0 \bar{\rho}_i \ln(\bar{\rho}_i) \tag{2.15}$$

Here E_i^0 is the cohesive energy and A_i is the scaling factor of an atom i. The background electron density $\bar{\rho}_i$ at a atom i is dependent on the directionality of bonding and is given by:

$$\bar{\rho}_i = \frac{{\rho_i}^{(0)}}{\rho_i^0} G_i(\Gamma_i) \tag{2.16}$$

where

$$\Gamma_i = \sum_{k=1}^{3} t^{(k)} \left(\frac{{\rho_i}^{(k)}}{{\rho_i}^{(0)}}\right)^2 \tag{2.17}$$

In the above equations, ${\rho_i}^0$ is the background electron density of the equilibrium structure (reference structure) at site i, $t^{(k)}$ are adjustable parameters. $G_i(\Gamma)$ is a function dependent on the element types, and typical expressions for this function are $G(\Gamma) = \sqrt{(1+\Gamma)}$ and $G(\Gamma) = \exp(\frac{\Gamma}{2})$. ${\rho_i}^{(k)}$ is the higher-order background electron densities which are composed of spherically-symmetric ($\rho_i^{(0)}$) and angular ($\rho_i^{(1)}, \rho_i^{(2)}, \rho_i^{(3)}$) partial electron densities, given as:

$$
\begin{aligned}
\rho_i^{(0)} &= \sum_{j\neq i} S_{ij}\rho_j^{\alpha(0)}(R_{ij}) \\
(\rho_i^{(1)})^2 &= \sum_{\alpha}\left[\sum_{j\neq i}\frac{R_{ij}^{\alpha}}{R_{ij}}S_{ij}\rho_j^{\alpha(1)}\right]^2 \\
(\rho_i^{(2)})^2 &= \sum_{\alpha,\beta}\left[\sum_{j\neq i}\frac{R_{ij}^{\alpha}R_{ij}^{\beta}}{R_{ij}^2}S_{ij}\rho_j^{\alpha(2)}\right]^2 - \frac{1}{3}\left[\sum_{j\neq i}S_{ij}\rho_j^{\alpha(2)}(R_{ij})\right]^2 \\
(\rho_i^{(3)})^2 &= \sum_{\alpha,\beta,\gamma}\left[\sum_{j\neq i}\frac{R_{ij}^{\alpha}R_{ij}^{\beta}R_{ij}^{\gamma}}{R_{ij}^3}S_{ij}\rho_j^{\alpha(3)}\right]^2 - \frac{3}{5}\sum_{\alpha=1}^{3}\left[\sum_{j\neq i}\frac{R_{ij}^{\alpha}}{R_{ij}}S_{ij}\rho_j^{\alpha(3)}\right]^2
\end{aligned}
\tag{2.18}
$$

Here $\rho_j^{\alpha(c)}(c = 0, 1, 2, 3)$ are the atomic electron densities at distance R_{ij} of site j from site i (α=x,y,z). R_{ij}^{α} is the α component of the distance vector between j and i. S_{ij} is the screening function. Finally the average weighting factor $t^k(k = 1, 2, 3)$ dependent on the element is given by

$$
t_i^{(k)} = \frac{1}{{\rho_i}^0}\sum_{j\neq i} t_{0,j}^{(k)}\rho_j^{\alpha(0)}S_{ij} \tag{2.19}
$$

Here $t_{0,j}^{(k)}$ is an element-dependent parameter. The atomic electron densities are computed as

$$
\rho_i^{\alpha(k)}(R_{ij}) = \rho_{i0}\exp\left[-\beta_i^{(k)}(\frac{R_{ij}}{R_i^0} - 1)\right] \tag{2.20}
$$

where R_i^0 is the nearest-neighbor distance in the single-element reference structure and $\beta_i^{(k)}$ are the element dependent parameters, ρ_{i0} is an element-dependent electron density with a relation to the composition-dependent electron density given as:

$$\rho_i^0 = \rho_{i0} Z_{i0} G(\Gamma_i^{\text{ref}}) \tag{2.21}$$

where

$$\Gamma_i^{\text{ref}} = \frac{1}{Z_{i0}^2} \sum_{k=1}^{3} t_i^{(k)} S_i^{(k)} \tag{2.22}$$

In the above equations, Z_{i0} is the first nearest-neighbor coordination of the reference system given by Eq. (2.21). The shape factor depending on the reference structure for atom i is given as $S_i^{(k)}$.

The pair potential consisting of a screening effect is given by:

$$\phi_{ij}(R_{ij}) = \bar{\phi_{ij}}(R_{ij}) S_{ij} \tag{2.23}$$

$$\bar{\phi_{ij}}(R_{ij}) = \frac{1}{Z_{ij0}} [2E_i^u(R_{ij} - F_i(\rho_i(R_{ij})) - F_j(\rho_j(R_{ij}))] \tag{2.24}$$

$$E_i^u(R_{ij}) = -E_{ij}^0(1 + a_{ij}^*(R_{ij}))e^{-a_{ij}^*(R_{ij})} \tag{2.25}$$

$$a_{ij}^* = \alpha_{ij}\left(\frac{R_{ij}}{R_{ij}^0} - 1\right) \tag{2.26}$$

Here E_{ij}, α_{ij} and R_{ij}^0 depend on the element i and j, and Z_{ij} depends upon the structure of the reference system. In Eq. (2.24), $\rho_j(R_{ij})$ is the background electron density of the j atom for the reference structure with interatomic distance R_{ij}.

The screening function depends on the cutoff radius R_c designed in such a way that $S_{ij} = 1$ if atoms i and j are un-screened and within the limit of a cutoff radius, and $S_{ij} = 0$ if they are outside this cutoff range. For partial screening, its value varies between 0 and 1. The total screening function involves the product of a cutoff function and three-body terms involving all other atoms in the system, and is given as:

$$S_{ij} = \bar{S_{ij}} f_c\left(\frac{R_c - R_{ij}}{\Delta R}\right) \tag{2.27}$$

$$\bar{S_{ij}} = \prod_{k \neq i,j} S_{ijk} \tag{2.28}$$

$$S_{ijk} = f_c\left(\frac{C_{ijk} - C_{min,ijk}}{C_{max,ijk} - C_{min,ijk}}\right) \tag{2.29}$$

$$C_{ijk} = 1 + 2\frac{R_{ij}^2 R_{ik}^2 + R_{ij}^2 R_{jk}^2 - R_{ij}^4}{R_{ij}^4 - (R_{ik}^2 - R_{jk}^2)^2} \tag{2.30}$$

$$f_c(x) = \begin{cases} 1 & \text{for } x \geq 1 \quad (2.31) \\ \left[1-(1-x)^4\right]^2 & \text{for } 0 < x < 1 \quad (2.32) \\ 0 & x \leq 0 \quad (2.33) \end{cases}$$

C_{min} and C_{max} can be defined separately for each ijk triplet, based on element type. ΔR controls the distance over which radial cutoff is smoothed from 1 to 0 near $R = R_c$.

2.2.1 Atomistix Toolkit (ATK) forcefield

The MEAM parameters were directly taken from the study published by Jelinek et al [44]. For the calculations of elastic properties, the MEAM potential was applied by using the Atomistix toolkit (ATK) forcefield [45, 46]. Fe-Al compounds were optimized by using the quasi-Newton optimizer "Limited-memory Broyden-Fletcher-Goldfarb-Shanno (LBFGS)" [47]. The atoms were relaxed until the maximum forces and stresses were less than 0.001 eV/atom and 0.01 GPa, respectively.

Chapter 3

Theoretical Background

> "I... a universe of atoms, an atom in the universe."
>
> Richard Feynman (1918-1988)

The main focus of this work is to predict the mechanical strength of bulk and interface structures by virtual tensile and shear strength testing. The atomic structures studied in this work are based on the activities in the physical metallurgical group within the Department of Materials Science and Engineering at NTNU in Trondheim, responsible for joining aluminum and steel, and of the Department of Physics at, NTNU in Trondheim, which provided transmission electron microscopy (TEM) images. The TEM analysis showed three distinct IMC phases, i.e. α-AlFeSi, Fe_4Al_{13} and Fe_2Al_5 [48].

The distinct IMC phases reported are shown in Fig. 3.1, and their specific order and related interfaces are the basis for the computational studies. Furthermore, an additional interface between Al and Fe_4Al_{13} has also been studied. This interface has been reported in an other experimental work [49].

The essential challenge of working with this system is to develop low-misfit interface structures. Due to the large unit cell size of these IMCs, it is very challenging to build low-strain interface structures containing a low number of atoms. The theory behind developing such complex low-strain structures is discussed in the next section. The next key challenge faced in this thesis is the optimization of the interface structures. A brief introduction about the optimization methods used is also given, and the methodology for calculating virtual tensile and shear strengths

from the optimized structures is discussed in the latter part of this chapter.

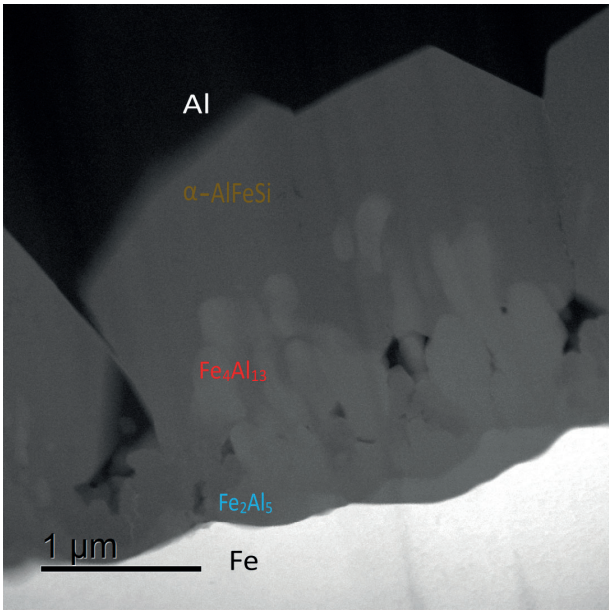

Figure 3.1: HAADF-STEM image of a cold metal transfer (CMT) welded sample showing the arrangements of distinct intermetallic layers. Image credit to Tina Bergh from the Department of Physics and the TEM Gemini Center at NTNU in Trondheim.

3.1 Introduction to atomic interface builder

3.1.1 Face-to-face matching model

All interface models have been developed by a face-to-face matching technique, which develops periodic structures by matching the planes of two phases. This method creates periodic interfaces by slightly straining both crystals. The development of the interface structures using the face-to-face matching technique consist of the following procedures:

- First the equivalent crystallographic directions of Crystal 1 and Crystal 2 are determined, which are governed by the minimization of the interface energy.
- An interface represents a set of possible periodic interfaces between crystals, called Crystal 1 and Crystal 2 (Fig. 3.2). The possible interface planes in Crystal 1 are defined by all pair of lattice vectors, $\mathbf{u}_1$ and $\mathbf{v}_1$ in Crystal 1. Similarly, $\mathbf{u}_2$ and $\mathbf{v}_2$ define all possible interface planes of Crystal 2. To get

a periodic interface, the length of vector directions of Crystal 1 ($\mathbf{u}_1$ and $\mathbf{v}_1$) should be equal to the length of vector directions of Crystal 2 ($\mathbf{u}_2$ and $\mathbf{v}_2$).

- Face-to-face matching constructs 3D interface models, which identifies an additional set of possible directions, $\mathbf{w}_1$ and $\mathbf{w}_2$ to Crystal 1 and Crystal 2 respectively.

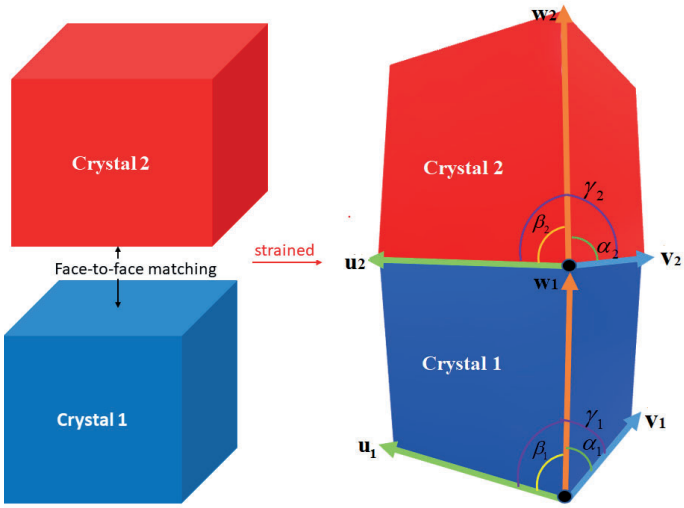

Figure 3.2: The schematic illustration of matching model, where two crystals are strained to match face-to-face to form a coherent/semi-coherent interface structure.

Angles of the Crystal 1 and Crystal 2 should also be matched/strained to form a coherent/semi-coherent interface. This identifies the additional set of conditions:

$$\begin{aligned} \angle\alpha_1 &= \angle\alpha_2 \\ \angle\beta_1 &= \angle\beta_2 \\ \angle\gamma_1 &= \angle\gamma_2 \end{aligned} \tag{3.1}$$

where $\angle\,\alpha_n = \angle(\mathbf{v}_n, \mathbf{w}_n)$, $\angle\,\beta_n = \angle(\mathbf{u}_n, \mathbf{w}_n)$ and $\angle\,\gamma_n = \angle(\mathbf{u}_n, \mathbf{v}_n)$ $(n = 1, 2)$ are defined in Fig. 3.2. Fig 3.2 shows an example of a strained interface model.

- Generally it is difficult to find an OR, which exactly follows the above criteria. So in order to match both crystals to form an interface model, crystals are strained to match at the interface. The resulting interface models depend on the condition of how much strain was introduced to develop a particular

interface model. The lattice strain introduced to match the interface structure is calculated according to the following relations:

$$\epsilon_u = \frac{||\mathbf{u}_2| - |\mathbf{u}_1||}{|\mathbf{u}_1|} \tag{3.2}$$

$$\epsilon_v = \frac{||\mathbf{v}_2| - |\mathbf{v}_1||}{|\mathbf{v}_1|} \tag{3.3}$$

where ϵ_u and ϵ_v is the strain introduced along the **u** and **v** directions, respectively.

- In order to reduce the number of atoms, a vacuum layer is added along the normal direction. The vacuum layer should be >10 Å thick to remove any interaction between two artificial interfaces. This condition removes the need for the consideration of angles α_n and β_n, since the structures are not periodic along the normal direction. Hence the relevant angle for building a low lattice misfit interface is γ_n. Due to the large unit cell size of the considered Fe-Al IMCs, we have developed all interface structures with a vacuum layer of >10 Å.

- The next step of building low-energy interface structures is determining of close-packed or nearly close-packed matching directions of Crystal 1 and Crystal 2 using the atom positions and lattice parameters by calculating the atomic linear density.

3.1.2 Selection of interface structures

After obtaining a possible ORs between bulk phases and developing an interface structure, there is still a further need for refinement of the interface structure before the calculation of mechanical properties. The additional degrees of freedom that need to be optimized can be defined as follows [50]:

- Lateral translation of the subcells along the interface plane (2 degrees of freedom).

- The cutting plane of each two subcells (2 degrees of freedom) and additional spacing perpendicular to the interface, which needs to be added or removed (2 degrees of freedom).

- Atoms at the interface could be removed, added or moved to form a new structure at the interface (many degrees of freedom).

Table 3.1: The calculated lattice parameters from the present calculation compared with references and measured values. H_f is the formation enthalpy and V_0 is the equilibrium volume per atom in Å^3 [51].

Phase	Space group	Species	a_0(Å)	b_0(Å)	c_0(Å)	V_0 (Å^3)	H$_f$(eV/atom)
FeAl	Pm3m	This work	2.953	-	-	12.87	-1.48
		EAM/MEAM	2.893 [53]	-	-	12.88 [44]	-1.42 [57]
		DFT [52]	2.851 [52]	-	-	12.07 [55]	-0.390 [52]
		Exp.	2.909 [54]	-	-	12.23 [56]	-0.423 [58], -0.28 [59]
Fe$_3$Al	Fm3m	This work	5.769			12.00	-0.53
		EAM/MEAM	5.764 [53]			12.01 [44]	-0.279 [53]
		DFT	5.586 [52]			12.01 [55]	-0.217 [52]
		Exp.	5.789 [60], 5.792 [54]			12.07 [56]	-0.202 [61], -0.321 [58]
FeAl$_3$	C2/m	This work	16.680	7.860	12.220	15.73	-0.532
		EAM/MEAM	15.069 [53]	7.864	12.083	15.03 [44]	-0.059 [53]
		DFT	15.352 [52]	8.010	12.398	13.91 [44]	-3.923 [52] -4.562 [62]
		Exp.	15.49 [54]	8.08	12.48	-	n.a
FeAl$_2$	P1	This work	4.054	6.687	8.802	15.77	-0.093
		EAM/MEAM	4.6212 [53]	6.372	8.629	14.71 [44]	-0.160 [53], -0.076 [44]
		DFT	4.793 [52]	6.351	8.658	12.78 [44]	-0.286 [52]
		Exp.	4.787 [54]	4.787	6.461	-	n.a
Fe$_2$Al$_5$	Cmcm	This work	7.462	6.717	4.464	15.96	-1.0303
		EAM	7.622 [53]	6.323	4.178		-0.146 [53]
		DFT	7.466 [52]	6.181	4.808		-8.385 [52] -7.352 [62]
		Exp.	7.675 [54]	6.403	4.203		n.a

Due to the large structures and computational cost associated with it, optimizing these degrees of freedom is a great challenge. For this reason, we used the MEAM potentials to find a good initial guess of interface structures for the DFT optimization and calculations. To assess the whether MEAM potential is suitable for Fe-Al compounds, we also performed MEAM calculations of the structural and mechanical properties of Fe-Al compounds and compared with other theoretical [52, 53, 57] and experimental studies [58, 59, 61] (Paper II). According to our calculations, the MEAM potential showed good agreement with other studies for Fe-Al compounds, but we were unable to find satisfactory results for the α-AlFeSi phase. Hence, this potential was only applicable to the Fe-Al compounds interface structures. Table 3.1 shows the comparisons of calculations of Fe-Al compounds structural properties with other theoretical and experimental studies. Interface optimization with the MEAM potential was performed by using Atomistix toolKit-Forcefield [45] implemented by Quantumwise [46].

3.2 Application of the face-to-face matching technique for Fe-Al compounds interfaces

Using the face-to-face matching technique as described earlier, we estimated and developed atomic interface structures between the following interfaces, (i) Al // Fe$_4$Al$_{13}$, (ii) Al // α-AlFeSi,(iii) θ-Fe$_4$Al$_{13}$ // η-Fe$_2$Al$_5$, (iv) η-Fe$_2$Al$_5$ // Fe and α-AlFeSi // θ-Fe$_4$Al$_{13}$. Based on the face-to-face matching technique different ORs

Table 3.2: The final ORs used in this work between interface structures, m_1, m_2 and m_3 are the components of a linear combination of lattice vectors of crystal 1, similarly n_1, n_2 and n_3 are defined for crystal 2.

Interface	**d**	m_1	m_2	m_3	length (Å)	angle	n_1	n_2	n_3	length(Å)	angle	strain (%)
Fe_4Al_{13} // Fe_2Al_5	**u**	0	0	1	12.42		0	0	-3	12.29		1.12
	v	0	-2	0	16.05	90.0°	2	-1	0	16.14	90.0°	0.56
	w	1	0	0	-		-1	-2	0	-		-
Al // Fe_4Al_{13}	**u**	2	0	0	8.08	90.0°	0	1	0	8.08	90.0°	0.00
	v	0	4	1	16.66	90.0°	1	0	1	16.67	90.0°	0.10
	w	0	-1	4	-		1	0	-1	-		-
Al // α-AlFeSi	**u**	3	1	0	12.80	90.0°	1	0	0	12.69	90.0°	0.89
	v	1	-3	0	12.80	90.0°	0	0	1	12.69	90.0°	0.89
	w	0	0	-3	-		0	1	0	-		-
Fe_2Al_5 // Fe	**u**	0	0	-1	4.10	90.0°	1	0	1	4.06	90.0°	0.89
	v	1	0	0	7.40	90.0°	1.5	1.5	-1.5	7.46	90.0°	0.79
	w	0	-2	0	12.88	90.0°	-2	4	2	-	90.0°	-
Fe_4Al_{13} // Fe_2Al_5	**u**	0	0	1	12.42		0	0	-3	12.29		1.12
	v	0	-2	0	16.05	90.0°	2	-1	0	16.14	90.0°	0.56
	w	1	0	0	-		-1	-2	0	-		-
α-AlFeSi // Fe_4Al_{13}	**u**	1	2	1	17.43		1	1	0	17.76		1.90
	v	-1	-1	0	17.47	121.5°	0	-1	1	17.76	121.5°	1.65
	w	1	-1	1	-		1	-1	-1	-		-

were determined between the different Fe-Al compounds, and only those ORs which provided low lattice misfit were taken into consideration. Table 3.2 lists the final ORs between interface structures used in this work.

Al // Fe_4Al_{13} interface

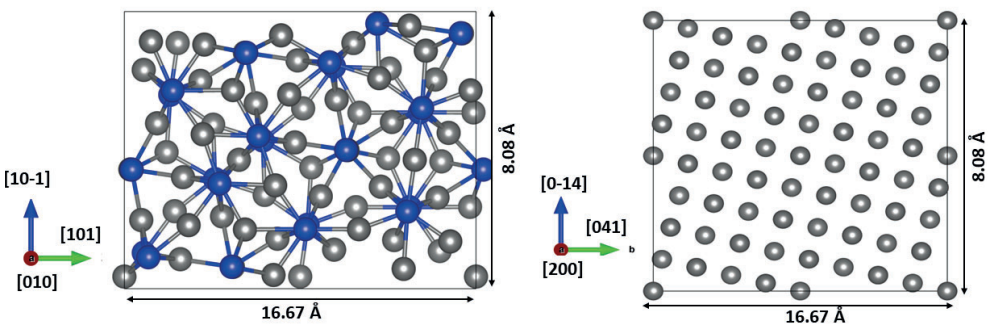

Figure 3.3: Equivalent directions and lengths for Fe_4Al_{13} and Al phases. Al atoms are shown in grey and Fe atoms in blue.

According to the face-to-face matching technique, the OR between two bulk phases A and B depends on the lattice constant ratios, because it directly influences the interatomic and interplanar spacing of the phases. Since Al is a FCC crystal and Fe_4Al_{13} is a monoclinic crystal, the OR between monoclinic-FCC depends on the

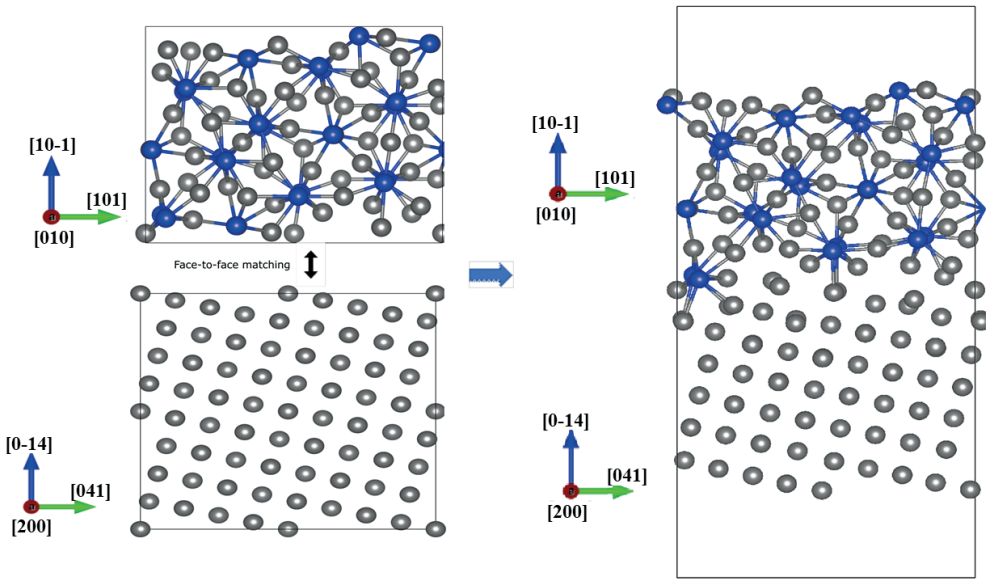

Figure 3.4: Face-to-face matching of bulk Fe_4Al_{13} and Al along [010]//[200] to form an interface structure.

ratios a_M/a_F, b_M/a_M and c_M/a_M. Here a_M, b_M and c_M represent the lattice constants of the monoclinic system and a_F of the FCC system.

The lattice constant used for Al is 4.04 Å and for Fe_4Al_{13}, we used $a = 15.49$ Å, $b = 8.08$ Å, and $c = 12.48$ Å. The atom positions for Fe_4Al_{13} were taken from Liu et al. [49]. Based on the face-to-face matching technique, the nearly closed-packed planes for Al and Fe_4Al_{13} were identified as $\{014\}$ and $\{101\}$, respectively. These planes consist of [200] and [041] directions for Al and [010] and $[10\bar{1}]$ for Fe_4Al_{13}, which are nearly closed-packed directions. Then, after picking out the nearly close-packed plane, the next step is to match both phases. In order to match the interface structure, Fe_4Al_{13} is cut in such a way that both phases are parallel to each other and ready to meet face-to-face as shown in Fig. 3.4 and 3.5. Fig 3.3 shows the equivalent directions of Al and Fe_4Al_{13}.

Fig 3.4 and 3.5 show the strained atom layers of Al and Fe_4Al_{13} which were matched to form an interface. After successfully predicting the OR and matching both structures by introducing strain, the strained structures were stacked together as shown in Fig. 3.4 and 3.5. As shown in Fig 3.5, Al and Fe_4Al_{13} atoms are arranged at the interface along the [101] // [041] direction. Moreover, the lattice mismatch along that direction is 0.10. Similarly, the best match was found along $[010]_{Fe_4Al_{13}}$ // $[200]_{Al}$ with lattice strain of 0.0 %. Finally, atoms aligned in a

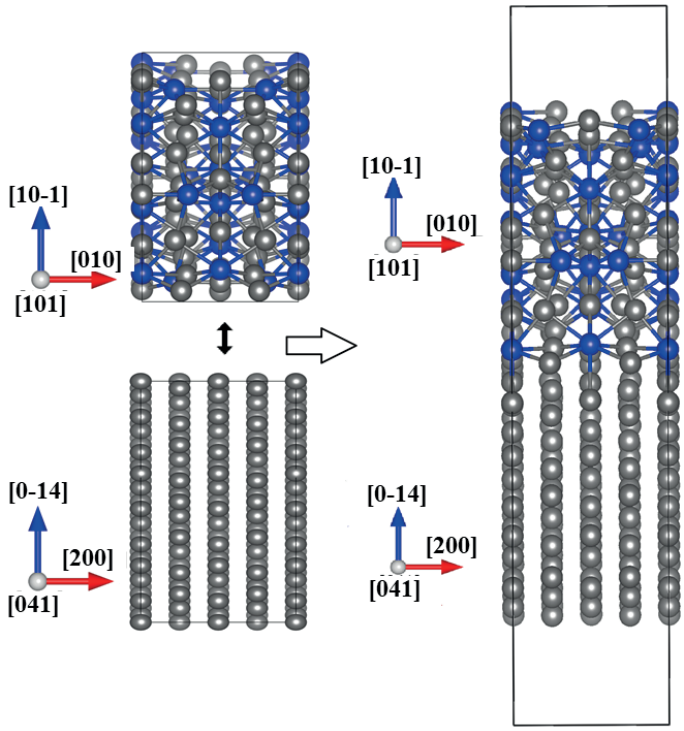

Figure 3.5: Face-to-face matching bulk Fe_4Al_{13} and Al along [101]//[041] to form an interface structure.

straight line along this direction are displayed in Fig. 3.5. Hence, the final OR between Al//Fe_4Al_{13} is given as;

$(10\bar{1})_{Fe_4Al_{13}} \parallel (0\bar{1}4)_{Al}$
$[010]_{Fe_4Al_{13}} \parallel [200]_{Al}$
$[101]_{Fe_4Al_{13}} \parallel [041]_{Al}$

Al // α-AlFeSi interface

As mentioned earlier, to predict the OR, the atom positions, lattice parameters and crystal structure of both phases are required. The atomic positions have been defined according to a study published by Cooper [63]. The α-AlFeSi has a cubic symmetry with a space group of $Im\bar{3}$ and lattice constant $a = 12.69$ Å. The unit cell of α-AlFeSi contains 138 atoms, i.e. 100 Al, 24 Fe atoms and 14 Si atoms [49]. Al is also a FCC crystal with a lattice constant of $a = 4.04$ Å, so the OR between

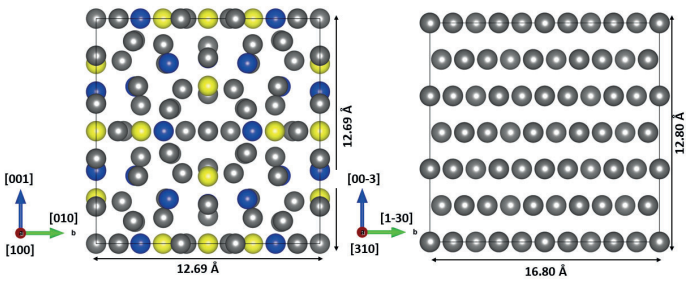

Figure 3.6: Equivalent directions and lengths of α-AlFeSi and Al. Al atoms are identified in grey, Fe as blue and Si as yellow.

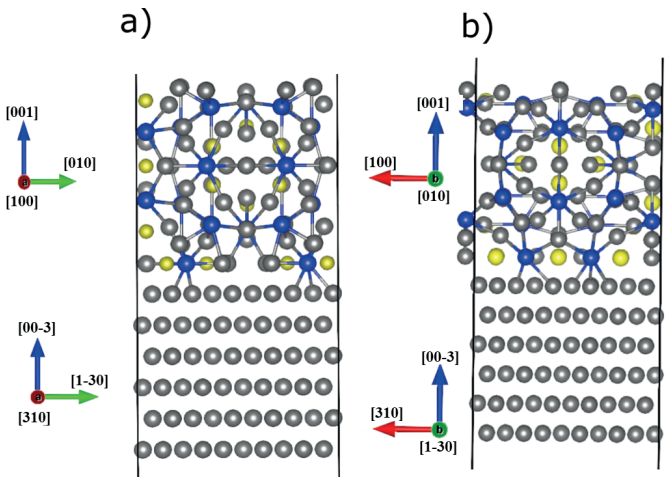

Figure 3.7: Face-to-face matched interface structure between Al and α-AlFeSi. Close-packed atom rows of Al and α-AlFeSi are matched along (a) [100]//[310] and (b) [010]//[1$\bar{3}$0].

α-AlFeSi and Al depends on the ratio a_{Al}/a_{α}. The best match for the close-packed or nearly close-packed directions for Al is identified to be <310>$_{Al}$ and <130>$_{Al}$ for the $(003)_{Al}$ plane. For α-AlFeSi, close-packed or nearly close-packed directions are <100>$_{\alpha}$ and <001>$_{\alpha}$ for the $(010)_{\alpha}$ plane. Atomic configurations for α-AlFeSi and Al along these directions are quite similar. Along these directions, Al and α-AlFeSi atoms are arranged in parallel rows. According to the face-to-face matching criteria, both phases are strained according to Eq. (3.1) and (3.2) to match at the interface. A lattice strain of 0.89 % was introduced along $[100]_{\alpha}$ // $[310]_{Al}$ and $[001]_{\alpha}$ // $[1\text{-}30]_{Al}$, respectively . Therefore this provides good matching directions for the Al //α-AlFeSi interface. Fig. 3.6 shows the matched planes for Al and α-AlFeSi. Moreover, all angles between two bulk phaes α-AlFeSi and

Al are equal along these directions. The atoms were stacked together along the (00-3)$_{Al}$ and (001)$_{\alpha}$ plane.

According to the matching criteria, matched Al and α-AlFeSi atom rows were stacked face-to-face such that atom rows of Al are parallel to atom rows of α-AlFeSi, as shown in Fig. 3.7. The final OR between Al and α-AlFeSi is given as;

$(010)_{\alpha\text{-AlFeSi}} \,||\, (00\bar{3})_{\text{Al}}$
$[100]_{\alpha\text{-AlFeSi}} \,||\, [310]_{\text{Al}}$
$[001]_{\alpha\text{-AlFeSi}} \,||\, [1\bar{3}0]_{\text{Al}}$

Fe_4Al_{13} // Fe_2Al_5 interface

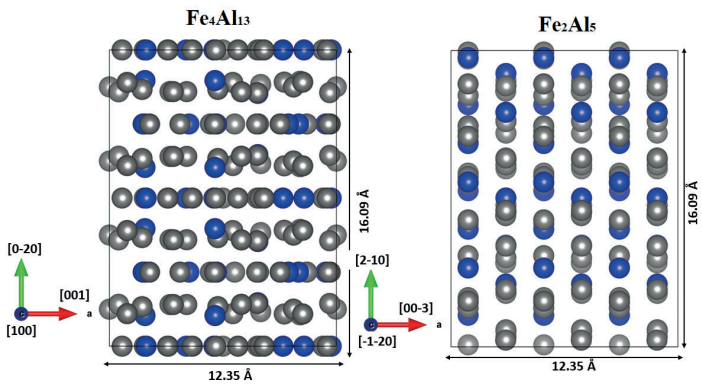

Figure 3.8: Equivalent lengths and ORs between Fe_2Al_5 and Fe_4Al_{13}.

The interface structure between Fe_2Al_5 and Fe_4Al_{13} is complex due to large unit cells. Fe_2Al_5 has an orthorhombic symmetry with lattice constants of $a = 7.657$ Å, $b = 6.409$ Å and $c = 4.227$ Å. The atomic positions and lattice constants for Fe_2Al_5 were taken from the directory of the Springer library [64]. Due to non-stoichiometry in the composition of Fe_2Al_5, Al atoms have a site occupancy of 1/6, which indicates that Al atoms can be occupied at different sites in the orthorhombic structure of Fe_2Al_5. To find the stable position of Al atoms, we performed DFT calculations with different positions of Al atoms in the structure. The structure with the lowest ground-state energy was further used for interface building. This approach possesses the advantage of being able not only to find the stable configuration of the orthorhombic Fe_2Al_5 crystal structure but also reducing the number of atoms in a unit cell, which facilitated an OR with a minimum number of atoms and a simpler interface structure. We will be using the DFT-relaxed bulk crystal struc-

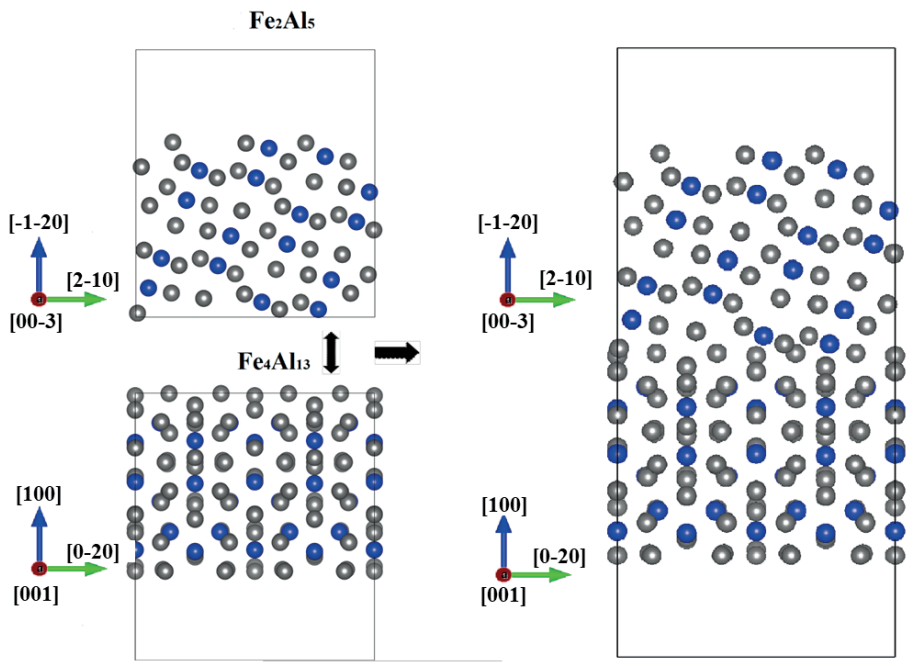

Figure 3.9: Fe_2Al_5 and Fe_4Al_{13} are strained such that both phases are parallel to each other and ready to meet face-to-face.

ture to build an interface structure. The lattice constants used after optimization of Fe_2Al_5 are given as $a = 7.397$ Å, $b = 6.442$ Å and $c = 4.095$ Å.

Based on the atom positions for Fe_2Al_5 and Fe_4Al_{13} crystal structures, the close-packed or nearly close-packed directions identified for the $(1\bar{2}0)$ plane of Fe_2Al_5 are <003> and <210>, and those for the (100) plane for Fe_4Al_{13} are <001> and <020>. So the matching plane $(1\bar{2}0)_{Fe_2Al_5}$ // $(100)_{Fe_4Al_{13}}$ is related to matching directions $[00\bar{3}]_{Fe_2Al_5}$ // $[001]_{Fe_4Al_{13}}$ and $[2\bar{1}0]_{Fe_2Al_5}$ // $[0\bar{2}0]_{Fe_4Al_{13}}$. The next step is to match the both phases so that both phases become parallel to each other. As shown in Fig. 3.8, the Fe_4Al_{13} and Fe_2Al_5 structures were cut along the defined ORs so that lenghts and angles of both phases match with each other, and ready to meet face-to-face to form an interface (Fig. 3.9). Due to the addition of a vacuum layer along the normal direction, unit cells are not periodic along the $[100]//[\bar{1}\bar{2}0]$ direction, which is why the only relevant angle is γ between $[001]//[00\bar{3}]$ and $[0\bar{2}0]//[2\bar{1}0]$ directions. A lattice strain of 1.12 % and -0.554 % was introduced along $[001]//[00\bar{3}]$ and $[100]//[1\bar{2}0]$ directions, respectively, to match both phases at the interface. The final structures are stacked together face-to-face as displayed in Fig. 3.9. As can also be seen in Fig. 3.10, atom rows of Fe_2Al_5 match with

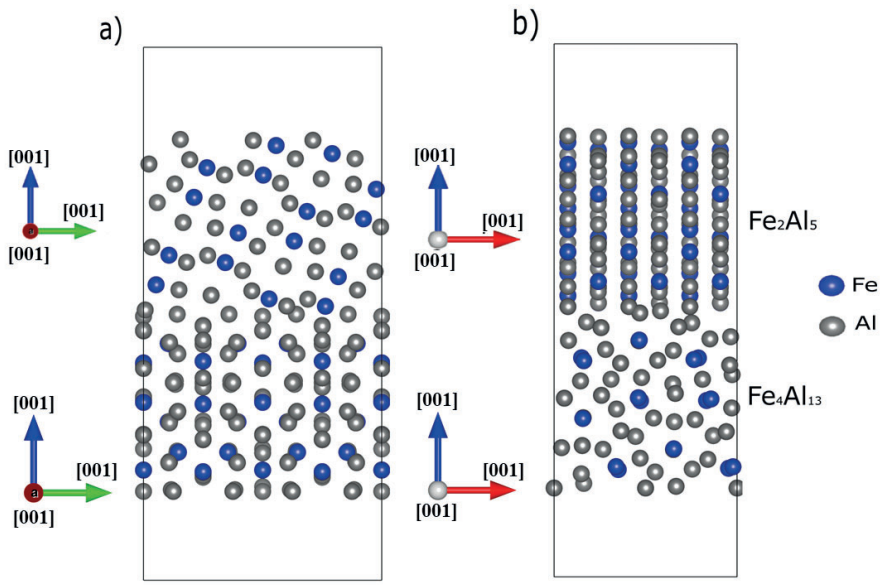

Figure 3.10: Face-to-face matched interface structure between Fe_2Al_5 and Fe_4Al_{13}.

atom rows of Fe_4Al_{13} at the interface. The final OR between Al and α-AlFeSi is given as;

$[00\bar{3}]_{Fe_2Al_5} \parallel [001]_{Fe_4Al_{13}}$
$[2\bar{1}0]_{Fe_2Al_5} \parallel [0\bar{2}0]_{Fe_4Al_{13}}$
$(\bar{1}\bar{2}0)_{Fe_2Al_5} \parallel (100)_{Fe_4Al_{13}}$

Fe_2Al_5 // Fe interface

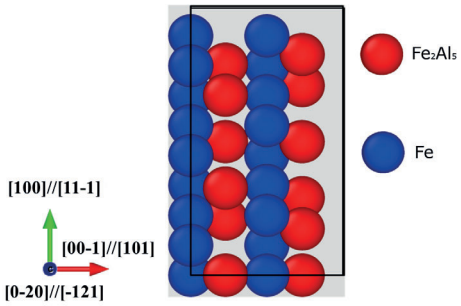

Figure 3.11: Superimposed structures of Fe and Fe_2Al_5.

Fe and Fe_2Al_5 has BCC and orthorhombic symmetries with lattice parameters

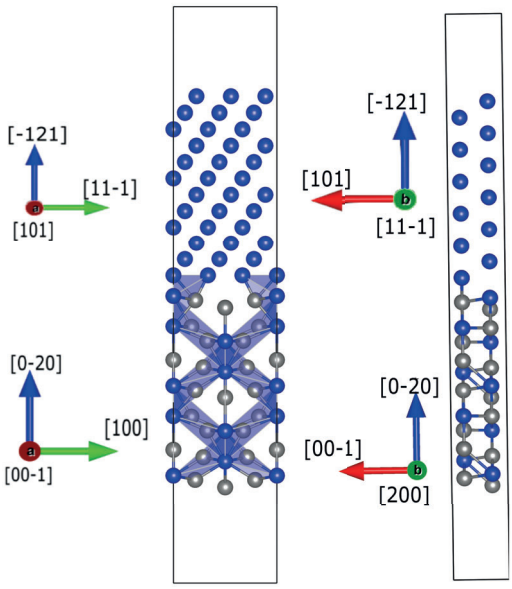

Figure 3.12: Matched interface structure between Fe_2Al_5 and Fe.

of a_{Fe} = 2.87 Å and a = 7.397 Å, b = 6.442 Å, c = 4.095 Å, respectively. For building the Fe_2Al_5 interface structure, the DFT-relaxed bulk Fe_2Al_5 structure was used. Based on the lattice parameters, closed-packed/nearly close-packed directions found for Fe_2Al_5 $(0\bar{2}0)$ are $[00\bar{1}]$ and [100], and for the Fe lattice a close-packed plane was identified to be $(\bar{1}21)$ along [101] and $[11\bar{1}]$ directions. Fig. 3.11 shows the superimposed $(0\bar{2}0)_{Fe_2Al_5}$ // $(121)_{Fe}$ plane. Both phases nicely match along these directions.

In order to match both phases along $[00\bar{1}]$//[101] and [100]//$[11\bar{1}]$ lattice strains of 0.89% and 0.79% were introduced, respectively. The final matched structure is shown in Fig. 3.12.

α-AlFeSi // Fe_4Al_{13}

The interface between α-AlFeSi // Fe_4Al_{13} is developed by using the same procedure as described above. The lattice constants and atomic positions used for developing this interface structures have already been described in previous subsections. The final OR used for this interface structure is given in Table 3.2. Fig. 3.13 shows the interface between α-AlFeSi and Fe_4Al_{13}. Lattice strains of 1.90% and 1.65 % were introduced between [121] // [110] and $[\bar{1}\bar{1}0]$ // $[0\bar{1}1]$, respectively.

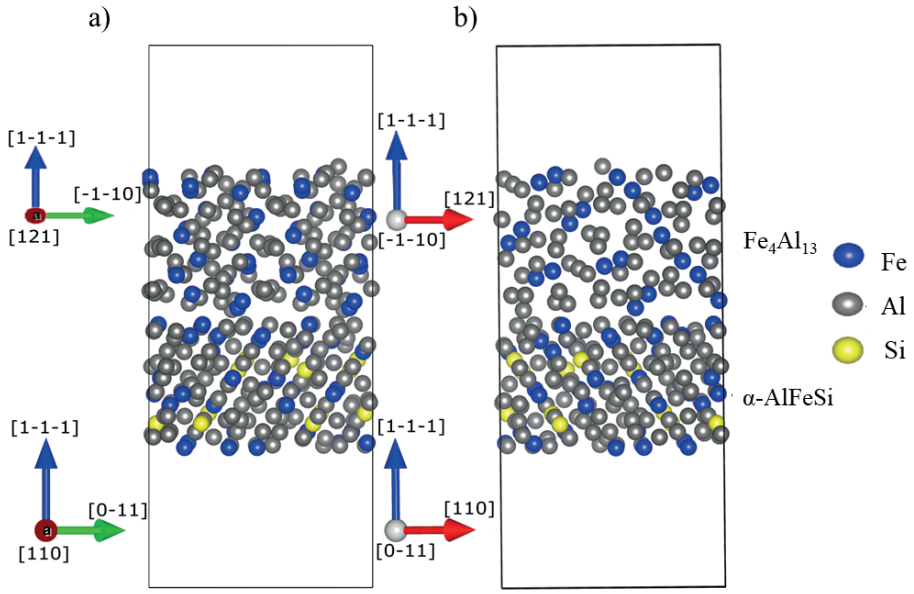

Figure 3.13: Face-to-face matched interface structure between α-AlFeSi and Fe_4Al_{13}.

3.3 Structural relaxation

After establishing successful and refined interface structures, the next crucial step is to optimize these structures using DFT before proceeding to mechanical calculations. The main challenge in optimizing these structures is their large cell size and number of atoms, which makes it extremely challenging to converge the structures and bring down forces in the range of 0.01 eV/Å. To find the structures with minimum potential energy, many well-established optimization methods have been applied such as conjugate gradient (CG), steepest descent, Newton-Raphson, quasi-Newton or truncated Newton methods [29, 30, 65, 66]. These optimization methods use the force projection to direct the optimizer towards the minimum energy paths and saddle points [67]. Owing to the large cell size of these interface structures, however, finding the minimum energy path requires huge computational resources and time. To address this problem, a new optimization method, the so-called Fast Inertial Relaxation Engine (FIRE) introduced by Bitzek et al. [2] was adopted.

3.3.1 Fast inertial relaxation engine

This method specifically directs the velocity towards an external force direction and resets the velocity when force and velocity are in opposite directions. To understand the mechanism of this method, consider a blind skier on an unknown

hilly mountain range described by the potential energy landscape of $E(\mathbf{x})$ with $\mathbf{x}$=(x_1, x_2). By assuming that the skier could choose the direction and stop if needed, the skier obeys the following equation of motion (Fig. 3.14) [2]:

$$\dot{\mathbf{v}}(t) = \mathbf{F}(t)/m - \gamma(t)|\mathbf{v}(t)|[\hat{\mathbf{v}}(t) - \hat{\mathbf{F}}(t)] \tag{3.4}$$

where m is the mass, the velocity $\mathbf{v}$= $\dot{\mathbf{x}}$, the force $\mathbf{F}$=$-\nabla E(\mathbf{x})$, $\hat{\mathbf{v}}(t)$ and $\hat{\mathbf{F}}(t)$ are the normalized velocity and force components. The skier accelerates in the direction which is steeper than the current direction via the function $\gamma(t)$, if the power $P(t) = \mathbf{F}(t) \cdot \mathbf{v}(t)$ is positive. When the power function becomes negative, the skier stops to avoid uphill motion. Since the current velocities carry the information about the average descent direction and energy scale, the function $\gamma(t)$ should not be too large. Fig. 3.15 shows a comparison of the FIRE algorithm with other powerful schemes CG and L-BFGS. FIRE keeps intact and surprisingly fast as compared to CG and LBFGS for the optimization of the spiral-shaped potential energy function. Therefore, this algorithm can be used on larger systems having millions of degree of freedom.

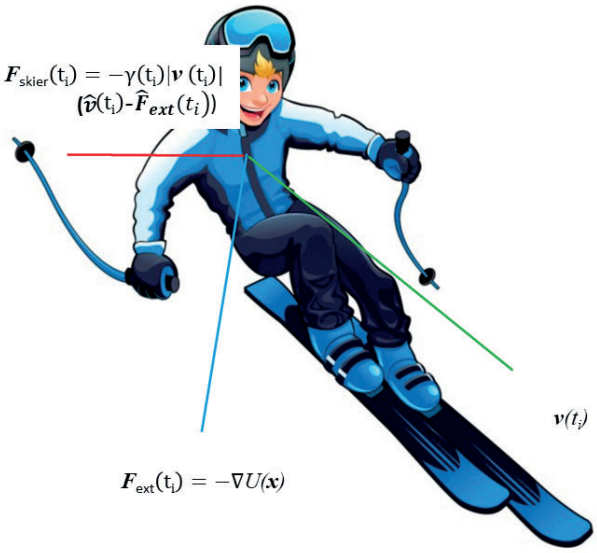

Figure 3.14: Mechanism of the FIRE optimization algorithm analogous to a blind skier searching for the bottom of the valley in an unknown mountain area [2].

While relaxing the system, this algorithm considers the following velocity modifications, (1) stopping to avoid uphill motion, (2) discrete use of an MD time step Δt, and (3) steer in the start then let the inertia decide the direction. Given the initial values of Δt, α=α_{start} and $\mathbf{v}$=0, the FIRE algorithm uses the following

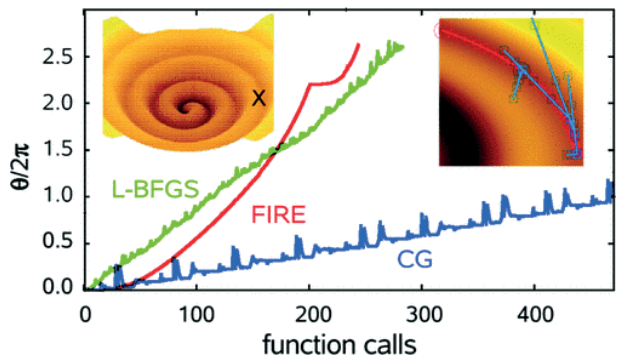

Figure 3.15: Comparison of the FIRE optimization method with CG and the limited memory Broyden-Fletcher-Goldfarb-Shanno (L-BFGS) scheme for a spherical-shaped potential energy function [2].

propagation rules [2]:

1. Calculate x, **F**=-$\nabla E(\mathbf{x})$ and velocity **v**.
2. Calculate P = **F** · **v**.
3. Set **v** $\rightarrow$ $(1-\alpha)$**v**+α $\hat{\mathbf{F}}|v|$
4. For $P > 0$, increase the time step $\Delta t \rightarrow min(\Delta t \cdot f_{min}, \Delta t_{max})$ and decrease $\alpha \rightarrow \alpha \cdot f_{\alpha}$.
5. If $P \leq 0$, decrease the time step $\Delta t \rightarrow min(\Delta t, f_{dec})$, and freeze the system **v** $\rightarrow$ 0 and set α to α_{start}.
6. Return to Molecular Dynamics.

3.3.2 Conjugate gradient

This method follows the conjugate search direction instead of just following the force. This algorithm applies the Polak-Ribère formula [67, 68]:

1. Search direction is being initialized along the force,
   $d_0 = F_0$
2. Using a line search, calculate the step size λ,
   $R_{j+1} = R_j + \lambda\, d_j$

3. Evaluate the conjugate search direction,
   $d_{j+1} = F_{j+1} + \gamma\, d_j$

where $\gamma = F_{j+1} \cdot (F_{j+1}\text{-}F_j)/|F_j|^2$. In order to minimize the force along the search direction d_i, a single Newton's method was adopted at each iteration. The finite difference step was used to evaluate the derivative of the force along the search direction, so that each CG iteration needs two force evaluations.

3.3.3 Implementation of optimization methods

These optimization methods have been incorporated in VASP for DFT calculations [69]. To use these force-based optimizers, a damped molecular dynamics is used for the update of ionic degrees of freedom with a step size of 0 for a scaling constant. This procedure disables the built-in optimizers. These force-based optimizers are selected by specifying the particular IOPT value for the optimizers in the VASP input INCAR file.

3.4 Mechanical properties

3.4.1 Bulk strength

The bulk material properties of Fe-Al compounds were determined by the calculations of single-crystal elastic constants. The Fe-Al compounds studied in this work are anisotropic, which means that their mechanical properties are dependent on the direction of the principal axis frame. In calculations of elastic constants, the crystal is subject to the applied force (stress tensor), which results in the deformation described by the strain tensor. The elastic deformation can be described by the generalized Hooke's law,

$$\sigma_{ij} = \sum_k \sum_l C_{ijkl}\epsilon_{kl} \tag{3.5}$$

where σ_{ij} and ϵ_{kl} are the stress and strain tensor, respectively, and C_{ijkl} is the stiffness tensor. The strain is expressed by inverting Eq. (3.5)

$$\epsilon_{ij} = \sum_k \sum_l S_{ijkl}\sigma_{kl} \tag{3.6}$$

Here S_{ijkl} is the compliance tensor. The elastic constant in Eq. (3.5) C_{ijkl} contains 81 elastic coefficients. At most, 21 of these 81 elastic components are independent. The number of elastic components can be further reduced, depending on the symmetry of the crystal [70].

3.4.2 Bulk mechanical properties

The elastic tensor described in Sec 3.4.1 differs at every point in the crystal. Elastic constants are calculated by performing different deformations of the equilibrium unit cell structure and determining the dependence on energy changes. After calculations of elastic constants, first, the elastic stability is determined according to the well-known Born criteria for different crystal systems [52, 71]:

Cubic system:

$$(C_{11} - C_{12}) > 0, C_{11} > 0, C_{44} > 0, C_{11} + 2C_{12} > 0 \tag{3.7}$$

Orthorhombic system:

$$\begin{aligned} C_{11} + C_{12} + C_{33} + 2C_{12} + 2C_{23} > 0; C_{11} + C_{22} > 2C_{12}; \\ C_{22} + C_{33} > 2C_{23}; C_{11} + C_{33} > 2C_{13}; C_{ij} > 0 (i = 1 - 6) \end{aligned} \tag{3.8}$$

Monoclinic system:

$$\begin{aligned} C_{ij} > 0 (ij = 11, 22, 33, 44, 55, 66), \\ C_{11} + C_{22} + C_{33} + 2(C_{12} + C_{13} + C_{23} > 0), \\ (C_{11}C_{55} - C_{12}^2) > 0, (C_{44}C_{66} - C_{46}^2) > 0, C_{22}C_{33} - C_{23} > 0, \\ C_{22}(C_{33}C_{55} - C_{35}^2) + 2C_{23}C_{25}C_{35} - C_{23}^2C_{55} - C_{25}^2C_{33} > 0, \\ 2[C_{15}C_{25}(C_{33}C_{12} - C_{13}C_{23}) + C_{15}C_{35}(C_{22}C_{13} - C_{12}C_{23}) \\ +C_{25}C_{35}(C_{11}C_{23} - C_{12}C_{13})] - [C_{15}^2(C_{11}C_{22} - C_{12}^2) \\ +C_{55}(C_{11}C_{22}C_{33} - C_{11}C_{23}^2 - C_{22}C_{13}^2 - C_{33}C_{12}^2 + C_{12}C_{13}C_{23})] > 0 \end{aligned} \tag{3.9}$$

Trigonal system:

$$\begin{aligned} C_{11} - C_{12} > 0; (C_{11} + C_{12})C_{33} - 2C_{13}^2 > 0; \\ (C_{11} - C_{12})C_{44} - 2C_{14}^2 > 0 \end{aligned} \tag{3.10}$$

The elastic constants calculated from the ab-initio and MEAM potential-based calculations of Fe-Al compounds are presented in Paper I and Paper II. According to our calculations, all Fe-Al compounds in this study fulfilled the elastic stability criteria given in Eqs. (3.7)-(3.10). From these elastic constants, material macroscopic properties such as bulk modulus (B), shear modulus (G), Poisson's ratio (ν) and Young's modulus (Y) are calculated.

Since these crystals are polycrystalline and anisotropic, their mechanical properties are calculated by using the approximation method proposed by Voigt-Reuss-Hill [72–74]. This method provides the upper and lower bounds of the elastic

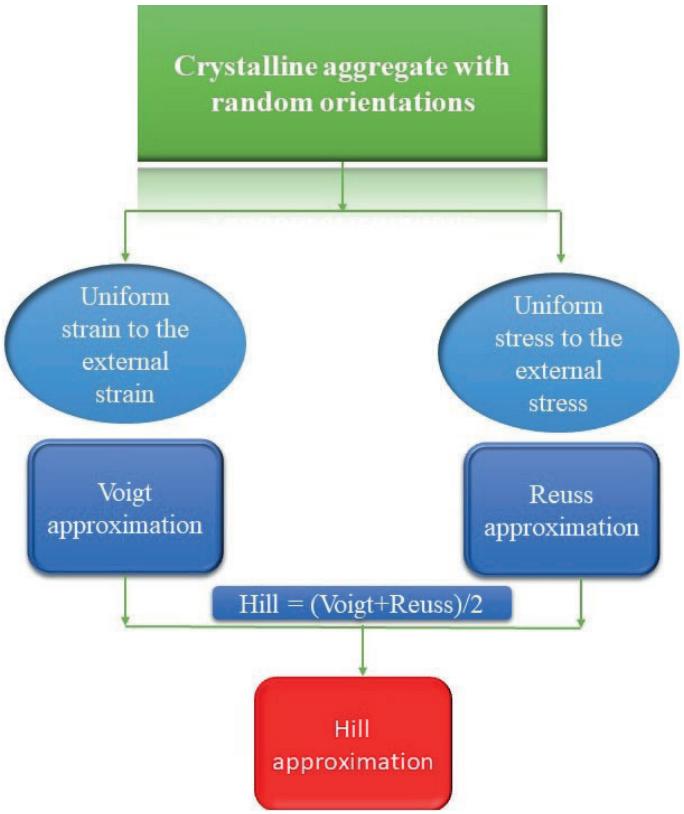

Figure 3.16: Voigt-Reuss-Hill approximation scheme for the calculations of crystalline aggregates.

parameters. The Voigt-Reuss-Hill approximation is an averaging scheme by which anisotropic single-crystal elastic constants can be converted into isotropic polycrystalline elastic moduli. The averaging scheme is explicitly based on three independent theoretical contributions due to Voigt [72], Reuss [73] and Hill [74]. The Voigt and Reuss averages are interpreted as the ratio of average stress to average strain within the composite. The stress and strain are generally unknown in the composite and are expected to be non-uniform. The upper bound (Voigt) and lower bound (Reuss) is found assuming that the strain and stress is everywhere uniform. Fig. 3.16 describes the hierarchy of the Voigt-Reuss-Hill approximation scheme. The Voigt shear modulus (G_V) and Reuss shear modulus (G_R) are given as:

$$G_V = \frac{C_{11} + C_{22} + C_{33} - C_{12} - C_{13} - C_{23}}{15} + \frac{C_{44} + C_{55} + C_{66}}{5} \tag{3.11}$$

$$G_R = \frac{15}{4(S_{11}+S_{22}+S_{33}) - 4(S_{12}+S_{13}+S_{23}) + 3(S_{44}+S_{55}+S_{66})} \tag{3.12}$$

The Voigt bulk modulus (B_V) and Reuss bulk modulus (B_R) are given as:

$$B_R = \frac{1}{(S_{11}+S_{22}+S_{33}) + 2(S_{12}+S_{13}+S_{23})} \tag{3.13}$$

$$B_V = \frac{(C_{11}+C_{22}+C_{33})}{9} + \frac{2}{9}(C_{12}+C_{13}+C_{23}) \tag{3.14}$$

In Eqs. (3.12) and (3.13), S_{ij} is an element of the compliance matrix S_{ij}=C_{ij}^{-1}.

The Voigt-Reuss moduli from Eqs. (3.11-3.14) provide the upper and lower bounds of the shear and bulk modulus. The anisotropic bulk and shear modulus are converted into the isotropic bulk and shear modulus by using the Hill approximation scheme, which uses the Voigt and Reuss average values:

$$G_{\text{Hill}} = \frac{G_R + G_V}{2} \tag{3.15}$$

$$B_{\text{Hill}} = \frac{B_R + B_V}{2} \tag{3.16}$$

Young's modulus (Y) and Poisson's ratio (ν) are calculated from Eq. (3.15) and (3.16):

$$Y_{\text{Hill}} = \frac{9B_{\text{Hill}}G_{\text{Hill}}}{3B_{\text{Hill}} + G_{\text{Hill}}} \tag{3.17}$$

$$\nu_{\text{Hill}} = \frac{3B_{\text{Hill}} - 2G_{\text{Hill}}}{2(3B_{\text{Hill}} + G_{\text{Hill}})} \tag{3.18}$$

The single-crystal bulk modulus, shear modulus, Young's modulus and Poisson's ratio using the VRH approximation for Fe-Al compounds are calculated using the approximation schemes in this thesis.

3.4.3 Interface strength

Tensile strength

For the tensile strength calculations of the bulk and interface structures, virtual tensile tests were performed in the regime of Rigid Grain Shift (RGS) with and

without atomic relaxations [17, 75, 76]. In the RGS approach, the DFT-relaxed equilibrium interface structure is stretched along the normal direction by introducing a vacuum at the interface, and static calculations were performed without atomic relaxation. In the second approach, atoms were stretched in the same way as in the RGS method but allowed to relax during DFT calculations and therefore named RGS+relaxation. These virtual tensile tests result in energy-displacement curves that can be fitted using an extended version of the Universal Binding Energy Relationship (UBER) [77–79]. Rose et al [80] postulated that binding energy-displacement curves can be scaled to a so-called single universal relation, which can be expressed as [80]

$$E_b(d) = |E_b^e| \cdot g(a) \tag{3.19}$$

where E_b^e is the binding energy of the equilibrium structure, d is the displacement of an interface structure and a is the re-scaled displacement given as $a = d/l$. Here l is the characteristic length, which can be approximated by the curvature of the energy-displacement curve at its minimum and is used as a starting point for the fitting procedure,

$$l = \sqrt{\frac{|E_b^e|}{E_b''(0)}} \tag{3.20}$$

If the functional form $g(a)$ is known, we can determine the theoretical strength and critical displacement of any material from the parameters E_b^e, and $E_b^{''}$. For the hydro-static compression/expansion, $g(a)$ is determined to be [81]:

$$g(a) = -(1 + a + P(a))e^{-a} \tag{3.21}$$

By differentiating the energy-displacement curve, the theoretical tensile strength of the atomic structures can be evaluated [77],

$$\sigma_{th}(d) = \frac{\partial E_b}{\partial d} \tag{3.22}$$

The theoretical strength σ_{th} at the maximum of its value is defined as the Ultimate Tensile Strength σ_{UTS}. The value of d at σ_{UTS} is defined as the critical length d_c.

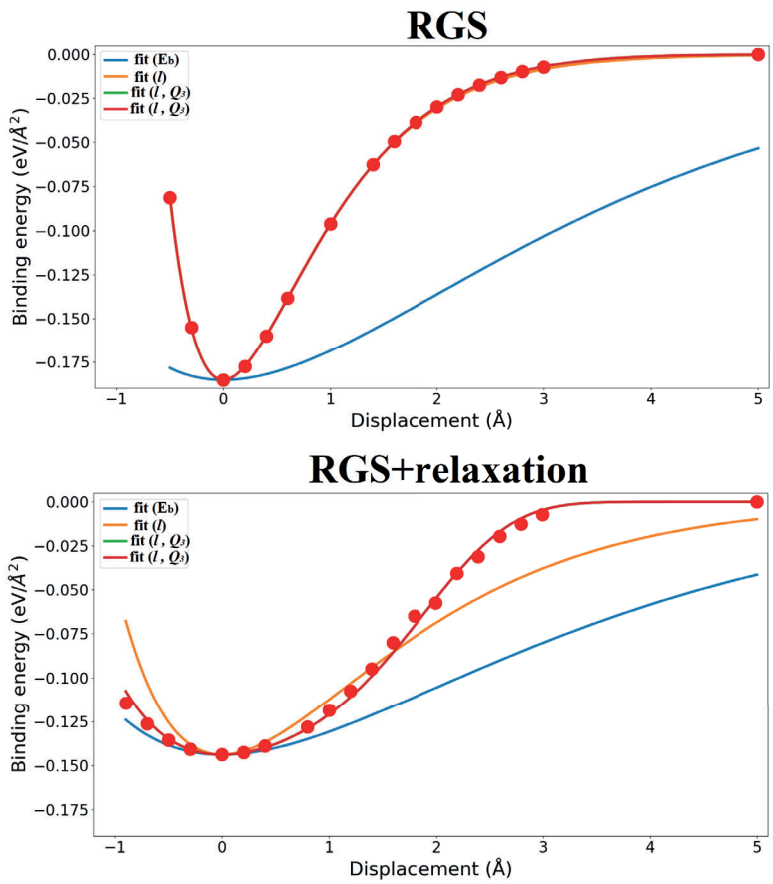

Figure 3.17: Scaling procedure of the energy-displacement curve for the IMCs interface. Green curve is coinciding with red curve.

Scaling of binding energies

In first-principles calculations, the tensile strength can be calculated by applying normal strain directly to the fully relaxed equilibrium interface structure in the z-direction. This virtual tensile testing provides binding energy versus tensile displacement data. As Rose postulated, a metallic bonding-energy curve can be approximately scaled into the universal binding energy relation for the following cases: (i) metallic or bimetallic adhesion (ii) chemisorption on a metal surface, and (iii) cohesion of bulk metals [80]. Although UBER shows good correspondence of binding energy versus displacement for un-relaxed metal surfaces, it is unable to describe the behaviour of tightly bound metals and intermetallics [82]. For this reason, we were unable to find a good fit for the IMC interfaces using the func-

tional form given in Eq. (3.21). To find a good fit capturing the features of binding energy versus displacement, we added another polynomial exponent for $g(a)$ in Eq. (3.19) [81]:

$$E_b(d) = |E_b^e| \cdot g(a) \tag{3.23}$$

$$g(a) = -(1 + a + P(a))e^{-a-Q(a)} \tag{3.24}$$

where a is the rescaled displacement and $|E_b^e|$ is the binding energy of the equilibrium structure. P and Q are polynomials of order two or larger. This expression for $g(a)$ ensures that $g(0) = -1$, $g(a \to \infty) = 0$ and $g'(0) = 0$. The first-order terms are excluded from P and Q since they are related to each other as well as to the characteristic length. To ensure that the fitting behaves well one should only include odd-order terms in the polynomials P and Q.

Using the above approach we found a good fit for both RGS and RGS+relaxation methodologies for the IMC interface structures. Fitting is done by only including a single third-order term in $Q(a)$ while keeping $P(a) = 0$. The fitting is done in the following steps (Fig. 3.17):

1. Blue curve: starting point, we just assumed some reasonable value for $|E_b^e|$ and d.

2. Orange curve: fitting of d.

3. Green curve: fit l together with Q_3 (the coefficient for the third-order term in the polynomial Q).

4. Red curve: Fit $|E_b^e|$, l and Q_3 together.

As can be seen from Fig. 3.17, the characteristic length fits well for the first-order term for the RGS approach. During the relaxation of atomic positions, binding energy lost in breaking a bond is regained during elastic relaxation, which is why the length required to fracture the interface structure increases. For this reason, during the RGS+relaxation method, the characteristic length does not fit to the first-order term polynomial, as it does for the RGS method.

For some materials, the use of a single third-order term in $Q(a)$ was not enough. To find a reasonable fit for such materials, polynomial term $P(a)$ of different orders were also tested.

Features of the energy-displacement curve

Based on the RGS and RGS+relaxation methodologies, the energy-displacement curve is divided into different regions. In the case of the RGS methodology, the curve is continuous and fits adequately to the UBER relation as explained in the previous section. As can be seen in Fig. 3.18, the nominal binding energy increases with the increase in tensile displacement until the energy stabilizes, and interface structures split into two non-interacting free surfaces. The minimum value of the binding energy represents the ideal work of separation W_{sep}. Work of separation W_{sep} is defined as the energy needed to separate an interface structure into two non-interacting free surfaces. The strength calculated using the RGS methodology is overestimated, therefore RGS+relaxation tests are also performed.

RGS+relaxation virtual tensile tests are performed by introducing a vacuum at the interface and then allowing atoms to relax. This results in energy versus displacement curve which does not correspond well with the UBER relation. Fig. 3.18 shows the binding energy versus displacement curve for the RGS+relaxation methodology. This curve is divided into the following regions [77]:

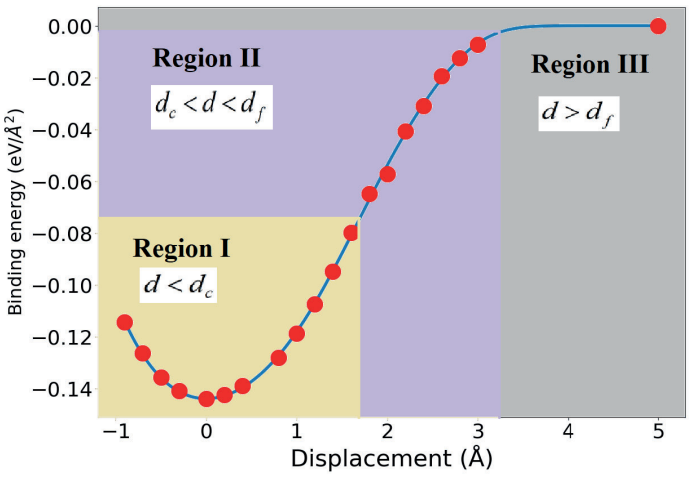

Figure 3.18: Features of the binding energy versus tensile separation curve.

1. Region I ($d < d_c$): At smaller displacements, the binding energy is continuous. An initial crack introduced can, therefore, be recovered by elastic relaxation and surfaces are reconnected. The d_c can be determined as follows,

$$d_c = \epsilon_c d_0 + d_0 \tag{3.25}$$

where ϵ_c and d_0 are the critical strain value at the maximum tensile stress and equilibrium length of the supercell, respectively. The materials during the virtual tensile tests reach the maximum tensile stress at d_c

2. Region II ($d_c < d < d_f$): This region is defined as the instability region. The purple region in Fig. 3.18 indicate the range and the crack introduced in Region 1 can here no longer be healed. The range of this region can be calculated by the following relation:

$$d_{\text{instability}} = d_f - d_c \tag{3.26}$$

where d_f is the final fracture length. We define d_f to be the value of d where the binding energy reached -0.003 eV/Å^2. The final fracture length can be regarded as the limiting displacement, after which the interface structures are completely separated into the corresponding relaxed bulk surfaces.

3. Region III ($d > d_f$) : At larger separation distances; the energy-displacement curve levels out. The fractured surfaces are attracted to their corresponding blocks after overcoming the energy barrier, hence the energy-displacement curve stabilizes and the surfaces are totally separated.

Shear strength

For the shear strength calculations the interface structures were moved along the **a** and **b** directions, depending on the ORs between related interfaces, and atoms were allowed to relax along the **c** direction to remove strain. Moreover, to remove any periodic interaction along the [001] direction, a vacuum layer of >10 Å was introduced. A series of incremental strains were introduced along the respective slip directions, and atoms were allowed to relaxed along the normal direction using a conjugate gradient relaxation algorithm. Figure 3.18 shows a schematic example of shear displacement between Crystal 1 and 2. Crystal 2 was moved with respect to Crystal 1 along **a** and **b** directions. The same procedure was adopted for all the interface structures.

These calculations result in the total energy as a function of shear displacement. Since the shear system is periodic along the shearing direction, the shifted slab energy is defined as a Fourier series:

$$E_s(d) = E_0(0) + \sum_{i=1}^{\infty}[A_i \cos(k_i d) + B_i \sin(k_i d)] \tag{3.27}$$

where k_i=$\frac{2\pi i}{\lambda}$ and λ is the periodicity along the shear direction. To find a good fit, a Fourier series of order 3 was used for most of the curves. $E_s(d)$ and $E_0(0)$ are

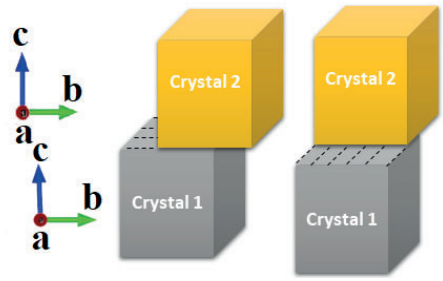

Figure 3.19: Schematic illustration of shear displacement.

the total energies of the shifted and un-shifted supercell, respectively [83], of the interface structures and d is the shear displacement. The shear stress is calculated by differentiating Eq. 3.27,

$$\gamma_s(d) = \frac{1}{A}\frac{\partial E_s}{\partial d} \tag{3.28}$$

where A is the interface area.

Chapter 4

Summary

> "If you thought that science was certain — well, that is just an error on your part."
>
> Richard Feynman (1918-1988)

In this chapter, the articles on which this thesis is based on will be summarised. This will be followed by overall conclusion, together with a brief discussion of the main challenges and limitations of the present theoretical results, and their validity with respect the joint strength of real structures. Finally some methodological perspectives are presented.

4.1 Summary of articles

The main objective of this thesis is to characterize the influence of Fe-Al intermetallics on the joint strength of aluminum and steel joints. The scope of this thesis is mainly limited to the Fe_2Al_5, Fe_4Al_{13} and α-AlFeSi intermetallics. However, we also performed MEAM simulations on the FeAl, Fe_3Al and $FeAl_2$ phases to identify the computational reliability of the MEAM method in comparison to EAM, DFT, and long-range analytical embedded atom method (LAEAM) methods. Moreover, it provided us the opportunity to find a MEAM potential suitable for finding good initial guesses for complex Fe-Al interfaces (see subsection 3.1.2).

4.1.1 Paper I

First-principles calculations were performed on bulk single-crystal unit cells of Fe_2Al_5 and Fe_4Al_{13} intermetallics. Based on single-crystal elastic constant cal-

culations, the following conclusions are drawn from this study. (i) both Fe_2Al_5 and Fe_4Al_{13} compounds were found to be thermodynamically and mechanically stable. Based on the calculation of formation enthalpy, Fe_2Al_5 was found to be thermodynamically more stable than Fe_4Al_{13}; (ii) both compounds were found to be brittle in nature with Fe_4Al_{13} more brittle than Fe_2Al_5, (iii) based on the shear modulus and Young's modulus, Fe_2Al_5 was found to be harder and stiffer as compared to Fe_4Al_{13}, (iv) Fe_2Al_5 showed higher bulk modulus values than Fe_4Al_{13}, which indicates that Fe_2Al_5 is more resistant to compression than Fe_4Al_{13}, (v) both compounds were found to be mechanically anisotropic, however, Fe_2Al_5 showed higher directional dependence of Young's modulus than Fe_4Al_{13}. Moreover, a calculation of the electron localization function indicated covalent bonding between Al-Al atoms and metallic bonding between Fe-Fe atoms for both compounds. On the other hand, bonding between Al-Fe showed mixed behavior and depends on the orientation of the structure.

4.1.2 Paper II

(Pre-print)

Modified embedded atom method (MEAM) based simulations were performed of Fe-Al bulk intermetallic phases to identify the accuracy and applicability of the MEAM potentials for the Fe-Al system. To assess the degree of the uncertainty of the calculations, structural and mechanical properties calculated by the MEAM force-field was compared to density functional theory, the embedded atom method (EAM), the long-range analytical embedded atom method (LAEAM) and experiments. The other main objective of this study was to identify the best computational methodology available so far, for as realistic as possible predictions of structural and mechanical properties of the Fe-Al compounds.

Based on MEAM calculations of the heat of formation and elastic constants, all Fe-Al compounds (FeAl, $FeAl_2$, Fe_2Al_5, $FeAl_3$ and Fe_3Al) were found to be thermodynamically and mechanically stable. Comparisons with other theoretical and experimental studies identified uncertainties in computational methodologies. Generally, it has been found that semi-empirical potentials are unable to provide realistic insights about high-symmetry compounds. It has been generally accepted that Fe_2Al_5 and $FeAl_3$ are brittle, but EAM and MEAM simulations predicted a ductile nature of these compounds, which is in contradiction with experiments. However, DFT was successfully able to predict the brittle nature of these compounds. Moreover, these comparisons and studies were performed without considering any crystal defects, so the calculated values are expected to be over-estimated as compared to the experiments.

4.1.3 Paper III, IV and V

Systematic studies were performed by virtual tensile and shear strength calculations of the Al//Fe_4Al_{13}, Al//α-AlFeSi,α-AlFeSi // Fe_4Al_{13}, Fe_4Al_{13} // Fe_2Al_5 and Fe_2Al_5 // Fe interface structures by using the density functional theory method. Moreover, to quantify the weakest zone in the interface structure, bulk virtual tensile strength was also evaluated for the Al, Fe_4Al_{13}, Fe_2Al_5 and Fe phases. Virtual tensile calculations for all interface structures were performed in the regime of RGS without atomic relaxations and RGS+relaxation with atomic relaxations. The contributions from these papers are not only limited to finding the strength of these interface structures but also to point out the importance of the RGS+relaxation methodology for more realistic predictions of the virtual tensile strength.

The RGS+relaxation virtual tensile strength calculations indicated that the Fe_2Al_5// Fe interface is the strongest, followed by the α-AlFeSi // Fe_4Al_{13}, Fe_4Al_{13} // Fe_2Al_5, Al//α-AlFeSi and Al//Fe_4Al_{13} interfaces. Furthermore, calculations gave insights into the structure of the charge depletion region in Fe_4Al_{13}, which significantly compromises its bonding strength. It was found that Fe_4Al_{13} is highly anisotropic in nature, and the presence of this phase can compromise the joint strength. In terms of virtual shear strength, Fe_2Al_5//Fe showed the lowest virtual shear strength along the $< 001 >$ direction followed by Al//α-AlFeSi and Al//Fe_4Al_{13}. α-AlFeSi // Fe_4Al_{13} and Fe_4Al_{13} // Fe_2Al_5 interfaces showed comparatively higher shear strength as compared to all other interfaces. However, the α-AlFeSi // Fe_4Al_{13} interface seems to have the highest shear strength. Table 4.1 and 4.2 show the calculated virtual tensile and shear strengths of the interface structures.

Moreover, the RGS+relaxation methodology helped us to predict the ductile and brittle failure mechanism of the interface structures. The energy-displacement curve in the RGS+relaxation method was divided into three distinct regions which helped us to explore the physics at different displacement lengths. Due to this unique feature of this method, it was argued to use the extra polynomial term in the UBER relation for finding a better fit for interface structures. Based on the RGS+relaxation method, brittle failure was determined based on the range of the instability region, i.e., the higher the range of the region the higher the ductile behavior. It is well known, Al is a highly ductile material. Al (210) bulk is therefore taken as a reference with 3.17 Å range of the instability region, Fe_2Al_5 // Fe showed the smallest range of the instability region (0.79 Å), which indicates that this interface structure is most brittle in nature. α-AlFeSi // Fe_4Al_{13} showed the largest range (1.55 Å) followed by Al // Fe_4Al_{13} (1.38 Å), Fe_2Al_5 // Fe_4Al_{13} (1.10 Å) and Al // α-AlFeSi (0.92 Å). To summarize, the presence of Al atoms at the

interface increases the range of the instability region with the exception of the Al // α-AlFeSi. The weak bonding between Al-Si atoms at the interface as observed by the total charge density plots in the Al // α-AlFeSi interface is assumed to cause the lower range of the instability region and brittle failure.

These papers enhance our understanding of the influence of Fe_2Al_5, Fe_4Al_{13} and α-AlFeSi intermetallic phases on the joint strength of aluminum and steel. Systematic studies have been performed to characterize the mechanical strength of Fe_2Al_5, Fe_4Al_{13} and α-AlFeSi compounds and interfaces. However, these papers do not consider crystallographic defects and effects of temperature.

Table 4.1: Virtual tensile strength of interface structures.

Interface	σ_{UTS} (RGS) (GPa)	σ_{UTS} (RGS+relaxation) (GPa)
Al // Fe_4Al_{13}	13.17	9.85
Al // α-AlFeSi	17.27	10.92
Fe_4Al_{13} // α-AlFeSi	17.79	11.10
Fe_4Al_{13} // Fe_2Al_5	17.32	14.48
Fe_2Al_5 // Fe	33.03	23.88

Table 4.2: Virtual shear strength of interface structures.

Interface	Shear stress (Lowest) (GPa)	Shear stress (Highest) (GPa)
Al // Fe_4Al_{13}	5.11 <101>	7.65 <101>
Al // α-AlFeSi	2.23 <101>	3.14 <100>
Fe_4Al_{13} // α-AlFeSi	6.50 <011>	6.81 <110>
Fe_4Al_{13} // Fe_2Al_5	5.15 <020>	5.92 <001>
Fe_2Al_5 // Fe	0.97 <001>	4.74 <100>

4.1.4 Appendix article A

This is a preliminary article, in which we studied the simple Al and Fe interface without any IMC layer. This article had the following aims:

- We tested our methodology for the building of low lattice misfit interface structures.
- Although it is inevitable to avoid the development of IMCs during the welding of aluminum and steel, this study is still relevant to be considered as a

reference for investigating the effect of IMC layers on the mechanical properties of the joint. We also devised a methodology for the calculation of the work of separation. The purpose of calculating W_{sep} for the Al//Fe interface was to make comparisons with W_{sep} values of Al // IMC, IMC // IMC, and IMC // Fe interfaces.

Table 4.3 lists the W_{sep} values for all interfaces. It is clear from the table that the pure Al//Fe interface has a higher value of W_{sep} than all IMCs interfaces. This indicates that the presence of the IMC layers lowers the interfacial strength. Although this conclusion is trivial, it nevertheless validates our methodology and approach.

Table 4.3: Virtual tensile strength of interface structures.

Interface	W_{sep} (J/m^2)
Al // Fe	5.84
Al // Fe_4Al_{13}	2.24
Al // α-AlFeSi	2.26
Fe_4Al_{13} // α-AlFeSi	2.95
Fe_4Al_{13} // Fe_2Al_5	3.11
Fe_2Al_5 // Fe	4.45

4.2 Overall summary

4.2.1 Main conclusions

The aim of this Ph.D. thesis to contribute to an improved fundamental understanding of the mechanical behavior of Fe-Al welding joints. This was obtained by performing a systematic study of mechanical strength of the individual phases (Al and Fe) and Al-Fe and α-AlFeSi IMCs and their relevant interfaces via ab-initio calculations. Based on the articles I-V and A the following main conclusions can be drawn:

- Compared to the interfaces, bulk IMCs showed the highest strengths, which indicates that failure is more likely to initiate from the interface region than the bulk region for these IMCs.
- The calculated work of separation and ultimate tensile strengths are shown in Fig. 4.1. The interfaces with higher work of separation values showed the

higher ultimate tensile strength. Moreover, the ranking of the IMC interfaces based on the mechanical strength values can also be seen. An interface with higher Fe content shows higher strength values.

- Shear strength for all interface structures were found to be significantly lower than the virtual tensile strengths (cf. Fig. 4.2). The interfaces with more Al atoms at the interface showed comparatively higher shear-strength values than the interfaces with more Fe and Si atoms. To summarize, Fe atoms found to develop stronger tensile but lower shear strengths than the Al atoms at the interface.

- Overall Fe-Al and α-AlFeSi IMCs were found to have negative effect on the strength of aluminum-steel joint.

These conclusions are expected to provide useful insights into the role of individual IMCs and help experimentalists to develop strategies for welding methods. The theoretical calculations also provide valuable results about intrinsic strength, which can be important input for higher scale modelling approaches (also including defects), and hopefully also serve as basis for future, more sophisticated multiscale models.

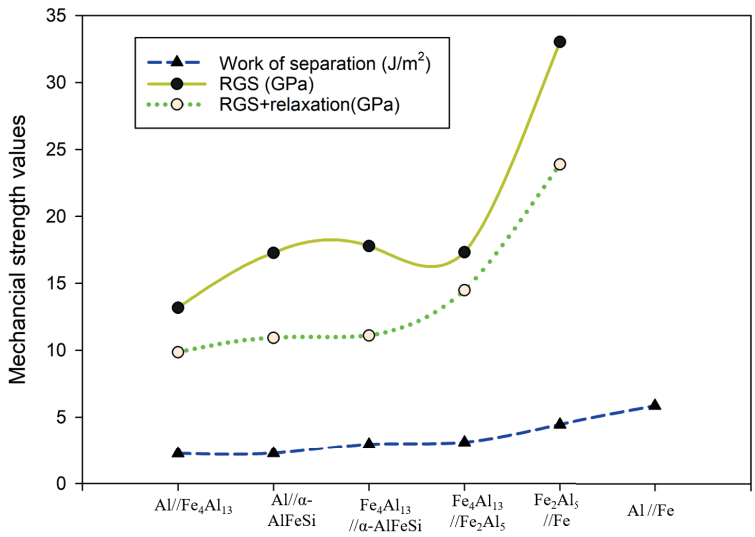

Figure 4.1: Relation between different calculated mechanical values such as work of separation and the ultimate tensile strengths (RGS and RGS+relaxation approaches) for the interface structures.

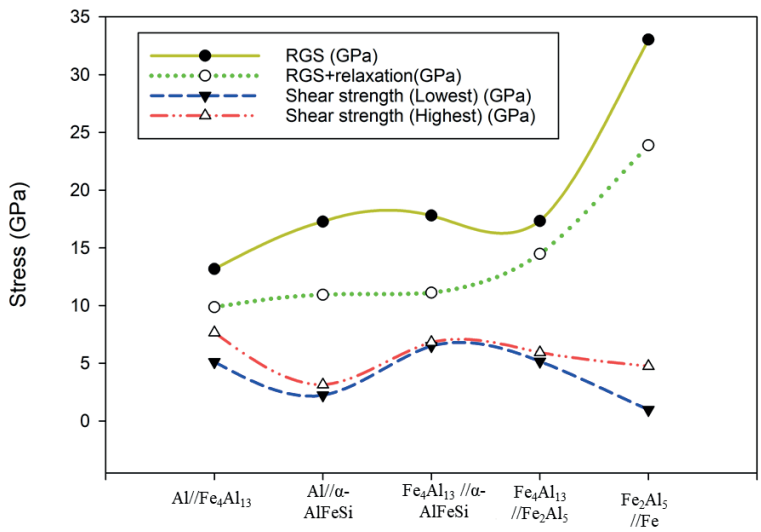

Figure 4.2: Relation between ultimate tensile and shear strengths for the interface structures.

4.2.2 Methodological perspectives, challenges and limitations

The research articles in this thesis contribute to the building of atomic interface structures and their bulk and interfacial strengths by DFT and MEAM based approaches. This Ph.D. project explored the applicability and reliability of the MEAM potential approach for predicting mechanical strengths. To ensure the reliability and uncertainty of our calculations, we compared the calculated values with other theoretical and experimental literature. Results indicated that the MEAM potential scheme can provide good structural properties, but it showed huge discrepancies in the mechanical behavior predictions for Fe-Al compounds. This Ph.D. proposes that the MEAM potential approach should only be applied for finding good initial interface structures, but it is unsuitable for inferring mechanical behavior prediction. Therefore, this thesis mostly comprises of DFT calculations.

In the later part of this Ph.D. thesis, interfacial properties are calculated by using the generalized form of UBER for tensile and Fourier series for shear strength calculations. This thesis used RGS and RGS+relaxation based approaches to identify the ultimate tensile strengths of the interface structures. Since RGS does not involve the atomic relaxations during the virtual tensile testing, the RGS+relaxation based approach is proposed to be more reliable. However, this approach presented an extra challenge of finding a reasonable fit with UBER. We therefore introduced an additional polynomial term in the UBER relation to find a reasonable fit for the RGS+relaxation method. Before adopting this approach, this fitting technique was

evaluated for different Al alloy compositions and grain boundaries and it showed reasonable agreement with literature [81]. However, due to the lack of data for these IMCs, we could not compare the calculated values with other literature. Nevertheless, comparisons of structural parameters for the bulk IMCs from our DFT calculations showed good agreement with other literature [52, 53, 60].

The approach and methods applied in this work has the following challenges and limitations:

- Among the main limitations of all the articles discussed in this thesis is the lack of consideration of crystallographic defects. Such microstructure defects can have a significant effect on the mechanical properties of the IMCs and their interfaces- and may modify the conclusions with respect to relative strength based on the IMCs' intrinsic strength properties. Extended defects like dislocations and micro-/nano voids are probably the most important defects that are not included in this work. Even though there exist examples in the literature where the defects are considered in the frame of first principles [84, 85], they generally live in a length scale above DFT and are therefore outside the scope of this work.

- The role of impurities and the effect of temperature on the mechanical strengths of IMCs: For example, Medvedeva et al. [86] studied the role of C, Mn and Al impurities in a fcc Fe matrix by first principles. They demonstrated the effect of impurities on the intrinsic stacking fault energy (SFE) and found SFE is highly sensitive to the concentration of impurities in the vicinity of stacking fault defect. Song et al. [87] recently addressed the role of vacancies on the mechanical properties of B2 FeAl intermetallic by first principles. They found the mechanical change of IMC from brittle to ductile with an increase in the vacancy concentration and also observed an increase in equilibrium concentration of vacancies with an increase in temperature.

- Generally, Fe_2Al_5, Fe_4Al_{13} and α-AlFeSi are non-magnetic IMCs [88, 89]. However, studies have shown an increase in magnetism with an increase of substitutional Fe atoms, temperature, and anti-phase grain boundaries for Fe-Al IMCs [90, 91]. In this work, we did perform spin-polarized calculations for the IMCs, and these calculations indicated that spin is a second order effect. For this reason, magnetism was not considered for virtual tensile and shear strength calculations of Fe-Al IMCs.

- Lateral contraction (Poisson effect) during virtual tensile tests was also not considered in this work. It is generally accepted to perform tensile calculations by neglecting the Poisson effect as we often make comparative stud-

ies. However, Tian et al. [92] studied the Poisson effect upon stretching and found that it remarkably reduces the total energy of the grain-boundary system.

- Since this work does not include extended defects (dislocation, micro/nanovoids), the prediction of brittleness/ductility from the binding energy versus the separation curve is not defined in a classical sense as relevant for real microstructures and materials (in which brittleness and ductility is related to the mobility of dislocations). But it provides an approximate qualitative comparison of different Fe-Al IMC interfaces indicating the intrinsic brittle/ductile failure mechanism.

4.2.3 Future perspectives

1. The study of the MEAM potential was performed for bulk Fe-Al IMC compounds. However, the MEAM potential was used in this work for finding good initial interface structures due to the suitability of the MEAM potentials for Fe and Al. Hence there is a need for the improvement of such potentials. Moreover, during the development of such potential, the reliability of the mechanical properties should also be tested.

2. In this work, the main focus was on the Fe_2Al_5, Fe_4Al_{13} and α-AlFeSi intermetallic phases. Depending on the welding methodology and temperature reached at the joint, many other phases such as FeAl, $FeAl_2$, Fe_2Al and many other Al-Fe-Si intermetallics have already been observed and found at aluminum-steel joints. These phases still need to be studied further.

3. This study was performed without considering any crystallographic defects such as point defects, line defects, planar or bulk defects. This results in over-estimation of values calculated from these simulations. For example, macroscopic tensile and shear strengths will be much lower than the virtual tensile and shear strength calculations of this study. Given this, there is a need for systematically studying the influence of crystallographic defects on the mechanical properties of Fe-Al and Al-Fe-Si compounds.

4. These simulations were performed at 0K. The temperature could have a significant effect on the mechanical properties of these compounds, and this should be considered and scrutinized in future studies. Since all our DFT calculations neglect temperature effects, molecular dynamics or ab-initio molecular dynamics-based approaches should be adopted for an enhanced understanding of the temperature effects on these compounds and interfaces.

5. There is a need to link the atomistic simulations with the macroscopic failure process by using molecular dynamics or finite element modeling. The work reported in this thesis can be used as an input to describe the macroscopic failure mechanism of aluminum-steel joints by a FEM method. Figure 1.1 shows the strategy for linking atomistic simulations with a macroscopic model inspired by the experimental observations.

Bibliography

[1] D. Sholl and J. A. Steckel, *Density functional theory: a practical introduction*. John Wiley & Sons, 2011.

[2] E. Bitzek, P. Koskinen, F. Gähler, M. Moseler, and P. Gumbsch, "Structural relaxation made simple," *Physical Review Letters*, vol. 97, no. 17, p. 170201, 2006.

[3] H.-C. Chen, A. J. Pinkerton, L. Li, Z. Liu, and A. T. Mistry, "Gap-free fibre laser welding of Zn-coated steel on Al alloy for light-weight automotive applications," *Materials & Design*, vol. 32, no. 2, pp. 495–504, 2011.

[4] R. Qiu, C. Iwamoto, and S. Satonaka, "Interfacial microstructure and strength of steel/aluminum alloy joints welded by resistance spot welding with cover plate," *Journal of Materials Processing Technology*, vol. 209, no. 8, pp. 4186–4193, 2009.

[5] G. Sierra, P. Peyre, F. Deschaux-Beaume, D. Stuart, and G. Fras, "Steel to aluminium key-hole laser welding," *Materials Science and Engineering: A*, vol. 447, no. 1, pp. 197–208, 2007.

[6] H. Springer, A. Kostka, E. Payton, D. Raabe, A. Kaysser-Pyzalla, and G. Eggeler, "On the formation and growth of intermetallic phases during interdiffusion between low-carbon steel and aluminum alloys," *Acta Materialia*, vol. 59, no. 4, pp. 1586–1600, 2011.

[7] F. Haddadi, D. Strong, and P. Prangnell, "Effect of zinc coatings on joint properties and interfacial reactions in aluminum to steel ultrasonic spot welding," *JOM*, vol. 64, no. 3, pp. 407–413, 2012.

[8] C. Ageorges, L. Ye, and M. Hou, "Advances in fusion bonding techniques for joining thermoplastic matrix composites: a review," *Composites Part A: Applied Science and Manufacturing*, vol. 32, no. 6, pp. 839–857, 2001.

[9] S. Kalpakjian, S. R. Schmid, K. Sekar *et al.*, *Manufacturing engineering and technology*. Pearson Publications.

[10] R. J. Churchill, U. Varshney, H. P. Groger, and J. M. Glass, "Laser brazing for ceramic-to-metal joining," Apr. 18 1995, US Patent 5,407,119.

[11] K. Suganuma, Y. Miyamoto, and M. Koizumi, "Joining of ceramics and metals," *Annual Review of Materials Science*, vol. 18, no. 1, pp. 47–73, 1988.

[12] T. Sakiyama, G. Murayama, Y. Naito, K. Saita, Y. M. H. Oikawa, and T. Nose, "Dissimilar metal joining technologies for steel sheet and aluminum alloy sheet in auto body," *Nippon Steel & Sumitomo Metal Corp., Tokyo, Nippon Steel Technical Report*, vol. 103, pp. 91–98, 2013.

[13] S. Imaizumi, "Welding of aluminium to dissimilar metals," *Welding International*, vol. 10, no. 8, pp. 593–604, 1996.

[14] S. Yang, J. Zhang, J. Lian, and Y. Lei, "Welding of aluminum alloy to zinc coated steel by cold metal transfer," *Materials & Design*, vol. 49, pp. 602–612, 2013.

[15] S. Niu, S. Chen, H. Dong, D. Zhao, X. Zhang, X. Guo, and G. Wang, "Microstructure and properties of lap joint between Aluminum Alloy and galvanized steel by CMT," *Journal of Materials Engineering and Performance*, vol. 25, no. 5, pp. 1839–1847, 2016.

[16] Y. Shi, J. Li, G. Zhang, J. Huang, and Y. Gu, "Corrosion behavior of aluminum-steel weld-brazing joint," *Journal of Materials Engineering and Performance*, vol. 25, no. 5, pp. 1916–1923, 2016.

[17] G. Zhang, M. Chen, Y. Shi, J. Huang, and F. Yang, "Analysis and modeling of the growth of intermetallic compounds in aluminum-steel joints," *RSC Advances*, vol. 7, no. 60, pp. 37 797–37 805, 2017.

[18] S. Lan, X. Liu, and J. Ni, "Microstructural evolution during friction stir welding of dissimilar aluminum alloy to advanced high-strength steel," *The International Journal of Advanced Manufacturing Technology*, vol. 82, no. 9-12, pp. 2183–2193, 2016.

[19] G. Sorger, H. Wang, P. Vilaça, and T. G. Santos, "FSW of aluminum AA5754 to steel DX54 with innovative overlap joint," *Welding in the World*, vol. 61, no. 2, pp. 257–268, 2017.

[20] K.-K. Wang, L. Chang, D. Gan, and H.-P. Wang, "Heteroepitaxial growth of Fe_2Al_5 inhibition layer in hot-dip galvanizing of an interstitial-free steel," *Thin Solid Films*, vol. 518, no. 8, pp. 1935–1942, 2010.

[21] A. Bouayad, C. Gerometta, A. Belkebir, and A. Ambari, "Kinetic interactions between solid iron and molten aluminium," *Materials Science and Engineering: A*, vol. 363, no. 1, pp. 53–61, 2003.

[22] D. Naoi and M. Kajihara, "Growth behavior of Fe_2Al_5 during reactive diffusion between Fe and Al at solid-state temperatures," *Materials Science and Engineering: A*, vol. 459, no. 1, pp. 375–382, 2007.

[23] Y. Chen, A. Gholinia, and P. Prangnell, "Interface structure and bonding in abrasion circle friction stir spot welding: a novel approach for rapid welding aluminium alloy to steel automotive sheet," *Materials Chemistry and Physics*, vol. 134, no. 1, pp. 459–463, 2012.

[24] W.-J. Cheng and C.-J. Wang, "Study of microstructure and phase evolution of hot-dipped aluminide mild steel during high-temperature diffusion using electron backscatter diffraction," *Applied Surface Science*, vol. 257, no. 10, pp. 4663–4668, 2011.

[25] L. Agudo, D. Eyidi, C. H. Schmaranzer, E. Arenholz, N. Jank, J. Bruckner, and A. R. Pyzalla, "Intermetallic Fe_xAl_y-phases in a steel/Al-alloy fusion weld," *Journal of Materials Science*, vol. 42, no. 12, pp. 4205–4214, 2007.

[26] W. M. C. Foulkes and R. Haydock, "Tight-binding models and density-functional theory," *Physical Review B*, vol. 39, no. 17, p. 12520, 1989.

[27] R. G. Parr, "Density functional theory of atoms and molecules," in *Horizons of Quantum Chemistry*. Springer, 1980, pp. 5–15.

[28] J. Nocedal and S. J. Wright, *Numerical Optimization*. Springer-Verlag New York Incorporated, 1999.

[29] W. H. Press, S. A. Teukolsky, W. T. Vetterling, and B. P. Flannery, *Numerical recipes 3rd edition: The art of scientific computing*. Cambridge university press, 2007.

[30] T. Schlick, *Molecular modeling and simulation: an interdisciplinary guide: an interdisciplinary guide*. Springer Science & Business Media, 2010, vol. 21.

[31] R. O. Jones and O. Gunnarsson, "The density functional formalism, its applications and prospects," *Reviews of Modern Physics*, vol. 61, no. 3, p. 689, 1989.

[32] W. Kohn and L. J. Sham, "Self-consistent equations including exchange and correlation effects," *Physical Review*, vol. 140, no. 4A, p. A1133, 1965.

[33] J. P. Perdew, K. Burke, and M. Ernzerhof, "Generalized gradient approximation made simple," *Physical Review Letters*, vol. 77, no. 18, p. 3865, 1996.

[34] R. G. Parr, "Density functional theory of atoms and molecules," pp. 5–15, 1980.

[35] J. D. Patterson, "Density-functional theory of atoms and molecules: Robert G. Parr and Weitao Yang. Oxford University Press, New York, and Clarendon Press, Oxford (1989). US 55. 333 pages," 1989.

[36] P. V. Medeiros, "Electronic properties of complex interfaces and nanostructures," Ph.D. dissertation, Linköping University Electronic Press, 2015.

[37] J. P. Perdew, "Density-functional approximation for the correlation energy of the inhomogeneous electron gas," *Physical Review B*, vol. 33, no. 12, p. 8822, 1986.

[38] D. C. Langreth and M. Mehl, "Beyond the local-density approximation in calculations of ground-state electronic properties," *Physical Review B*, vol. 28, no. 4, p. 1809, 1983.

[39] A. D. Becke, "Density-functional exchange-energy approximation with correct asymptotic behavior," *Physical Review A*, vol. 38, no. 6, p. 3098, 1988.

[40] J. Hafner, "Ab-initio simulations of materials using VASP: Density-functional theory and beyond," *Journal of Computational Chemistry*, vol. 29, no. 13, pp. 2044–2078, 2008.

[41] P. E. Blöchl, "Projector augmented-wave method," *Physical review B*, vol. 50, no. 24, p. 17953, 1994.

[42] H. J. Monkhorst and J. D. Pack, "Special points for brillouin-zone integrations," *Physical Review B*, vol. 13, no. 12, p. 5188, 1976.

[43] M. Baskes, "Modified embedded-atom potentials for cubic materials and impurities," *Physical Review B*, vol. 46, no. 5, p. 2727, 1992.

[44] B. Jelinek, S. Groh, M. F. Horstemeyer, J. Houze, S.-G. Kim, G. J. Wagner, A. Moitra, and M. I. Baskes, "Modified embedded atom method potential for Al, Si, Mg, Cu, and Fe alloys," *Physical Review B*, vol. 85, no. 24, p. 245102, 2012.

[45] J. Schneider, J. Hamaekers, S. T. Chill, S. Smidstrup, J. Bulin, R. Thesen, A. Blom, and K. Stokbro, "ATK-forcefield: a new generation molecular dynamics software package," *Modelling and Simulation in Materials Science and Engineering*, vol. 25, no. 8, p. 085007, 2017.

[46] "Atomistix toolkit version 2017.0, synopsys quantumwise a/s," www.quantumwise.com.

[47] J. Nocedal, "Updating quasi-newton matrices with limited storage," *Mathematics of Computation*, vol. 35, no. 151, pp. 773–782, 1980.

[48] S. M. Arbo, T. Bergh, H. Solhaug, I. Westermann, and B. Holmedal, "Influence of thermomechanical processing sequence on properties of AA6082-IF steel cold roll bonded composite sheet," *Procedia Manufacturing*, vol. 15, pp. 152–160, 2018.

[49] P. Liu and G. Dunlop, "Crystallographic orientation relationships for Al-Fe and Al-Fe-Si precipitates in aluminium," *Acta Metallurgica*, vol. 36, no. 6, pp. 1481–1489, 1988.

[50] M. Z. Khalid, J. Friis, P. H. Ninive, K. Marthinsen, and A. Strandlie, "First-principles study of tensile and shear strength of Fe_2Al_5//Fe interface," *in Preparation*, 2019.

[51] ——, "Modified embedded atom method potential for Fe-Al intermetallic mechanical strength: A comparative analysis of atomistic simulations," *Work in progress*, 2019.

[52] Y. Liu, X. Chong, Y. Jiang, R. Zhou, and J. Feng, "Mechanical properties and electronic structures of Fe-Al intermetallic," *Physica B: Condensed Matter*, vol. 506, pp. 1–11, 2017.

[53] C.-H. Zhang, S. Huang, J. Shen, and N.-X. Chen, "Structural and mechanical properties of Fe-Al compounds: An atomistic study by EAM simulation," *Intermetallics*, vol. 52, pp. 86–91, 2014.

[54] W. G. Moffatt, "The handbook of binary phase diagrams. vol. 1-2," 1976.

[55] P. G. Gonzales-Ormeño, H. M. Petrilli, and C. G. Schön, "Ab-initio calculations of the formation energies of bcc-based superlattices in the Fe-Al system," *Calphad*, vol. 26, no. 4, pp. 573–582, 2002.

[56] W. Pearson, "A Handbook of Lattice Spacings and Structures of Metals and Alloys: Pergamon Press, London, New York, Paris, los Angeles. 1958. 1044," , vol. 13, no. 8, p. 516, 1958.

[57] C. Vailhe and D. Farkas, "Shear faults and dislocation core structure simulations in B2 FeAl," *Acta Materialia*, vol. 45, no. 11, pp. 4463–4473, 1997.

[58] P. D. Desai, "Thermodynamic properties of selected binary aluminum alloy systems," *Journal of Physical and Chemical Reference Data*, vol. 16, no. 1, pp. 109–124, 1987.

[59] E. A. Brandes and G. Brook, *Smithells metals reference book*. Elsevier, 2013.

[60] P. Villars, "Pearson's Handbook—Desk Edition: Crystallographic Data for Intermetallic Phases," *ASM International: Materials Park, OH*, pp. 1727–1729, 1998.

[61] R. Hultgren, P. D. Desai, D. T. Hawkins, M. Gleiser, and K. K. Kelley, "Selected values of the thermodynamic properties of binary alloys," National Standard Reference Data System, Tech. Rep., 1973.

[62] M. Z. Khalid, J. Friis, P. H. Ninive, K. Marthinsen, and A. Strandlie, "DFT calculations based insight into bonding character and strength of Fe_2Al_5 and Fe_4Al_{13} intermetallics at Al-Fe joints," *Procedia Manufacturing*, vol. 15, pp. 1407–1415, 2018.

[63] M. Cooper, "The crystal structure of the ternary alloy α (AlFeSi)," *Acta Crystallographica*, vol. 23, no. 6, pp. 1106–1107, 1967.

[64] "Fe_2Al_5 (feal2.8) crystal structure: Datasheet from "pauling file multinaries edition – 2012" in springermaterials (https://materials.springer.com/isp/crystallographic/docs/sd_0261950)," copyright 2016 Springer-Verlag Berlin Heidelberg & Material Phases Data System (MPDS), Switzerland & National Institute for Materials Science (NIMS), Japan. [Online]. Available: https://materials.springer.com/isp/crystallographic/docs/sd_0261950

[65] A. R. Leach and A. R. Leach, *Molecular modelling: principles and applications*. Pearson education, 2001.

[66] J. Nocedal and S. Wright, "Numerical optimization, "Springer-Verlag New York Incorporated"."

[67] D. Sheppard, R. Terrell, and G. Henkelman, "Optimization methods for finding minimum energy paths," *The Journal of Chemical Physics*, vol. 128, no. 13, p. 134106, 2008.

[68] W. H. Press, S. A. Teukolsky, W. T. Vetterling, and B. P. Flannery, *FORTRAN numerical recipes*. Cambridge England, 1996, vol. 1.

[69] H. Group. (2019) MS Windows NT kernel description. [Online]. Available: https://theory.cm.utexas.edu/henkelman/

[70] J. F. Nye *et al.*, "Physical properties of crystals: their representation by tensors and matrices, Oxford University Press," 1985.

[71] F. Mouhat and F. Coudert, "Necessary and sufficient elastic stability conditions in various crystal systems."

[72] W. Voigt, *Lehrbuch der kristallphysik (mit ausschluss der kristalloptik)*. Springer-Verlag, 2014.

[73] A. Reuss, "Berechnung der fließgrenze von mischkristallen auf grund der plastizitätsbedingung für einkristalle." *ZAMM-Journal of Applied Mathematics and Mechanics/Zeitschrift für Angewandte Mathematik und Mechanik*, vol. 9, no. 1, pp. 49–58, 1929.

[74] R. Hill, "Proc. phys. soc., london, sect. a," 1952.

[75] A. Tahir, R. Janisch, and A. Hartmaier, "Hydrogen embrittlement of a carbon segregated $\sigma 5$ (310)[001] symmetrical tilt grain boundary in α-Fe," *Materials Science and Engineering: A*, vol. 612, pp. 462–467, 2014.

[76] M. Yamaguchi, "First-principles study on the grain boundary embrittlement of metals by solute segregation: Part i. iron (Fe)-solute (B, C, P, and S) systems," *Metallurgical and Materials Transactions A*, vol. 42, no. 2, pp. 319–329, 2011.

[77] D. Zhao, O. M. Løvvik, K. Marthinsen, and Y. Li, "Segregation of Mg, Cu and their effects on the strength of Al $\sigma 5$ (210)[001] symmetrical tilt grain boundary," *Acta Materialia*, vol. 145, pp. 235–246, 2018.

[78] P. Lazar and R. Podloucky, "Cleavage fracture of a crystal: Density functional theory calculations based on a model which includes structural relaxations," *Physical Review B*, vol. 78, no. 10, p. 104114, 2008.

[79] R. Janisch, N. Ahmed, and A. Hartmaier, "Ab initio tensile tests of Al bulk crystals and grain boundaries: Universality of mechanical behavior," *Physical Review B*, vol. 81, no. 18, p. 184108, 2010.

[80] J. H. Rose, J. R. Smith, and J. Ferrante, "Universal features of bonding in metals," *Physical review B*, vol. 28, no. 4, p. 1835, 1983.

[81] I. J. Jensen, J. Friis, C. D. Marioara, and I. G. Ringdalen, "The role of grain boundary precipitates during intergranular fracture in 6XXX series Aluminium alloys," *In preparation*.

[82] E. A. Jarvis, R. L. Hayes, and E. A. Carter, "Effects of oxidation on the nanoscale mechanisms of crack formation in aluminum," *ChemPhysChem*, vol. 2, no. 1, pp. 55–59, 2001.

[83] M. Kanani, A. Hartmaier, and R. Janisch, "Interface properties in lamellar TiAl microstructures from density functional theory," *Intermetallics*, vol. 54, pp. 154–163, 2014.

[84] H. Krull and H. Yuan, "Suggestions to the cohesive traction–separation law from atomistic simulations," *Engineering Fracture Mechanics*, vol. 78, no. 3, pp. 525–533, 2011.

[85] P. Liu and R. Matsumoto, "Temperature dependence of vacancy concentration and void growth mechanism in Al with constant hydrogen concentration: A first-principles study," *Engineering Fracture Mechanics*, vol. 216, p. 106508, 2019.

[86] N. Medvedeva, M. Park, D. C. Van Aken, and J. E. Medvedeva, "First-principles study of Mn, Al and C distribution and their effect on stacking fault energies in fcc Fe," *Journal of Alloys and Compounds*, vol. 582, pp. 475–482, 2014.

[87] L. Song, X. Tian, H. Jiang, W. Yu, Z. Zhao, H. Zheng, J. Qin, and X. Lin, "Vacancies effect on the mechanical properties in b2 feal intermetallic by the first-principles study," *Philosophical Magazine*, vol. 99, no. 21, pp. 2703–2717, 2019.

[88] J. Chi, X. Zheng, S. Y. Rodriguez, Y. Li, W. Gou, V. Goruganti, K. D. D. Rathnayaka, and J. H. Ross, "Dilute magnetism and vibrational entropy in Fe_2Al_5," *Phys. Rev. B*, vol. 82, p. 174419, Nov 2010.

[89] J. Chi, "A nuclear magnetic resonance probe of Fe-Al and Al20V2Eu intermetallics," Ph.D. dissertation, 2009.

[90] M. Friák, M. Golian, D. Holec, N. Koutná, and M. Šob, "An ab initio study of magnetism in disordered fe-al alloys with thermal antiphase boundaries," *Nanomaterials*, vol. 10, no. 1, p. 44, 2020.

[91] C. Fang, A. Dinsdale, Z. Que, and Z. Fan, "Intrinsic defects in and electronic properties of θ-Al13Fe4: an ab initio DFT study," *Journal of Physics: Materials*, vol. 2, no. 1, p. 015004, 2019.

[92] Z. Tian, J. Yan, W. Xiao, and W. Geng, "Effect of lateral contraction and magnetism on the energy release upon fracture in metals: First-principles computational tensile tests," *Physical Review B*, vol. 79, no. 14, p. 144114, 2009.

[93] A. Hotař, M. Palm, P. Kratochvíl, V. Vodičková, and S. Daniš, "High-temperature oxidation behaviour of Zr alloyed Fe_3Al-type iron aluminide," *Corrosion Science*, vol. 63, pp. 71–81, 2012.

[94] B. L. Silva, A. Garcia, and J. E. Spinelli, "The effects of microstructure and intermetallic phases of directionally solidified Al-Fe alloys on microhardness," *Materials Letters*, vol. 89, pp. 291–295, 2012.

[95] R. Shull, H. Okamoto, and P. Beck, "Transition from ferromagnetism to mictomagnetism in Fe-Al alloys," *Solid State Communications*, vol. 20, no. 9, pp. 863–868, 1976.

[96] G. Huffman and R. Fisher, "Mössbauer studies of ordered and cold-worked Fe-Al alloys containing 30 to 50 at.% Aluminum," *Journal of Applied Physics*, vol. 38, no. 2, pp. 735–742, 1967.

[97] E. Lee and B.-J. Lee, "Modified embedded-atom method interatomic potential for the Fe-Al system," *Journal of Physics: Condensed Matter*, vol. 22, no. 17, p. 175702, 2010.

[98] M. Mendelev, D. Srolovitz, G. Ackland, and S. Han, "Effect of Fe segregation on the migration of a non-symmetric $\sigma 5$ tilt grain boundary in Al," *Journal of Materials Research*, vol. 20, no. 1, pp. 208–218, 2005.

[99] B.-J. Lee and M. Baskes, "Second nearest-neighbor modified embedded-atom-method potential," *Physical Review B*, vol. 62, no. 13, p. 8564, 2000.

[100] B.-J. Lee, M. Baskes, H. Kim, and Y. K. Cho, "Second nearest-neighbor modified embedded atom method potentials for bcc transition metals," *Physical Review B*, vol. 64, no. 18, p. 184102, 2001.

[101] B.-J. Lee, J.-H. Shim, and M. Baskes, "Semiempirical atomic potentials for the fcc metals Cu, Ag, Au, Ni, Pd, Pt, Al, and Pb based on first and second nearest-neighbor modified embedded atom method," *Physical Review B*, vol. 68, no. 14, p. 144112, 2003.

[102] E. Asadi, M. A. Zaeem, S. Nouranian, and M. I. Baskes, "Two-phase solid-liquid coexistence of Ni, Cu, and Al by molecular dynamics simulations using the modified embedded-atom method," *Acta Materialia*, vol. 86, pp. 169–181, 2015.

[103] ——, "Quantitative modeling of the equilibration of two-phase solid-liquid Fe by atomistic simulations on diffusive time scales," *Physical Review B*, vol. 91, no. 2, p. 024105, 2015.

[104] H. Fang, P. M. Gullett, A. Slepoy, M. F. Horstemeyer, M. I. Baskes, G. J. Wagner, and M. Li, "Numerical tools for atomistic simulations." Sandia National Laboratories, Tech. Rep., 2004.

[105] Y. Ouyang, X. Tong, C. Li, H. Chen, X. Tao, T. Hickel, and Y. Du, "Thermodynamic and physical properties of FeAl and Fe_3Al: an atomistic study by EAM simulation," *Physica B: Condensed Matter*, vol. 407, no. 23, pp. 4530–4536, 2012.

[106] G. Simmons, H. Wang *et al.*, "Single crystal elastic constants and calculated aggregate properties," 1971.

[107] L. Sun, Y. Gao, B. Xiao, Y. Li, and G. Wang, "Anisotropic elastic and thermal properties of titanium borides by first-principles calculations," *Journal of Alloys and Compounds*, vol. 579, pp. 457–467, 2013.

[108] J. Haines, J. Leger, and G. Bocquillon, "Synthesis and design of superhard materials," *Annual Review of Materials Research*, vol. 31, no. 1, pp. 1–23, 2001.

[109] W. H. Wang, "Correlations between elastic moduli and properties in bulk metallic glasses," *Journal of Applied Physics*, vol. 99, no. 9, p. 093506, 2006.

[110] H.-Y. Chung, M. B. Weinberger, J.-M. Yang, S. H. Tolbert, and R. B. Kaner, "Correlation between hardness and elastic moduli of the ultraincompressible transition metal diborides RuB_2, OsB_2, and ReB_2," *Applied Physics Letters*, vol. 92, no. 26, p. 261904, 2008.

[111] J. Schroers and W. L. Johnson, "Ductile bulk metallic glass," *Physical Review Letters*, vol. 93, no. 25, p. 255506, 2004.

[112] K. Gschneidner Jr, A. Russell, A. Pecharsky, J. Morris, Z. Zhang, T. Lograsso, D. Hsu, C. C. Lo, Y. Ye, A. Slager *et al.*, "A family of ductile intermetallic compounds," *Nature Materials*, vol. 2, no. 9, p. 587, 2003.

[113] S. Pugh, "XCII. Relations between the elastic moduli and the plastic properties of polycrystalline pure metals," *The London, Edinburgh, and Dublin Philosophical Magazine and Journal of Science*, vol. 45, no. 367, pp. 823–843, 1954.

[114] L. Tricarico, R. Spina, D. Sorgente, and M. Brandizzi, "Effects of heat treatments on mechanical properties of Fe/Al explosion-welded structural transition joints," *Materials & Design*, vol. 30, no. 7, pp. 2693–2700, 2009.

[115] H. Titrian, U. Aydin, M. Friák, D. Ma, D. Raabe, and J. Neugebauer, "Self-consistent scale-bridging approach to compute the elasticity of multi-phase polycrystalline materials," in *MRS Proc*, vol. 1524, 2013.

[116] M. Friák, W. A. Counts, D. Ma, B. Sander, D. Holec, D. Raabe, and J. Neugebauer, "Theory-guided materials design of multi-phase Ti-Nb alloys with bone-matching elastic properties," *Materials*, vol. 5, no. 10, pp. 1853–1872, 2012.

[117] L.-F. Zhu, M. Friák, L. Lymperakis, H. Titrian, U. Aydin, A. M. Janus, H.-O. Fabritius, A. Ziegler, S. Nikolov, P. Hemzalová *et al.*, "Ab initio study of single-crystalline and polycrystalline elastic properties of Mg-substituted calcite crystals," *Journal of the Mechanical Behavior of Biomedical Materials*, vol. 20, pp. 296–304, 2013.

[118] S. Bozzi, A. Helbert-Etter, T. Baudin, B. Criqui, and J. Kerbiguet, "Intermetallic compounds in Al 6016/IF-steel friction stir spot welds," *Materials Science and Engineering: A*, vol. 527, no. 16-17, pp. 4505–4509, 2010.

[119] G. Kresse and J. Furthmüller, "Vienna ab-initio simulation package (VASP)," *Vienna: Vienna University*, 2001.

[120] R. Yang, S. Tanaka, and M. Kohyama*, "First-principles study on the tensile strength and fracture of the Al-terminated stoichiometric α-Al_2O_3 (0001)/Cu (111) interface," *Philosophical Magazine*, vol. 85, no. 25, pp. 2961–2976, 2005.

[121] T. Ogura, Y. Saito, T. Nishida, H. Nishida, T. Yoshida, N. Omichi, M. Fujimoto, and A. Hirose, "Partitioning evaluation of mechanical properties and the interfacial microstructure in a friction stir welded aluminum alloy/stainless steel lap joint," *Scripta Materialia*, vol. 66, no. 8, pp. 531–534, 2012.

[122] H. Das, S. Basak, G. Das, and T. K. Pal, "Influence of energy induced from processing parameters on the mechanical properties of friction stir welded lap joint of aluminum to coated steel sheet," *The International Journal of Advanced Manufacturing Technology*, pp. 1–9, 2013.

[123] L. Liu, L. Xiao, J. Feng, L. Li, S. Esmaeili, and Y. Zhou, "Bonding of immiscible Mg and Fe via a nanoscale Fe_2Al_5 transition layer," *Scripta Materialia*, vol. 65, no. 11, pp. 982–985, 2011.

[124] U. Burkhardt, Y. Grin, M. Ellner, and K. Peters, "Structure refinement of the iron–aluminium phase with the approximate composition Fe_2Al_5," *Acta Crystallographica Section B*, vol. 50, no. 3, pp. 313–316, 1994.

[125] M. Z. Khalid, J. Friis, P. H. Ninive, K. Marthinsen, and A. Strandlie, "DFT calculations based insight into bonding character and strength of Fe_2Al_5 and Fe_4Al_{13} intermetallics at Al-Fe joints," *Procedia Manufacturing*, vol. 15C, pp. 1407–1415, 2018.

[126] P. Peyre, G. Sierra, F. Deschaux-Beaume, D. Stuart, and G. Fras, "Generation of aluminium-steel joints with laser-induced reactive wetting," *Materials Science and Engineering: A*, vol. 444, no. 1-2, pp. 327–338, 2007.

[127] Y.-J. Wang and C.-Y. Wang, "Influence of the alloying element re on the ideal tensile and shear strength of γ-Ni_3Al," *Scripta Materialia*, vol. 61, no. 2, pp. 197–200, 2009.

[128] L. Xu, L. Wang, Y.-C. Chen, J. D. Robson, and P. B. Prangnell, "Effect of interfacial reaction on the mechanical performance of steel to aluminum dissimilar ultrasonic spot welds," *Metallurgical and Materials Transactions A*, vol. 47, no. 1, pp. 334–346, 2016.

[129] S. Kobayashi and T. Yakou, "Control of intermetallic compound layers at interface between steel and aluminum by diffusion-treatment," *Materials Science and Engineering: A*, vol. 338, no. 1, pp. 44–53, 2002.

Part II

Included Papers

Paper I

Khalid MZ, Friis J, Ninive PH, Marthinsen K and Strandlie A,"DFT calculations based insight into bonding character and strength of Fe_2Al_5 and Fe_4Al_{13} intermetallics at Al-Fe joints," *Procedia Manufacturing 15,* vol. 15, pp. 1407-1415, 2018.

Paper I

DFT calculations based insight into bonding character and strength of Fe_2Al_5 and Fe_4Al_{13} intermetallics at Al-Fe joints

Khalid M. Z., Friis J., Ninive P. H., Marthinsen K. Strandlie A.

Available online at www.sciencedirect.com

ScienceDirect

Procedia Manufacturing 15 (2018) 1407–1415

Procedia MANUFACTURING

www.elsevier.com/locate/procedia

17th International Conference on Metal Forming, Metal Forming 2018, 16-19 September 2018, Toyohashi, Japan

DFT calculations based insight into bonding character and strength of Fe_2Al_5 and Fe_4Al_{13} intermetallics at Al-Fe joints

Muhammad Zeeshan Khalid[a,c,] *, Jesper Friis[b], Per Harald Ninive[a], Knut Marthinsen[c], Are Strandlie[a]

[a] *Department of Manufacturing and Civil Engineering, Norwegian University of Science and Technology, Gjøvik, 2815, Norway*
[b]*SINTEF Materials and Chemistry, Trondheim, Norway*
cDepartment of Material Science and Engineering, Norwegian University of Science and Technology (NTNU), Trondheim, Norway

Abstract

The joining of aluminum and steel has been considered as the efficient combination to develop lightweight and environmental friendly structures. However, due to the significant differences in mechanical and physical properties of aluminum and steel, the joining of these two metals is challenging, where typically several intermetallic phases are formed at the interface. Origin of intermetallic phases at the Al-Fe interface is inevitable due to the low intermixing of Al and Fe. Thus in order to achieve reliable joining, it is necessary to have basic understanding about these intermetallic phases. This paper aims to describe mechanical and bonding properties of the two most commonly observed phases, Fe_4Al_{13} and Fe_2Al_5. The formation energy, elastic properties and nature of bonding of Fe_4Al_{13} and Fe_2Al_5 have been calculated. The results show that Fe_2Al_5 is thermodynamically more stable than Fe_4Al_{13}, and it seems to be less brittle than Fe_4Al_{13}. Electron localization plots of these compounds show a combination of covalent and metallic bonding, where Fe_4Al_{13} shows a stronger tendency of covalent character than Fe_2Al_5

Peer-review under responsibility of the scientific committee of the 17th International Conference on Metal Forming.

Keywords: Fe-Al intermetallic; Mechanical properties; Al-Fe welding; First-principles calculation

* Corresponding author. Tel.: +47-96707507.
E-mail address: muhammad.z.khalid@ntnu.no

2351-9789 © 2018 The Authors. Published by Elsevier B.V.
Peer-review under responsibility of the scientific committee of the 17th International Conference on Metal Forming.
10.1016/j.promfg.2018.07.341

1. Introduction

Multi-material vehicle structures are considered to be one of the most promising solutions for automotive weight reduction and is receiving more and more attention with the growing concerns on energy saving and environmental preservations [1]. A typical and efficient combination is aluminum and high-strength steel (590-1470 MPa). Due to the significant difference in physical and mechanical properties of these two materials, it is very difficult to achieve reliable joints between these two materials through traditional fusion welding techniques [2, 3].

Various methods and techniques have been studied to achieve optimal properties, but it has been found inevitable to avoid the development of intermetallic phases at the interface due to the limited diffusion of aluminum and steel. It is thermodynamically possible to produce a range of intermetallic phases in the Al-Fe system [4, 5], However, Fe_2Al_5 and Fe_4Al_{13} layers are the most commonly observed ones at Al-Fe joints by different welding methodologies [6, 7].

Cold metal transfer is one of the welding techniques that has been employed to weld aluminum and steel. In this welding technique, aluminum is placed on the surface of a steel plate, and filler wire is melted along the edges of the plate creating a lap joint [8]. Cao et al. [9, 10] showed that the molten filler metal and the aluminum develop a fusion joint, and the filler and the aluminum plate forms a brazed joint with the steel plate, where intermetallic phases are formed. Using the transmission electron microscopy (TEM), these intermetallic phases can be distinguished. Based on our cold metal transfer sample's TEM images in our SFI research Centre, we found Fe_2Al_5 and Fe_4Al_{13} intermetallic phases at the interface. Between these two phases, Fe_2Al_5 has been reported to be the most dominant one [11]. This is thought to be partly due to the favored crystallographic habit orientation with ferrite ([110] Fe_2Al_5//[111]Fe, (001) Fe_2Al_5//(0-11)Fe, (1-10) Fe_2Al_5//(2-1-1)Fe) [11].

In order to understand the basic nature and improvement of welding methodologies, a complete understanding of these intermetallic phases is vital to help experimentalists to anticipate their properties by looking into their basic mechanical properties.

Despite extensive experimental and numerical studies of layer growth, formation and stability of these intermetallic phases, there is still need for a more fundamental understanding of their basic bonding and mechanical properties. This paper presents a density functional theory based study, mainly making a comparative analysis of the properties of Fe_2Al_5 and Fe_4Al_{13} in terms of thermodynamic stability, strength and mechanical behavior. Calculations performed in this study termed to act as universal for all welding methodologies in which these two intermetallic phases are reported.

1.1. Computation

All calculations in this paper were implemented using first-principle calculations based on density functional theory (DFT), which were performed by the Vienna ab-initio Simulation Package code [12]. The exchange correlation energy was evaluated with the Projected augmented-wave method of the Perdew-Burke-Ernzerhof approach [13]. For the Al and Fe atoms, the electronic states $3s^2\ 3p^1$ and $3d^6\ 4s^2$, respectively, are treated as valence states. Automatic k-points were generated by using the method proposed by Monkhorst-Pack to characterize energy integration in the first irreducible Brillouin zone [14]. In our calculations, a maximum energy cutoff value of 500 eV was used for the plane wave expansion in reciprocal space. During the calculations of elastic constants, we employed a plane-wave energy of 500 eV and a 9×10×15 k-point mesh for the orthorhombic crystal and 3×5×4 for the monoclinic crystal. During the optimization process, the total energy changes were finally converged to 1×10^{-6} eV/atom.

1.2. Construction of crystal structures

Fe_2Al_5 and Fe_4Al_{13} has orthorhombic and monoclinic crystal class, respectively. Crystal structure unit cells were constructed by considering the directory of Springer library [15, 16]. Crystallographic data for the two crystal structures is shown in Table 1. There are many crystalline materials, which are non-stoichiometric in composition. In these cases, refinement of site occupancy is required. Crystallographic data for Fe_2Al_5 show that it has this behavior, so site occupancy refinement was performed by calculating the ground state energy. Al in Fe_2Al_5 have a site occupancy value of 0.167, so in order to find a stable configuration of this structure, Fe_2Al_5 crystal structures with different Al site occupancies were relaxed in order to determine the minimum energy value. The structure with lowest total energy value was used for further calculations in this paper. Al and Fe in Fe_4Al_{13} on the other hand has a site occupancy of 1,

however, the unit cell contains more than 100 atoms. In order to reduce the computational cost, the Fe_4Al_{13} crystal structure was cut along vectors a=[1,0,0], b=[0.5,0.5, 0] and c=[0,0,1]. This reduces the computational cost without breaking the symmetry. The final Fe_2Al_5 and Fe_4Al_{13} optimized structures used for these calculations are shown in Fig. 1.

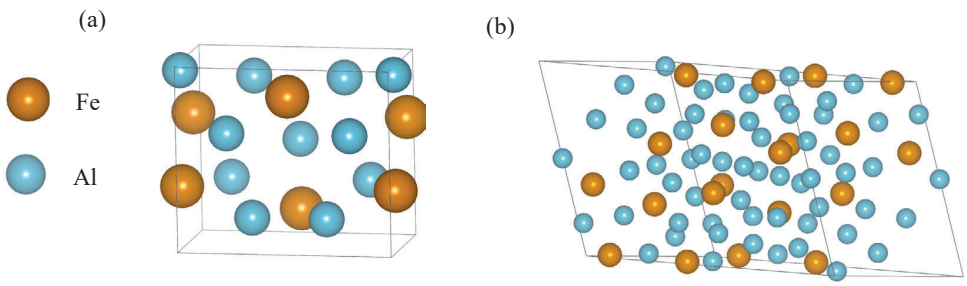

Fig. 1. (a) Fe_2Al_5 crystal structure; (b) Fe_4Al_{13} crystal structure.

Table 1. Calculated cohesive and formation energies of Fe_2Al_5 and Fe_4Al_{13}.

Species	Space group	a (Å)	b (Å)	c (Å)	Angle	E_b (ev/atom)	ΔH_R (ev/atom)
Fe_2Al_5	Cmcm	7.418	6.428	4.103	α= β= 90	-7.364	-7.352
		7.466[a]	6.181[a]	4.808[a]	ɣ= 90	-13.728[a]	-8.385[a]
		7.622[b]	6.323[b]	4.178[b]			
Fe_4Al_{13}	C2/m	15.125	4.012	11.839	α=90, β= 107	-5.819	-4.562
		15.352[a]	8.010[a]	12.398[a]	ɣ= 90	-9.063[a]	-3.923[a]
		15.069[b]	7.864[b]	12.083[b]			

[a] [17]
[b] [18]

2. Results and discussions

2.1. Chemical stability

The material hardness can be evaluated by calculating the bonding energy. Bonding energy/cohesive energy is defined as the energy required to break the bulk structure into its constituent's elements. Materials having a high bonding energy are generally harder than those having a low bonding energy. Similarly, the chemical stability of a compound can be predicted by calculation of formation energy. The bonding energy (cohesive energy), $E_b(Fe_xAl_y)$, and the formation energy, $\Delta H_r(Fe_xAl_y)$, are in the present work calculated according to the following two equations:

$$\Delta H_r(Fe_xAl_y) = \frac{E_{tot}((Fe_xAl_y) - xE_b(Fe) - yE_b(Al)}{x+y}, \quad (1)$$

$$E_b(Fe_xAl_y) = \frac{E_{tot}((Fe_xAl_y) - xE_{iso}(Fe) - yE_{iso}(Al)}{x+y}, \quad (2)$$

where $E_{tot}(Fe_xAl_y)$ is the total energy for the Fe_xAl_y phase and E_{iso} is the total energy of a single Fe or Al atom. $E_b(Fe)/E_b(Al)$ is the binding energy (per atom) of either pure Fe or Al.

After optimization of the crystal structures, we got the lattice parameters and bonding energy of Fe_2Al_5 and Fe_4Al_{13}, as listed in Table 1. The crystal parameters showed good agreement with literature in general. Some of the differences may be due the different setups or methodologies. In our work, we also made some structural simplifications and modifications to the crystal structures, which may also have some impact. However, it can be noted from Table 1 that the bonding energy of Fe_4Al_{13} is greater than that of Fe_2Al_5. All bonding energies listed in Table 1 are negative, which shows that the arrangements of atoms are energetically favorable compared to the atoms being separated from one another by large distances [19]. The crystal structure naturally chosen will be the one with the largest negative value. In our case, Fe_2Al_5 has the larger cohesive energy. However, there is not a significant difference between Fe_2Al_5 and Fe_4Al_{13}, which is why these phases have quite close melting temperatures (i.e., 1171 C for Fe_2Al_5 and 1157 C for Fe_4Al_{13}) according to the Al-Fe phase diagram.

Thermodynamic stability of the two compounds can be predicted by calculating their formation energy using Eq. (2). A lower negative formation energy implies a more stable crystal structure. The formation energy we calculated for these compounds are -7.352 and -4.562 for Fe_2Al_5 and Fe_4Al_{13} respectively. From these results, it can be concluded that the Fe_2Al_5 phase is thermodynamically more stable than Fe_4Al_{13}.

2.2. Calculation of elastic constants for the prediction of mechanical properties

The elastic constants provides useful information about the dynamic and mechanical behavior of crystals and about how the crystal responds to forces acting on it. As single crystal samples are not easily available, it is in general difficult to measure experimentally the individual elastic constants C_{ij}. Instead, we can determine the shear (G) and bulk modulus (B) [19]. However, prior to calculations of these quantities we need to calculate elastic constants based on generalized Hooke's law by the stress-strain method. The related elastic constants are identified from these stress relations given in the following equation [20]:

$$\begin{pmatrix} \sigma_1 \\ \sigma_2 \\ \sigma_3 \\ \tau_4 \\ \tau_5 \\ \tau_6 \end{pmatrix} = \begin{pmatrix} C_{11} & C_{12} & C_{13} & C_{14} & C_{15} & C_{16} \\ C_{21} & C_{22} & C_{23} & C_{24} & C_{25} & C_{26} \\ C_{31} & C_{32} & C_{33} & C_{34} & C_{35} & C_{36} \\ C_{41} & C_{42} & C_{43} & C_{44} & C_{45} & C_{46} \\ C_{51} & C_{52} & C_{53} & C_{54} & C_{55} & C_{56} \\ C_{61} & C_{62} & C_{63} & C_{64} & C_{65} & C_{66} \end{pmatrix} \begin{pmatrix} \xi_1 \\ \xi_2 \\ \xi_3 \\ \gamma_4 \\ \gamma_5 \\ \gamma_6 \end{pmatrix} , \tag{3}$$

where σ_i is normal stress, τ_i is the shear stress, C_{ij} are the elastic constants, γ_i is the shear strain and ε_i is the corresponding normal strain. Total number of independent elastic constant is determined by the symmetry of the crystal. Since in this study Fe_2Al_5 has orthorhombic symmetry while Fe_4Al_{13} belongs to monoclinic crystal system, the total numbers of independent elastic constant for these crystals are 9 and 13, respectively.

The calculated elastic constants for both the orthorhombic and monoclinic phases are given Table 2. Furthermore, stability of these crystal structures can be calculated by using the formulas given in Eqs (4) and (5) for orthorhombic and monoclinic crystal structures [18].

For orthorhombic structure (Fe_2Al_5),

$$C_{11}>0,\ C_{22}>0,\ C_{11}+C_{22}+C_{33}+2(C_{12}+C_{13}+C_{23}) > 0,$$
$$C_{33}>0,\ C_{44}>0,\ C_{55}>0,\ C_{66}>0,\ C_{11}+C_{22}-2C_{12}>0 \quad . \tag{4}$$

For monoclinic system (Fe_4Al_{13}),

$$C_{11}>0,\ C_{22}>0,\ C_{33}>0,\ C_{44}>0,\ C_{55}>0,\ C_{66}>0,$$
$$C_{11}+C_{22}+C_{33}+2(C_{12}+C_{13}+C_{23})>0,\ (C_{11}C_{55}-(C_{12})^2)>0,$$
$$C_{22}+C_{33}-2C_{23}>0,\ (C_{44}C^{66}-(C_{46})^2)>0,$$
$$C_{22}(C_{33}C_{55}-(C_{35})^2)+2C_{23}C_{25}C_{35}-(C_{23})^2C_{55}-(C_{25})^2C_{33}>0,$$
$$2[C_{15}C_{25}(C_{33}C_{12}-C_{13}C_{23})+C_{15}C_{35}(C_{22}C_{13}-C_{12}C_{23})+C_{25}C_{35}(C_{11}C_{23}-C_{12}C_{13})]$$
$$-[(C_{15})^2(C_{11}C_{22}-(C_{12})^2+C_{55}(C_{11}C_{22}C_{33}-C_{11}(C_{23})^2-C_{22}(C_{13})^2-C_{33}(C_{12})^2+C_{12}C_{13}C_{23})]>0 \quad . \tag{5}$$

From Table 2, we find that all elastic constants of both Fe_2Al_5 and Fe_4Al_{13} satisfy these above criteria. This means that both are mechanically stable.

In order to obtain a better understanding of the mechanical properties of these compounds, the bulk modulus (B), shear modulus (G), Young's modulus (E) and Poisson ratio (σ) are calculated according to Voight-Reuss-Hill approach [22], and compared with previous ab-initio calculations [17], embedded atom method [18] and modified embedded atom method [21] results. All results are shown in Table 3.

Table 2. Calculated elastic constants of Fe_2Al_5 and Fe_4Al_{13}.

crystal	C_{11}	C_{22}	C_{33}	C_{44}	C_{55}	C_{66}	C_{12}	C_{13}	C_{15}	C_{23}	C_{25}	C_{35}	C_{46}
Fe_2Al_5	213.49	237.49	269.17	88.25	78.25	99.66	77.13	89.43		45.71			
	249.4[a]	300.4[a]	256.3[a]	109.6[a]	65.4[a]	109.6[a]	68.4[a]	45.6[a]		60.0[a]			
	126[b]	97.4[b]	174.1[b]	81.6[b]	68.6[b]	52.3[b]	136.2[b]	71.8[b]		49.2[b]			
Fe_4Al_{13}	216.3	195.8	219.03	77.09	63.93	76.07	59.70	41.52	-2.75	19.28	-3.61	-3.36	-0.067
	127.4[a]	260.2[a]	259.6[a]	76.1[a]	97.7[a]	84.5[a]	71.8[a]	67.6[a]	3.9[b]	49.5[a]	9.1[b]	-7.1[b]	-14.9[b]
		148.2[b]	182.0[b]	-17.2[b]	25.1[b]	34.2[b]	80.3[b]	72.8[b]		72.9[b]			

[a] [17], [b] [18]

Table 3. Calculated bulk modulus (B), shear modulus (G), Young's modulus (E) and Poisson's ratio (σ) of Fe_2Al_5 and Fe_4Al_{13}.

Compound	Method	B_{HILL}(GPA)	G_{HILL}(GPA)	E_{HILL}(GPA)	B_{HILL}/G_{HILL}	σ	Anisotropy measure(=0 if isotropic) E_{max}/E_{min}
Fe_2Al_5	This work	126.92	85.84	210.16	1.47	0.224	1.39
	EAM [18]	101.3	16.5	47.0		0.423	
	DFT [19]	127.5	97.0	232.1	1.31	0.196	
Fe_4Al_{13}	This work	96.41	76.65	181.79	1.25	0.185	1.29
	EAM [18]	105.6	23.8	145.7		0.376	
	DFT. [19]	127.4	89.7	218.0	1.41	0.215	
	MEAM [21]	103.5					

The ccompressibility of a material under a hydrostatic pressure can be defined by the bulk modulus. As shown in Table 3, Fe_2Al_5 has a higher value of the bulk modulus as compared to that of Fe_4Al_{13}, indicating that Fe_2Al_5 is more resistant to compression than Fe_4Al_{13}. Hardness and stiffness of a material can be predicted by the shear modulus (G) and Young's modulus (E), respectively. According to our calculations, Fe_2Al_5 has a significantly higher value of Young's modulus (210.16 GPa) than Fe_4Al_{13} (181.79 GPa). Haines et al. [23] proved that hardness of a material is closely related to its Young's modulus and shear modulus. It is generally recognized that the larger the relevant modulus is, the higher hardness the material has. Thus, the larger modulus of Fe_2Al_5 (G=85.84 GPa, E= 210.16 GPa) clearly indicates that this phase is harder than Fe_4Al_{13} (G=76.65 GPa, E= 181.79 GPa). To further shed light on the brittle and ductile properties of these compounds, the ratio of bulk modulus to shear modulus (B/G), which is an empirical criterion of the extent of fracture range of the material [23], is considered. The material behaves as ductile when the B/G ratio > 1.75, otherwise it will show brittle characteristics [17]. In our work, it can easily be implied that both materials have a B/G value lower than 1.75, indicating that both possess brittle behavior. Still, Fe_4Al_{13} is more brittle than Fe_2Al_5. For Poisson's ratio, it is generally accepted that materials with a low Poisson's ratio are brittle [18, 24]. Thus, since Fe_4Al_{13} has a lower value of Poisson's ratio (0.185) than Fe_2Al_5 (0.224), it is clearly indicated that Fe_4Al_{13} is more brittle than Fe_2Al_5.

During welding of the Al/Fe system, micro-cracks sometimes are induced in the intermetallic compound layer, which may strongly affect the strength and stability of the joints. The presence of micro-cracks are often associated with the mechanical anisotropy. Therefore, study of mechanical anisotropy is very important for these compounds. A universal anisotropic index A^U for crystals proposed by S.I. Ranganathan and M.O. Starzewski [25] is given as;

$$A^U = \frac{5G_{Voigt}}{G_{Reuss}} + \frac{B_{Voigt}}{B_{Reuss}} - 6 \geq 0 \quad , \tag{6}$$

where A^U=0 for isotropic materials. The deviations of A^U from zero defines the extent of single-crystal anisotropy and includes both shear and bulk contributions [26]. A larger value of the anisotropic index A^U indicates greater anisotropic mechanical properties. According to our calculations, both materials have non-zero values (Table 3), which indicate anisotropic properties; with Fe_2Al_5 having a stronger anisotropy than Fe_4Al_{13}. For highly anisotropic materials, it is instructive to report the directional elastic moduli (Fig 2).

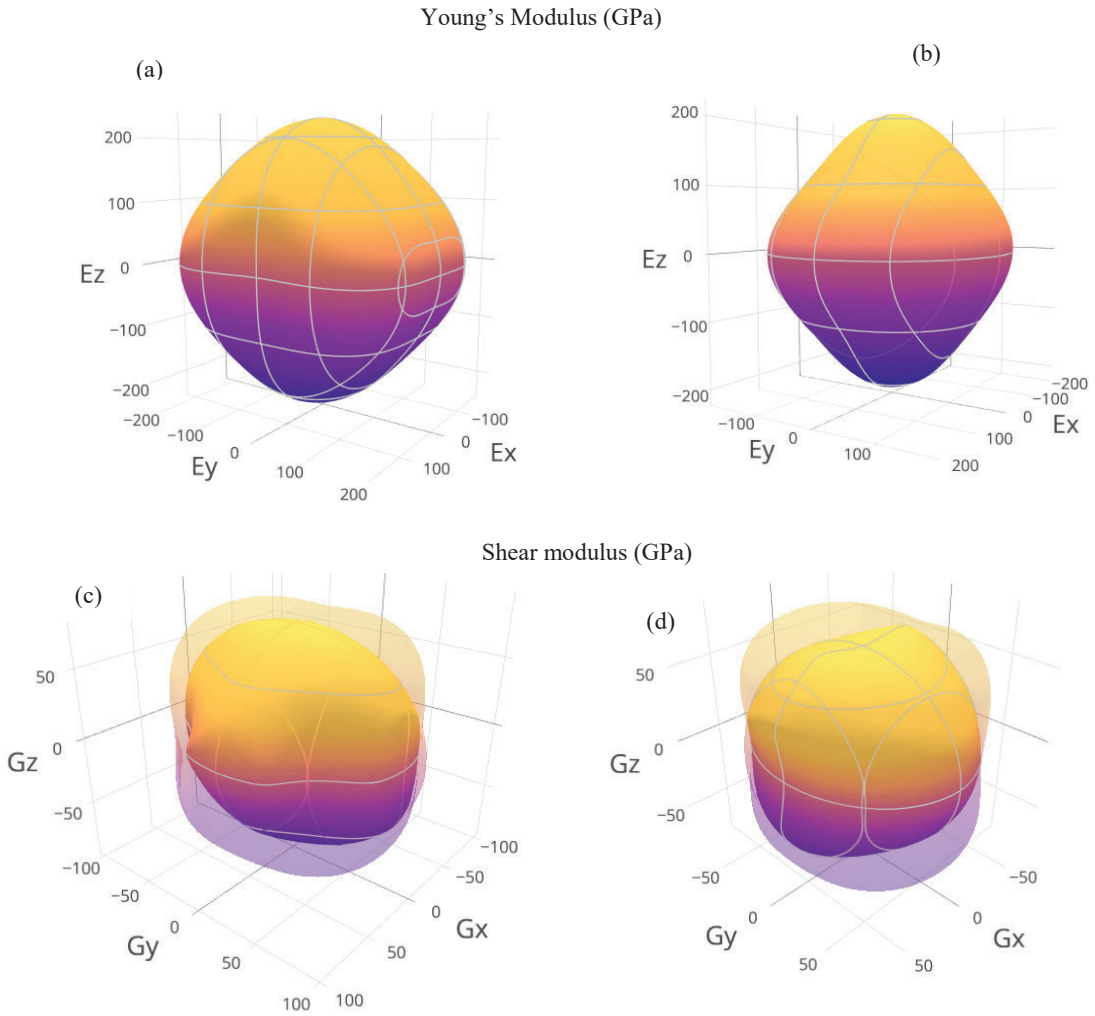

Fig. 2. Contour plots of direction dependency of Young's modulus (a) and shear modulus (c) for Fe_2Al_5 and (b) and (d) for Fe_4Al_{13}. In figure (c) and (d) clouds over solid color bar shows the surface with maximum shear modulus value, and the surface corresponding to minimum shear modulus is shown in solid color bars. Visualization generated with ELATE [27, 28].

3D surfaces of Young's modulus (E), and shear modulus are shown in Fig. 2. For an isotropic system, the graph would show a perfect spherical shape. Deviations from the perfect spherical shape indicate anisotropic behavior of the compound. Obviously, both compounds show anisotropic behavior as can be seen from the above illustrations. However, Fe_2Al_5 show a stronger anisotropic behavior of shear modulus (Fig. 2(c)) as compared to Fe_4Al_{13} (Fig. 2(d)). Overall, Fe_2Al_5 show stronger anisotropic properties, which is why during a welding process, Fe_2Al_5 is more prone to induce micro-cracks as compared to Fe_4Al_{13}. However, the intermetallic layer thickness may also have an influence, but was not taken into account in the current study.

2.3. Origin of mechanical anisotropy

To gain insight into the origin of these mechanical properties and bonding characteristics, we have also calculated the electron localization function. Fig 3(a) shows the contours of the electron localization function for Fe_2Al_5 and Fig 3(b) for Fe_4Al_{13}. The electron localization function (ELF) ranges between 0 (no/zero localization) and 1 (perfect localization) while a value of 0.5 corresponds to a perfect free electron gas (metallic bonding) [29]. As observed in Figs. 3(a) and (b), Fe atoms show a metallic bonding character with Al atoms both for the Fe_2Al_5 and Fe_4Al_{13} compound. However, bonding between Al-Fe atom pairs is anisotropic, showing metallic or covalent nature depending on position. Electron clouds between Fe-Fe was only observed at ELF = 0.5 values and disappeared at 0.65 as shown in Fig 3 (c), which indicate metallic bonding between Fe-Fe atoms. The maximum value of ELF was achieved between Al-Al atoms indicating covalent bonding between these atoms. From this analysis, it can be concluded that the bonding characteristics in both compounds are directional dependent, which is probably the reason for the anisotropic mechanical properties. As there is a higher amount of Fe in Fe_2Al_5, and Fe-Fe bonds are metallic, this could also explain the more ductile nature of Fe_2Al_5 as compared to Fe_4Al_{13}.

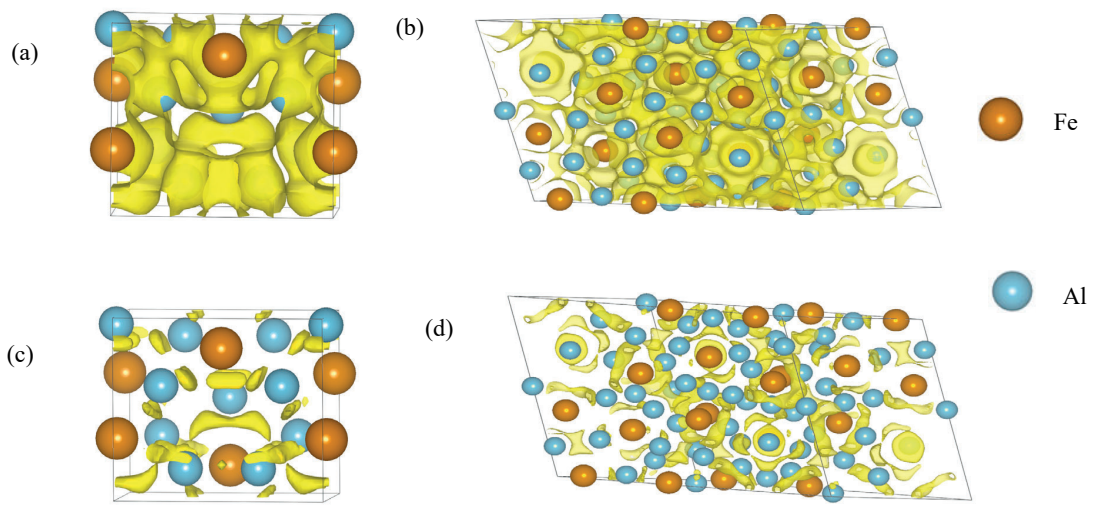

Fig. 3. Electron localization function Plot of Fe_2Al_5(001) (a), (c) and Fe_4Al_{13}(0-11) (b), (d), (a) ELF= 0.5 (b) ELF = 0.5, (c) ELF = 0.65, (f) ELF = 0.65.

3. Conclusion and Future work

In this work, mechanical and bonding properties of the Fe_2Al_5 and Fe_4Al_{13} intermetallic compounds were investigated by first-principles calculations. Both compounds are shown to be mechanically and dynamically stable by analysis of elastic constants and formation enthalpies. Both compounds were found to be brittle and showed mechanical anisotropic behavior. The calculations of mechanical properties showed that Fe_4Al_{13} is more brittle than

Fe_2Al_5. However, Fe_2Al_5 showed more directional dependent mechanical properties. In addition, analysis of their electron localization plots showed covalent character between Al-Al, and metallic bonding between Fe-Fe, while Al-Fe showed both metallic and covalent character depending on position/orientation in the structure.

Calculations of interfacial strength and mechanical properties of intermetallics compounds such as FeAl, $FeAl_2$, Fe_3Al and different AlFeSi phases still need to be studied to establish the role of these compounds in joining of aluminum and steel.

Acknowledgements

The work reported in this paper was based on activities within the centre for research-based innovation SFI Manufacturing in Norway and is partially funded by the Research Council of Norway under contract number 237900. UNINETT Sigma2 AS (The Norwegian Metacenter for High Performance Computing) provided computational resources through Project NN9466K and NN9158K.

References

[1] T. Sakiyama, G. Murayama, Y. Naito, K. Saita, Y.M.H. Oikawa, T. Nose, Dissimilar metal joining technologies for steel sheet and aluminum alloy sheet in auto body, Nippon Steel & Sumitomo Metal Corp, Tokyo, Nippon Steel Technical Report, 103 (2013) 91–98.
[2] T. Ogura, Y. Saito, T. Nishida, H. Nishida, T. Yoshida, N. Omichi, M. Fujimoto, A. Hirose, Partitioning evaluation of mechanical properties and the interfacial microstructure in a friction stir welded aluminum alloy/stainless steel lap joint, Scripta Materialia, 66-8 (2012) 531–534.
[3] H. Das, S. Basak, G. Das, T.K. Pal, Influence of energy induced from processing parameters on the mechanical properties of friction stir welded lap joint of aluminum to coated steel sheet, The International Journal of Advanced Manufacturing Technology, (2013) 1–9.
[4] Y. Chen, A. Gholinia, P. Prangnell, Interface structure and bonding in abrasion circle friction stir spot welding: a novel approach for rapid welding aluminium alloy to steel automotive sheet, Materials Chemistry and Physics, 134-1 (2012) 459–463.
[5] W.J. Cheng, C.J. Wang, Study of microstructure and phase evolution of hot-dipped aluminide mild steel during high-temperature diffusion using electron backscatter diffraction, Applied Surface Science, 257-10 (2011) 4663–4668.
[6] M. Eggersmann, H. Mehrer, Diffusion in intermetallic phases of the Fe-Al system, Philosophical Magazine A, 80-5 (2000) 1219–1244.
[7] N. Tang, Y. Li, S. Kurosu, Y. Koizumi, H. Matsumoto, A. Chiba, Interfacial reactions of solid co and solid Fe with liquid Al, Corrosion Science, 60 (2012) 32–37.
[8] S. Niu, S. Chen, H. Dong, D. Zhao, X. Zhang, X. Guo, G. Wang, Microstructure and properties of lap joint between aluminum alloy and galvanized steel by CMT, Journal of Materials Engineering and Performance, 25-5 (2016) 1839–1847.
[9] R. Cao, J.H. Sun, J.H. Chen, P.C. Wang, Cold metal transfer joining of aluminum AA6061-T6-to-galvanized boron steel, Journal of Manufacturing Science and Engineering, 136 (2014) 051015–051015-10.
[10] R. Cao, G. Yu, J.H. Chen, P.C. Wang, Cold metal transfer joining aluminum alloys-to-galvanized mild steel, Journal of materials processing technology, 213 (2013) 1753–1763.
[11] K.K. Wang, L. Chang, D. Gan, H.P. Wang, Heteroepitaxial growth of Fe_2Al_5 inhibition layer in hot-dip galvanizing of an interstitial-free steel, Thin Solid Films, 518-8 (2010) 1935–1942.
[12] G. Kresse, J. Furthmuller, Vienna ab-initio simulation package (vasp), Vienna, Vienna University.
[13] P.E. Blochl, Projector augmented-wave method, Physical review B, 50-24 (1994) 17953.
[14] H.J. Monkhorst, J.D. Pack, Special points for brillouin-zone integrations, Physical review B, 13-12 (1976) 5188.
[15] Fe_2al_5 (feal2.8) crystal structure, Datasheet from "pauling file multinaries edition – 2012" in SpringerMaterials, copyright 2016 Springer-Verlag Berlin Heidelberg & Material Phases Data System (MPDS), Switzerland & National Institute for Materials Science (NIMS), Japan. URL http://materials.springer.com/isp/crystallographic/docs/sd_1201135
[16] $FeAl_3$ (Fe_4Al_{13}) crystal structure, Datasheet from "pauling file multinaries edition–2012", SpringerMaterials, copyright 2016 SpringerVerlag Berlin Heidelberg & Material Phases Data System (MPDS), Switzerland & National Institute for Materials Science (NIMS), Japan. URL http://materials.springer.com/isp/crystallographic/docs/sd_0261719
[17] Y. Liu, X. Chong, Y. Jiang, R. Zhou, J. Feng, Mechanical properties and electronic structures of Fe-Al intermetallic, Physica B: Condensed Matter, 506 (2017) 1–11.
[18] C.H. Zhang, S. Huang, J. Shen, N.X. Chen, Structural and mechanical properties of Fe–Al compounds: An atomistic study by EAM simulation, Intermetallics, 52 (2014) 86–91.
[19] P. Ravindran, L. Fast, P.A. Korzhavyi, B. Johansson, J. Wills, O. Eriksson, Density functional theory for calculation of elastic properties of orthorhombic crystals: application to $TiSi_2$, Journal of Applied Physics, 84-9 (1998) 4891–4904.
[20] J. Feng, B. Xiao, J. Chen, Y. Du, J. Yu, R. Zhou, Stability, thermal and mechanical properties of PtxAly compounds, Materials & Design, 32-6 (2011) 3231–3239.
[21] B. Jelinek, S. Groh, M.F. Horstemeyer, J. Houze, S.G. Kim, G.J. Wagner, A. Moitra, M.I. Baskes, Modified embedded atom method potential for Al, Si, Mg, Cu, and Fe alloys, Physical Review B, 24 (2012) 245–102.

[22] G. Simmons, H. Wang, Single crystal elastic constants and calculated aggregate properties, Cambridge, MA: MIT Press, (1971).
[23] S.F. Pugh, XCII. relations between the elastic moduli and the plastic properties of polycrystalline pure metals, The London, Edinburgh and Dublin Philosophical Magazine and Journal of Science, 367 (1954) 823–843.
[24] J. Schroers, L.W. Johnson, Ductile bulk metallic glass, Physical Review Letters, 25 (2004) 255506.
[25] S.I. Ranganathan, M.O. Starzewski, Universal elastic anisotropy index, Physical Review Letters, 5 (2008) 055504.
[26] Z.G. Mei, S.L. Shang, Y. Wang, Z.K. Liu, First-principles study of structural and elastic properties of monoclinic and orthorhombic BiMnO3, Journal of Physics: Condensed Matter, 29 (2010) 295404.
[27] Elate, Elastic tensor analysis, http://progs.coudert.name/elate, accessed: 2018-04-16.
[28] R. Gaillac, P. Pullumbi, F.X. Coudert, ELATE: an open-source online application for analysis and visualization of elastic tensors, Journal of Physics: Condensed Matter, 27 (2016) 275201.
[29] B. Wang, D.Y. Wang, Y.X. Wang, A new hard phase of ReB_4 predicted from first principles, Journal of Alloys and Compounds, 573 (2013) 20–26.

Paper II

Khalid M. Z., Friis J., Ninive P. H., Marthinsen K., Strandlie A. (2019). Modified embedded atom method potential for Fe-Al intermetallic mechanical strength: A comparative analysis of atomistic simulations, Pre-print

Paper II

Modified embedded atom method potential for Fe-Al intermetallic mechanical strength: A comparative analysis of atomistic simulations

Khalid M. Z., Friis J., Ninive P. H., Marthinsen K., Ringdalen I.G., Strandlie A.

Abstract

The structural and mechanical properties of Fe-Al compounds (FeAl, Fe_2Al, Fe_3Al, $FeAl_2$, $FeAl_3$, Fe_2Al_5) have been studied using modified embedded atom method (MEAM) potentials. The equilibrium lattice constants, formation enthalpies, and elastic properties have been investigated and compared with other studies. The calculated lattice constants show good agreement with the embedded atom method (EAM) and density functional theory (DFT) calculations and with experiments. All Fe-Al compounds are mechanically stable according to the elastic constants restrictions. The calculated bulk modulus of the compounds does not show a linear relation with Fe concentration, which is most probably caused by the mechanical anisotropy of Fe-Al compounds. However, a comparison of the Fe-Al mechanical properties of MEAM, DFT and EAM-based approaches and experiments show non-consistent differences, which reflects uncertainties with several of these methods, due to assumptions and simplifications imposed during calculations. In gen-

eral, DFT calculations are closer to experimental observations than semi-empirical potentials. Comprehensive comparisons are made based on theoretical and experimental methodologies.

Keywords

Fe-Al intermetallics; elastic properties; atomistic simulations

1 Introduction

Fe-Al compounds have been gaining a lot of attention due to their increased industrial interest owing to the light-weight, corrosion resistance and high-temperature resistance behavior [1–3]. FeAl compounds including Fe_3Al, FeAl, Fe_2Al_5, $FeAl_2$ and $FeAl_3$ have been the main focus of research in many different industrial areas, for example, high-temperature structural materials, composite materials, protective coatings for materials and functional materials. Fe-Al materials have been considered very promising because they are considered as potential candidates for replacing steel [4, 5].

Many researchers have performed atomistic simulations to predict the mechanical strength of Fe-Al compounds [6–10]. Zhang et al. [6] studied the structural and mechanical properties of these compounds by EAM simulations. Liu et al. [10] studied the mechanical and electronic properties of Fe-Al compounds by an ab-initio method. Jelinek et al. [9] developed the MEAM and calculated the lattice constants, formation enthalpy and bulk modulus of $FeAl_3$, $FeAl_2$, FeAl, and Fe_3Al compounds. Liu et al. [11] studied the FeAl compound and calculated the elastic properties from first-principles calculations. Niu et al. [12] performed first-principles simulations for the prediction of mechanical properties and electronic structure of the Fe_3Al compound.

All these simulations were performed on a single unit cell of Fe-Al compounds without considering any crystal defects. However, results from simulations have shown contrasting trends about the mechanical properties of these compounds. The differences can be caused by the following reasons, (i) the mechanical properties change at higher temperatures, (ii) the potentials used for calculations are inaccurate and require further improvements. To signify the differences between different semi-empirical potentials and first-principles studies, we have made comparisons of the mechanical properties of Fe-Al compounds with experiments. We also studied the inaccuracy of these atomistic simulations, and tried to find the best atomistic methodology for the prediction of actual trends about Fe-Al compounds.

In this paper, we have investigated the structural and mechanical properties of Fe-Al compounds (FeAl, Fe_2Al, Fe_3Al, $FeAl_3$, Fe_2Al_5) analyzed by semi-empirical

interatomic potentials, i.e. the MEAM method [9, 13]. MEAM is extensively applied for metallic systems [14–16] and it agrees reasonably well with experiments [17, 18]. The MEAM potential mono-atomic parameters fitted to Al and Fe and their binary combination developed by Jelinek et al [9] are used in this study. Other studies have already reported the structural properties of Fe-Al compounds by using the MEAM potentials. In this study, however, we are exploring the mechanical properties of Fe-Al compounds and discuss the reliability and applicability of semi-empirical potentials for extracting actual values by comparing it with density functional theory (DFT) and experiments.

2 Method of calculation

2.1 Interatomic potential

In DFT, the electron structure of a many-electron systems is solved, which is computationally very intensive. For this reason, a direct numerical solution can only be applied to smaller systems so far. To overcome this limitation, molecular dynamic (MD) simulations offer an opportunity of studying larger systems. In MD, the interaction between atoms is described by Newton's classical equation of motion, which in the simplest form for a particle of mass m_i ($i = 1, 2, ...N$) with interaction potential Φ, can be defined as [19]:

$$\vec{F_i} = m_i \frac{d^2}{dt^2}\vec{r_i} = -\nabla_i \Phi(\vec{r_i} - \vec{r}) \tag{1}$$

where $\nabla_i \Phi$ is the force field felt by the atom i, $\vec{r_i}$ is the position of atom i and $\vec{r}$ is the mass center of system. To describe the interatomic interaction, many researchers have developed empirical and semi-empirical interatomic potentials, whose parameters are mainly determined by results from density functional theory.

MD simulations frequently approximate the atomic interaction with an average interaction from neighboring atoms. One of the most common and widely used interatomic potentials is the embedded atom method (EAM) developed by Baskes [20], which considers many-body terms suitable for metallic systems.

The modified EAM (MEAM) method is a generalization of EAM that in addition includes (i) the directional bonding effect and (ii) a screening function is introduced to limit the number of interactions between the atoms. Even with the introduction of new parameters, the MEAM potentials struggle to predict experimentally consistent results for BCC metals [14, 15]. For example, MEAM has predicted that other metals are thermodynamically more stable than BCC metals, while it is experimentally well known that BCC metals are more stable [14, 15]. Moreover, surface energies of low-index surfaces of BCC metals are not consist-

ent with experiments. This failure of the MEAM potentials for BCC is assumed to be caused by the fact that only nearest-neighbor interactions are considered. To overcome this shortcoming, second-nearest neighbor interactions (2NN) have been introduced by adjusting the screening parameter [21]. The MEAM formalism is thoroughly described in literature [16, 21, 22].

2.2 MEAM parameters and simulation technique

The MEAM parameters used in this work for Al and Fe are given in Table 1. The initial values were directly taken from MEAM potentials [16, 22] without any modifications. E_c and a_0 depends on the material properties (see Table 1 caption), if the initial reference structure is known. It is either directly taken from the experiments or optimization of the structure. The other important parameter is C_{min}, which defines the extent of screening of an atom (k) with the neighboring atoms (i and j). The elements are the same for pure elements (i-j-k=A-A-A or B-B-B), however for Fe-Al compounds, one of the screening atoms could be different (i-j-k=A-B-A, B-A-B, A-A-B, B-B-A) [23]. For this reason a different value of C_{min} has to be assigned. To improve the generalized stacking fault energy curves, the value of C_{min} was reduced to 0.8 from 2 for Al [9]. C_{max} has been given a fixed value of 2.8 for Fe and 1.9 for Al. C_{max} determines the position of an atom (k) that begins screening with a second neighboring atom (i or j). The values of C_{min} and C_{max} thereby define the range of screening to nearest-neighbor interactions. The density scaling factor ρ_0 also affects the calculations. For pure elements, the factor has been removed, but for alloys and compounds with different types of elements, this factor may have a great effect on the calculations.

The parameters listed in Table 1 are determined by fitting the experiments or by density functional theory based calculated physical properties for Fe-Al binary compounds. The MEAM parameters for Fe-Al compounds were initialized to match the DFT-calculated heat of formation, bulk modulus, equilibrium volume and elastic moduli to the hypothetical NaCl reference structure [9]. NaCl was chosen as a reference structure due to its direct relevance with MEAM and simplicity. Based on a trial and error method, parameters were varied until the properties calculated showed good agreement with DFT and experimental values. Those values were then further considered for Fe-Al compounds and shown in Table 1. The most important parameter which affects the physical properties of the compounds is the density scaling factor ρ_0 for the element pair. For Fe-Al binary compounds, it is selected to be 1 [9]. The remaining parameters β^n and t^n ((n=1,2,3)) are adjustable parameters, and values are determined by the fitting of physical properties with DFT.

After the selection of suitable values for MEAM parameters, the simulations were

Table 1: Set of MEAM parameters for fcc Al and bcc Fe. E_c is the cohesive energy, a_0 is the quilibrium lattice constant, A is the scaling factor for embedding energy. α is exponential decay factor for the universal energy, β^0 ^{3} are the exponential decay factors for the atomic energies, t^0 ^{3} are the weighting factors for the atomic densities, C_{max} and C_{min} are the screening parameters, and ρ_0 is the density scaling factor relevant for the element pairs.

element	E_c(eV)	a_0(Å)	A	α	β^0	β^1	β^2	β^3	t^0	t^1	t^2	t^3	C_{min}	C_{max}	ρ_0
Al	3.35	4.04	1.07	4.64	2.04	3.0	6.0	1.5	1.0	4.5	-2.3	8.01	0.8	2.8	1.0
Fe	4.28	2.851	0.55	5.027	3.5	2.0	1.0	1.0	1.0	-1.6	12.5	-1.4	0.68	1.9	1.0

run by using an Atomistix Toolkit (ATK) forcefield [24, 25]. Before the calculations of elastic constants, the geometry of the material was optimized by relaxing the atoms until the maximum forces and stresses were less than 0.001 eV/atom and 0.01 GPa, respectively. To obtain the equilibrium structure of Fe-Al intermetallics, the quasi-Newton optimizer "Limited-memory Broyden-Fletcher-Goldfarb-Shanno (LBFGS)" [26] was adopted.

2.3 Calculations of elastic constants

The elastic constants are related to the various components of stress and strain by:

$$\sigma_{ijl} = C_{ijk}\epsilon_{kl} \tag{2}$$

where σ_{ijl}, C_{ijk} and ϵ_{kl} are the stress, elastic components and strain tensor, respectively. After the calculations of elastic constants, various mechanical properties of Fe-Al compounds such as bulk modulus (B), Young's modulus (Y), shear modulus (G) and Poisson's ratio (ν) can be obtained by using the Voigt-Reuss-Hill (VRH) approximation [27–29]. The bulk modulus (B) and shear modulus were obtained by Eq. (3) and (4), respectively, and the VRH approximation was used to calculate the average of the lower and upper bounds of the elastic modulus. Young's modulus (Y) and Poisson's ratio (ν) were calculated from the bulk modulus and shear modulus by using Eq. (5)-(6) (for cubic systems).

$$B = [2(C_{11} + C_{12} + 2C_{13}) + C_{33}]/9 \tag{3}$$

$$G = (7C_{11} - 5C_{12} + 2C_{33} + 12C_{44} - 4C_{13})/30 \tag{4}$$

$$Y = 9BG/(3B + G) \tag{5}$$

$$\nu = (3B - 2G)/2(3B + G) \tag{6}$$

The mechanical stability of these compounds has also been studied in this paper. The elastic stability criteria in various crystal structure systems can be found in the Appendix.

3 Results and Discussions

3.1 Structural properties

MEAM potentials were used to calculate equilibrium lattice constants, equilibrium volume, and formation enthalpy as shown in Table 2. Calculated structural values are compared with available experimental results, interatomic potentials, and DFT studies. As can be seen, the calculated lattice constants of FeAl from MEAM potentials are consistent with experimental studies [30, 31]. The results are as good as DFT and somewhat inferior to EAM. The calculated formation enthalpy for FeAl is -1.49 eV/atom, which is consistent with EAM [6] studies (-1.42 eV/atom). However, DFT results from [10] have shown better agreement with experiments as compared to EAM/MEAM potentials. We applied this potential for other Fe-Al IMCs as well. For another cubic structure, Fe_3Al (Fm3m), our calculated lattice constants are larger than those reported in other theoretical studies [6, 10], but shows better agreement with experimental values [30, 31]. For the monoclinic structure $FeAl_3$, the differences between lattice constants are found to be largest along the a_0 unit direction with a 7.68 % difference to experimental values [30]. For the orthorhombic Fe_2Al_5 and trigonal $FeAl_2$ structures, the difference between lattice constants was found to be 2.77-6.20 % and 15.31 % along the **a**, **a** and **a** lattice directions, respectively. These differences to experimental values indicate that the MEAM potentials are inaccurate and do not describe well low symmetry structures. EAM potentials [6] have also shown this tendency. The reason for this inaccuracy is attributed to the background electron density. In MEAM and EAM potentials, the background electron density is used to describe the many-body interactions and is assumed to be a homogeneous electron gas [6]. This may well describe high-symmetry structures such as a cubic structure, but it is not obvious that it describes the directional effects in low symmetry structures equally well.

We calculated the formation enthalpies by studying the energies of the optimized structures for the Fe-Al compounds as given in Table 2. All calculated values were compared with other theoretical [6, 10, 32] and experimental [33–35] results and plotted in the graph shown in Fig.1. It is generally accepted that the stability of a compound can be predicted by the values of formation enthalpies. Based on our calculations, all Fe-Al compounds have negative formation enthalpies, showing that they are thermodynamically stable. For cubic structures (FeAl, Fe_3Al), the

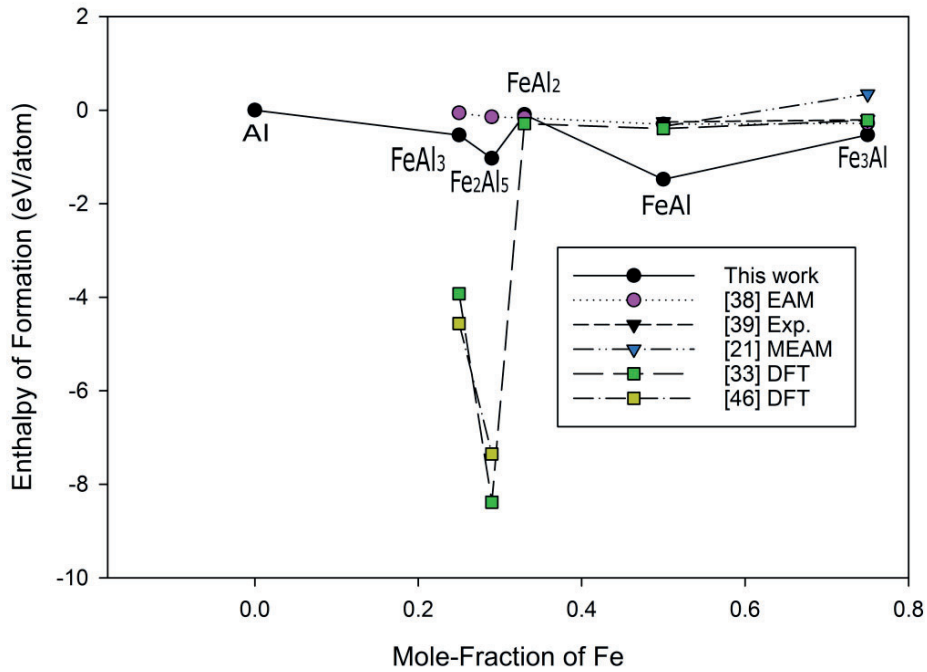

Figure 1: Comparison of calculated formation enthalpies of Fe-Al compounds with other studies.

formation enthalpies were found to be higher for all theoretical studies as compared to experiments, but for low-symmetry structures ($FeAl_3$, Fe_2Al_5 and $FeAl_2$) the opposite is found. Based on MEAM calculations, FeAl has the highest negative value (-1.48 eV/atom)) among the Fe-Al compounds, hence it is deemed to be thermodynamically more stable than any other Fe-Al compound studied in this work. This conclusion is consistent with EAM [6] studies, but contradicts with DFT results [10], which predicts Fe_2Al_5 to be the most stable compound.

3.2 Elastic constants and mechanical properties

In this section, we are investigating the elastic constants and mechanical strength of the different Fe-Al compounds. Table 3 lists the calculated elastic constants compared with EAM [6], DFT [10], long-range analytical embedded atom method (LAEAM) [38], and experimental studies [35, 39]. It is well known that different symmetries impose different constraints on the elastic constants. These constraints are defined from A.2-A.4 (see Appendix) for the cubic, orthorhombic, monoclinic

Table 2: The calculated lattice parameters from the present calculations compared with references and measured values. H_f is the formation enthalpy and V_0 is the equilibrium volume per atom calculated in Å^3.

Phase	Space group	Species	a_0(Å)	b_0(Å)	c_0(Å)	V_0 (Å^3)	H$_f$(eV/atom)
FeAl	Pm3m	This work	2.953	-	-	12.87	-1.48
		EAM/MEAM	2.893 [6]	-	-	12.88 [9]	-1.42 [32]
		DFT [10]	2.851 [10]	-	-	12.07 [36]	-0.390 [10]
		Exp.	2.909 [30]	-	-	12.23 [37]	-0.423 [33]
		Exp.	-			-	-0.28 [34]
Fe$_3$Al	Fm3m	This work	5.769			12.00	-0.53
		EAM/MEAM	5.764 [6]			12.01 [9]	-0.279 [6]
		DFT	5.586 [10]			12.01 [36]	-0.217 [10]
		Exp.	5.789 [31]			12.07 [37]	-0.202 [35]
		Exp.	5.792 [30]			-	-0.321 [33]
FeAl$_3$	C2/m	This work	16.680	7.860	12.220	15.73	-0.532
		EAM/MEAM	15.069 [6]	7.864	12.083	15.03 [9]	-0.059 [6]
		DFT	15.352 [10]	8.010	12.398	13.91 [9]	-3.923 [10]
		DFT	15.125 [7]	4.012 [7]	11.839 [7]	-	-4.562 [7]
		Exp.	15.49 [30]	8.08	12.48	-	n.a
FeAl$_2$	P1	This work	4.054	6.687	8.802	15.77	-0.093
		EAM/MEAM	4.6212 [6]	6.372	8.629	14.71 [9]	-0.160 [6], -0.076 [9]
		DFT	4.793 [10]	6.351	8.658	12.78 [9]	-0.286 [10]
		Exp.	4.787 [30]	4.787	6.461	-	n.a
Fe$_2$Al$_5$	Cmcm	This work	7.462	6.717	4.464	15.96	-1.0303
		EAM	7.622 [6]	6.323	4.178		-0.146 [6]
		DFT	7.466 [10]	6.181	4.808		-8.385 [10] -7.352 [7]
		Exp.	7.675 [30]	6.403	4.203		n.a

and trigonal systems. Elastic constants calculated for FeAl (cubic), Fe$_3$Al (cubic), FeAl$_3$ (monoclinic), FeAl$_2$ (trigonal) and Fe$_2$Al$_5$ comply with the respective restriction criteria, which implies that these compounds are mechanically stable.

As given in Table 3, good agreement was found with experimental studies for cubic structures (FeAl, Fe$_3$Al). FeAl elastic constants were found to be slightly overestimated compared with experimental studies [35, 39] but underestimated when compared with DFT results in [40]. The same conclusion can be drawn for other crystal structures. Overall DFT [7, 10] elastic constants show higher values when compared with EAM [6], LAEAM [38] and MEAM [8, 9].

To better understand the mechanical strength of Fe-Al compounds, mechanical properties such as bulk modulus, shear modulus, Young's modulus, and Poisson's ratio were calculated from the elastic constants. Table 4 lists the calculated values for the relevant Fe-Al compounds. Our calculated bulk modulus is similar to the experimental bulk modulus [39] for the FeAl compound and closer to the experimental result than any of the other theoretical studies [6, 8, 9, 38]. To make comparisons and interpret the results, bulk moduli of the Fe-Al compounds with different amounts of Fe are plotted in Fig. 2. The differences to other studies and experimental values reported in this study may be attributed to the following

reasons: (i) defects in the crystal structures were ignored, and (ii) the effects of anisotropy on the elastic constants are not considered. As shown in Fig. 2, with increasing contents of Fe, the bulk modulus decreases from $FeAl_3$ to $FeAl_2$, but for FeAl (138.3 GPa) and Fe_3Al (123.99 GPa), it again shows an increase. Since bulk Fe has a higher bulk modulus than Al, the bulk modulus is expected to increase with an increase in the Fe concentrations. However, the anisotropy of the crystal could affect this trend. To visualize the anisotropic properties we plotted 3D plots of directional dependencies of Young's modulus (see Fig. 3) using spherical coordinates. Readers are referred to the following references [40, 41] for details on the theoretical construction of anisotropic behavior of isotropic crystal structures. As shown in Fig. 3 the least anisotropic structure is FeAl with the highest values of Young's modulus along the $<111>$ direction, while Fe_3Al is found to be the most anisotropic structure. For this reason, FeAl shows a higher bulk modulus value despite having a lower Fe content as compared to Fe_3Al. Moreover we can clearly see that Fe_2Al_5 is more anisotropic than $FeAl_3$ and $FeAl_2$. This shows that the material's mechanical properties are largely influenced by the anisotropic nature, which is why we see different trends in the bulk modulus with varying contents of Fe (Fig. 2).

Haines et al. [42] showed that materials with higher shear and Young's modulus have a tendency of showing a higher hardness [43, 44]. Therefore FeAl, which is found to be the material with the largest moduli (G= 103.03 GPa, Y= 247.61 GPa) is a hard phase, while $FeAl_3$ with the smaller moduli (G= 37.88 GPa, Y= 99.23 GPa) is a softer phase. Poisson's ratio can provide important information about the brittle and ductile nature of the material. It is generally accepted that materials with low Poisson's ratio are brittle [45, 46]. From Table 4, we can see that FeAl has the lowest Poisson's ratio value, which indicates a brittle nature of FeAl.

To obtain further insight into the brittle and ductile nature of compounds, an empirical criterion of fracture has been proposed [47]. According to this criterion, the ratio between the bulk modulus (B) and the shear modulus (G) provides important information about the brittle and ductile nature of relevant compounds. Materials having $B/G > 1.75$ are assumed to be ductile, while materials having a ratio smaller than this are expected to exhibit brittle properties. From Table 4 we can see that FeAl, Fe_3Al and $FeAl_2$ have $B/G < 1.75$, which indicates that these materials are brittle. When comparing to different methodologies in literature, we have found a mixed trend for the properties of the Fe-Al IMCs. Based on the available data on the mechanical properties, Table 5 shows the ambiguity about certain property predictions of the Fe-Al compounds based on different theoretical and experimental methods.

The compressibility of a compound can be related to the bulk modulus of the ma-

Table 3: Elastic constants (in GPa).

Comp.	Method	C_{11}	C_{12}	C_{13}	C_{22}	C_{23}	C_{33}	C_{44}	C_{55}	C_{66}	C_{14}	C_{15}	C_{25}	C_{35}
FeAl Pm3m	This work	256.26	94.96					115.88						
	EAM [6]	179.1	132.9					116.6						
	DFT [10]	294.0	133.7					157.0						
	LAEAM [38]	224.6	146.6					113.6						
	MEAM [9]	251.4	92.2					111.7						
	Exp. [35]	207.7	121.4					126.2						
	Exp. [39]	181.1	113.7					127.1						
Fe_3Al Fm3m	This work	188.51	125.34					121.65						
	EAM [6]	187.9	133.3					138.1						
	DFT [10]	284.7	207.5					151.0						
	LEAM [38]	212.5	160.2					124.8						
	MEAM [9]	177.5	117.5					129.0						
	Exp. [39]	171.0	130.6					131.7						
$FeAl_3$ C2/m	This work	148.91	60.26	46.80	147.42	56.64	160.35	45.77	58.75	13.77		-5.12	4.25	-5.86
	EAM [6]	168.5	80.3	72.8	148.2	72.9	182.0	-17.2	25.1	34.2		3.9	9.1	-7.1
	DFT [10]	248.9	71.8	67.6	260.2	49.5	259.6	76.1	65.4	109.6				
$FeAl_2$ Pl	This work	172.34	37.29	49.79	141.92	62.64	158.71	51.87	67.43	38.09	19.22			
	EAM [6]	223.9	71.5	88.1	194.5	101.0	184.4	81.6	68.6	52.3	-12.0			
	DFT [10]	223.3	88.3	77.4	260.7	78.2	263.1	94.1	89.1	92.8				
Fe_2Al_5 Cmcm	This work	205.58	28.89	52.09	123.99	81.52	103.29	36.70	47.40	53.61				
	EAM [6]	126.0	136.2	71.8	97.4	49.2	174.1	13.8	21.6	18.2				
	DFT [10]	294.4	68.4	45.6	300.4	60.0	256.3	109.6	97.7	84.5				

terial. Materials having higher bulk modulus are more resistant to compression. We find FeAl as the most resistant to compression, with the highest bulk modulus. By comparing our calculated values with other available literature, we find some discrepancies with respect to this property. This work is in good agreement with other studies performed using MEAM potentials [9], but differs from EAM [6], DFT [10] and experimental studies [39]. In terms of the brittle and ductile nature of these compounds, an EAM study found [6] that all compounds are ductile, which does not fit well with DFT [10] and our work. Furthermore, many experimental studies have reported the brittle nature of these Fe-Al compounds, particularly Fe_2Al_5 and $FeAl_3$ [48]. Both MEAM (this work) and EAM [6] are unable to predict precisely the brittle nature of Fe_2Al_5 and $FeAl_3$ compounds, while DFT studies [7, 10] have shown good agreement with experimental observations. In terms of hardness of these compounds, this work predicted FeAl as the hardest phase, which agrees well with DFT but contradicts with EAM and experiments. A good agreement is also found with DFT in terms of mechanical anisotropy predictions of these compounds. This work shows agreement with experiments in predicting $FeAl_3$ as a soft phase. Hardness reported in experimental studies is dependent on the temperature range, welding or experimental methodologies. Since the present simulations were performed without considering temperature, deviations from experiments are inevitable.

Table 4: The calculated bulk modulus (B), shear modulus (G), Young's modulus (Y) and Poison's ration (ν) of Fe-Al compounds.

Comp.	Method	B (GPa)	G (GPa)	Y (GPa)	B/G	ν
FeAl Pm3m	This work	138.3	103.03	247.61	1.34	0.20
	EAM [6]	148.2	55.9	148.9	2.65	0.33
	MEAM [8]	124.5	-	-	-	-
	MEAM [9]	145.3	-	-	-	-
	DFT [10]	187.1	119.8	296.2	1.56	0.236
	Exp. [39]	136.1	-	-	-	-
Fe_3Al Fm3m	This work	123.99	72.572	182.17	1.71	0.255
	EAM [6]	151.5	66.2	173.4	2.29	0.309
	MEAM [8]	148.9	-	-	-	-
	MEAM [9]	137.5	-	-	-	-
	DFT [10]	233.2	87.9	234.0	2.65	0.33
	Exp. [39]	144.1	-	-	-	-
$FeAl_3$ C2/m	This work	87.047	37.88	99.23	2.30	0.31
	EAM [6]	105.6	23.80	65.9	4.44	0.376
	MEAM [9]	103.5	-	-	-	-
	DFT [10]	127.3	89.7	232.1	1.42	0.215
	DFT [7]	94.41	76.65	218.0	1.23	0.185
$FeAl_2$ P1	This work	83.836	49.51	124.09	1.69	0.25
	EAM [6]	124.90	49.8	47.0	2.51	0.32
	MEAM [9]	90.4	-	-	-	-
	DFT [10]	136.5	87.8	216.9	1.55	0.235
Fe_2Al_5 Cmcm	This work	85.53	39.502	102.37	2.17	0.295
	EAM [6]	101.3	16.5	47.0	6.14	0.423
	DFT [10]	127.5	97.0	232.1	1.31	0.196
	DFT [7]	126.92	85.84	210.16	1.48	0.224

4 Discussion

We have performed MEAM simulations and made comparisons of interatomic potentials with experiments and DFT. It is hard to find a perfect match with experiments due to the simplifications and generalizations imposed during computational calculations, but general trends can still be extracted as indications of actual properties. All these single-crystal simulations are performed without considering crystal defects, hence the values calculated from these calculations are over-estimated as compared to the experimental values. Still, these calculations provide vital insights into the mechanical behavior of ideal compounds. In this study, we have made comparisons of the Fe-Al compounds with other simulation techniques and methods. To be consistent in our comparisons, we only considered single-crystal calculations without any crystal defects.

Table 5 shows comparisons of the materials mechanical properties based on the calculated elastic constants. As discussed in Section 3, there are contrasting differences between the mechanical properties of these compounds. When compared

Table 5: Difference in mechanical properties of Fe-Al compounds reported in literature. All properties are described in descending order.

Property	This work	EAM [6]	MEAM [9]	DFT [10]	Exp. [39, 48, 52]
Compressibility	FeAl>Fe_3Al>$FeAl_3$>Fe_2Al_5>$FeAl_2$	Fe_3Al>FeAl>$FeAl_2$>$FeAl_3$>Fe_2Al_5	FeAl>Fe_3Al>$FeAl_3$>$FeAl_2$	Fe_3Al>FeAl>$FeAl_2$>Fe_2Al_5>$FeAl_3$	Fe_3Al>FeAl
Brittle to ductile	FeAl (brittle)>$FeAl_2$(brittle)>Fe_3Al (brittle)>Fe_2Al_5(ductile)>$FeAl_3$(ductile)	All compounds Ductile	Not reported	Fe_2Al_5 (brittle)>$FeAl_3$(brittle)>$FeAl_2$ (brittle)>FeAl(brittle)>Fe_3Al(ductile)	Brittle phases Fe_2Al_5 $FeAl_3$
Hardness and stiffness	FeAl>Fe_3Al>$FeAl_2$>Fe_2Al_5>$FeAl_3$	Fe_3Al>FeAl>$FeAl_2$>$FeAl_3$>Fe_2Al_5	-	FeAl>Fe_2Al_5>Fe_3Al>$FeAl_3$>$FeAl_2$	Fe_3Al>FeAl Fe_2Al_5>$FeAl_2$ $FeAl_3$ FeAl>$FeAl_3$>$FeAl_2$ >Fe_2Al_5
Mechancial anisotropy	Fe_3Al>Fe_2Al_5>$FeAl_3$>$FeAl_2$>FeAl	Not Reported	-	Fe_3Al>FeAl>Fe_2Al_5>$FeAl_2$>$FeAl_3$	

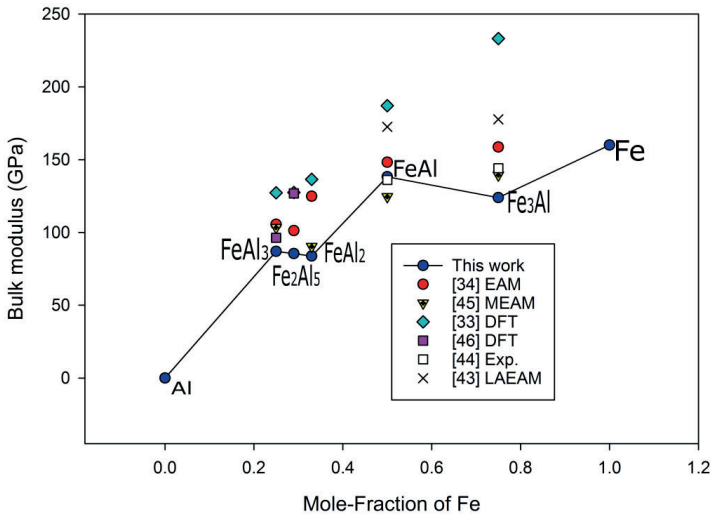

Figure 2: Comparison of calculated bulk modulus with previous studies.

to the available experimentally reported mechanical behavior of these compounds, it has been generally accepted that Fe_2Al_5 and $FeAl_3$ are brittle intermetallic compounds. However, semi-empirical potentials such as EAM and MEAM are unable to predict the brittle nature of these compounds. There are several plausible explanations for this observation: (i) these compounds are ductile at lower temperature and turn brittle at higher temperatures, (ii) crystal defects such as cracks and impurities significantly alter the mechanical properties of these compounds, and (iii) these potentials are inaccurate and not able to predict actual properties. Despite the first two assumptions, DFT calculations successfully predict the brittle nature of Fe_2Al_5 and $FeAl_3$ compounds. This shows that the interatomic potentials are not accurate enough in predicting the mechanical properties of low symmetry structures.

Furthermore, calculations of bulk modulus, shear modulus and Young's modulus from first-principles showed significantly higher values as compared to semi-empirical potentials. For the case of FeAl and Fe_3Al compounds, the bulk modulus calculated by EAM and MEAM is closer to the experimental value than the value from DFT (Table 4). It is worth mentioning that numerous experimental values also implicitly constitute contributions from crystal defects. For this reason, values calculated from single crystal calculations are over-estimated as compared to the experimental values. DFT calculations significantly over-estimate bulk modulus values compared to the experimental values, due to a too idealistic modelling

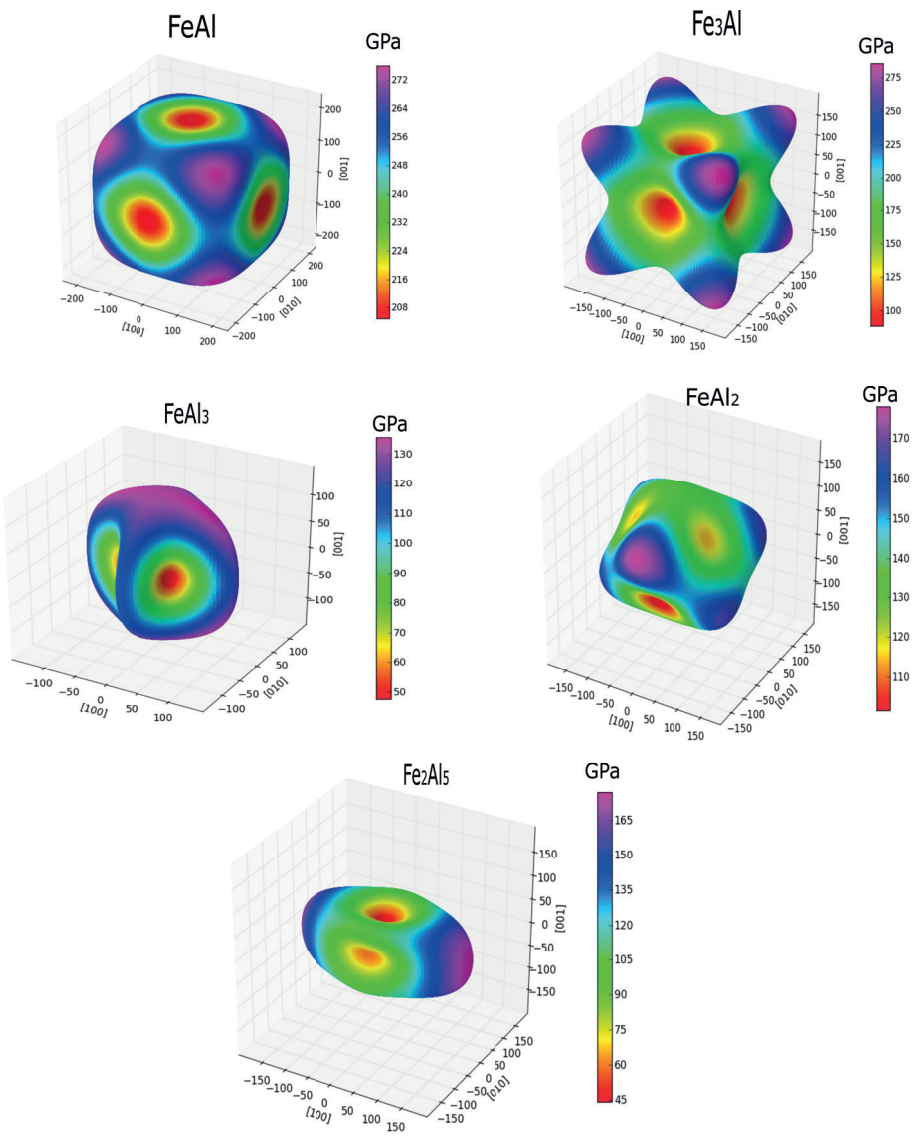

Figure 3: Directional dependence of Young's modulus of different Fe-Al compounds. The visualization is generated using the SC-EMA software package (freely available at http://scema.mpie.de) [49–51].

of FeAl and Fe_3Al compounds.

5 Conclusions

In this paper, structural and mechanical properties of different Fe-Al compounds were investigated using the MEAM. The calculated values of lattice constants and formation enthalpies show close agreement with previously reported theoretical and experimental values for different Fe-Al compounds. The calculated values of formation enthalpies of all Fe-Al compounds were found to be negative, which shows their thermodynamic stability. Calculated elastic constants were found to follow the elastic constant restrictions imposed by the symmetry of the compounds, which further confirms the mechanical stability of the considered Fe-Al compounds. Based on the bulk modulus, FeAl is found to be the hardest and $FeAl_2$ the softest phase. Comparisons of mechanical properties with other theoretical and experimental studies show uncertainties in the calculated values and material properties. However, in general, DFT is found to be in good agreement with most experimental observations.

6 Acknowledgements

The work reported in this paper was based on activities within the centre for research-based innovation SFI Manufacturing in Norway and is partially funded by the Research Council of Norway under contract number 237900.

7 Appendix

Mechancial stability criteria for Fe-Al compounds are calculated by the following relations [10, 53].

Cubic system:

$$(C_{11} - C_{12}) > 0, C_{11} > 0, C_{44} > 0, C_{11} + 2C_{12} > 0 \tag{7}$$

Orthorhombic system:

$$\begin{gathered} C_{11} + C_{12} + C_{33} + 2C_{12} + 2C_{23} > 0; C_{11} + C_{22} > 2C_{12}; \\ C_{22} + C_{33} > 2C_{23}; C_{11} + C_{33} > 2C_{13}; C_{ij} > 0 (i = 1 - 6) \end{gathered} \tag{8}$$

Monoclinic system:

$$\begin{aligned} C_{ij} > 0 (ij = 11, 22, 33, 44, 55, 66), \\ C_{11} + C_{22} + C_{33} + 2(C_{12} + C_{13} + C_{23} > 0), \\ (C_{11}C_{55} - C_{12}^2) > 0, (C_{44}C_{66} - C_{46}^2) > 0, C_{22}C_{33} - C_{23} > 0, \\ C_{22}(C_{33}C_{55} - C_{35}^2) + 2C_{23}C_{25}C_{35} - C_{23}^2C_{55} - C_{25}^2C_{33} > 0, \\ 2[C_{15}C_{25}(C_{33}C_{12} - C_{13}C_{23}) + C_{15}C_{35}(C_{22}C_{13} - C_{12}C_{23}) \\ +C_{25}C_{35}(C_{11}C_{23} - C_{12}C_{13})] - [C_{15}^2(C_{11}C_{22} - C_{12}^2) \\ +C_{55}(C_{11}C_{22}C_{33} - C_{11}C_{23}^2 - C_{22}C_{13}^2 - C_{33}C_{12}^2 + C_{12}C_{13}C_{23})] > 0 \end{aligned} \tag{9}$$

Trigonal system:

$$\begin{aligned} C_{11} - C_{12} > 0; (C_{11} + C_{12})C_{33} - 2C_{13}^2 > 0; \\ (C_{11} - C_{12})C_{44} - 2C_{14}^0 > 0 \end{aligned} \tag{10}$$

References

[1] A. Hotař, M. Palm, P. Kratochvíl, V. Vodičková, S. Daniš, High-temperature oxidation behaviour of zr alloyed fe3al-type iron aluminide, Corrosion Science 63 (2012) 71–81 (2012).

[2] B. L. Silva, A. Garcia, J. E. Spinelli, The effects of microstructure and intermetallic phases of directionally solidified Al-Fe alloys on microhardness, Materials Letters 89 (2012) 291–295 (2012).

[3] T. Sakiyama, G. Murayama, Y. Naito, K. Saita, Y. M. H. Oikawa, T. Nose, Dissimilar metal joining technologies for steel sheet and aluminum alloy sheet in auto body, Nippon Steel & Sumitomo Metal Corp., Tokyo, Nippon Steel Technical Report 103 (2013) 91–98 (2013).

[4] R. Shull, H. Okamoto, P. Beck, Transition from ferromagnetism to mictomagnetism in Fe—Al alloys, Solid State Communications 20 (9) (1976) 863–868 (1976).

[5] G. Huffman, R. Fisher, Mössbauer studies of ordered and cold-worked Fe-Al alloys containing 30 to 50 at.% aluminum, Journal of Applied Physics 38 (2) (1967) 735–742 (1967).

[6] C.-H. Zhang, S. Huang, J. Shen, N.-X. Chen, Structural and mechanical properties of Fe-Al compounds: An atomistic study by EAM simulation, Intermetallics 52 (2014) 86–91 (2014).

[7] M. Z. Khalid, J. Friis, P. H. Ninive, K. Marthinsen, A. Strandlie, DFT calculations based insight into bonding character and strength of Fe_2Al_5 and Fe_4Al_{13} intermetallics at Al-Fe joints, Procedia Manufacturing 15 (2018) 1407–1415 (2018).

[8] E. Lee, B.-J. Lee, Modified embedded-atom method interatomic potential for the $fe - al$ system, Journal of Physics: Condensed Matter 22 (17) (2010) 175702 (2010).

[9] B. Jelinek, S. Groh, M. F. Horstemeyer, J. Houze, S.-G. Kim, G. J. Wagner, A. Moitra, M. I. Baskes, Modified embedded atom method potential for Al, Si, Mg, Cu, and Fe alloys, Physical Review B 85 (24) (2012) 245102 (2012).

[10] Y. Liu, X. Chong, Y. Jiang, R. Zhou, J. Feng, Mechanical properties and electronic structures of Fe-Al intermetallic, Physica B: Condensed Matter 506 (2017) 1–11 (2017).

[11] L. Liu, X. Wu, R. Wang, W. Li, Q. Liu, First principle study on the temperature dependent elastic constants, anisotropy, generalized stacking fault energy and dislocation core of NiAl and FeAl, Computational Materials Science 103 (2015) 116–125 (2015).

[12] X.-l. Niu, L.-j. Wang, Effect of transition-metal substitution on electronic and mechanical properties of Fe_3Al: First-principles calculations, Computational Materials Science 53 (1) (2012) 128–132 (2012).

[13] M. Mendelev, D. Srolovitz, G. Ackland, S. Han, Effect of Fe segregation on the migration of a non-symmetric $\sigma 5$ tilt grain boundary in Al, Journal of materials research 20 (1) (2005) 208–218 (2005).

[14] B.-J. Lee, M. Baskes, Second nearest-neighbor modified embedded-atom-method potential, Physical Review B 62 (13) (2000) 8564 (2000).

[15] B.-J. Lee, M. Baskes, H. Kim, Y. K. Cho, Second nearest-neighbor modified embedded atom method potentials for bcc transition metals, Physical Review B 64 (18) (2001) 184102 (2001).

[16] B.-J. Lee, J.-H. Shim, M. Baskes, Semiempirical atomic potentials for the fcc metals cu, ag, au, ni, pd, pt, al, and pb based on first and second nearest-neighbor modified embedded atom method, Physical Review B 68 (14) (2003) 144112 (2003).

[17] E. Asadi, M. A. Zaeem, S. Nouranian, M. I. Baskes, Two-phase solid–liquid coexistence of ni, cu, and al by molecular dynamics simulations using the modified embedded-atom method, Acta Materialia 86 (2015) 169–181 (2015).

[18] E. Asadi, M. A. Zaeem, S. Nouranian, M. I. Baskes, Quantitative modeling of the equilibration of two-phase solid-liquid Fe by atomistic simulations on diffusive time scales, Physical Review B 91 (2) (2015) 024105 (2015).

[19] M. Steinhauser, S. Hiermaier, A review of computational methods in materials science: examples from shock-wave and polymer physics, International journal of molecular sciences 10 (12) (2009) 5135–5216 (2009).

[20] M. S. Daw, M. I. Baskes, Embedded-atom method: Derivation and application to impurities, surfaces, and other defects in metals, Physical Review B 29 (12) (1984) 6443 (1984).

[21] H. Fang, P. M. Gullett, A. Slepoy, M. F. Horstemeyer, M. I. Baskes, G. J. Wagner, M. Li, Numerical tools for atomistic simulations., Tech. rep., Sandia National Laboratories (2004).

[22] M. Baskes, Modified embedded-atom potentials for cubic materials and impurities, Physical Review B 46 (5) (1992) 2727 (1992).

[23] B.-J. Lee, A modified embedded-atom method interatomic potential for the Fe-C system, Acta materialia 54 (3) (2006) 701–711 (2006).

[24] J. Schneider, J. Hamaekers, S. T. Chill, S. Smidstrup, J. Bulin, R. Thesen, A. Blom, K. Stokbro, Atk-forcefield: a new generation molecular dynamics software package, Modelling and Simulation in Materials Science and Engineering 25 (8) (2017) 085007 (2017).

[25] Atomistix toolkit version 2017.0, synopsys quantumwise a/s, www.quantumwise.com.

[26] J. Nocedal, Updating quasi-newton matrices with limited storage, Mathematics of computation 35 (151) (1980) 773–782 (1980).

[27] W. Voigt, Lehrbuch der kristallphysik (mit ausschluss der kristalloptik), Springer-Verlag, 2014 (2014).

[28] A. Reuss, Berechnung der fließgrenze von mischkristallen auf grund der plastizitätsbedingung für einkristalle., ZAMM-Journal of Applied Mathematics and Mechanics/Zeitschrift für Angewandte Mathematik und Mechanik 9 (1) (1929) 49–58 (1929).

[29] R. Hill, Proc. phys. soc., london, sect. a (1952).

[30] H. eB, Handbook of binary alloy phase diagrams (2009).

[31] P. Villars, Pearson's handbook—desk edition: Crystallographic data for intermetallic phases; asm international: Materials park, oh, 1998, There is no corresponding record for this reference 1727–1729.

[32] C. Vailhe, D. Farkas, Shear faults and dislocation core structure simulations in B2 FeAl, Acta materialia 45 (11) (1997) 4463–4473 (1997).

[33] P. D. Desai, Thermodynamic properties of selected binary aluminum alloy systems, Journal of physical and chemical reference data 16 (1) (1987) 109–124 (1987).

[34] E. A. Brandes, G. Brook, Smithells metals reference book, Elsevier, 2013 (2013).

[35] R. Hultgren, P. D. Desai, D. T. Hawkins, M. Gleiser, K. K. Kelley, Selected values of the thermodynamic properties of binary alloys, Tech. rep., National Standard Reference Data System (1973).

[36] P. G. Gonzales-Ormeño, H. M. Petrilli, C. G. Schön, Ab-initio calculations of the formation energies of bcc-based superlattices in the Fe-Al system, Calphad 26 (4) (2002) 573–582 (2002).

[37] W. Pearson, Wb pearson: A handbook of lattice spacings and structures of metals and alloys: Pergamon press, london, new york, paris, los angeles. 1958. 1044 , 13 (8) (1958) 516 (1958).

[38] Y. Ouyang, X. Tong, C. Li, H. Chen, X. Tao, T. Hickel, Y. Du, Thermodynamic and physical properties of FeAl and Fe_3Al: an atomistic study by EAM simulation, Physica B: Condensed Matter 407 (23) (2012) 4530–4536 (2012).

[39] G. Simmons, H. Wang, et al., Single crystal elastic constants and calculated aggregate properties (1971).

[40] G. Zhang, M. Chen, Y. Shi, J. Huang, F. Yang, Analysis and modeling of the growth of intermetallic compounds in aluminum–steel joints, RSC Advances 7 (60) (2017) 37797–37805 (2017).

[41] L. Sun, Y. Gao, B. Xiao, Y. Li, G. Wang, Anisotropic elastic and thermal properties of titanium borides by first-principles calculations, Journal of Alloys and Compounds 579 (2013) 457–467 (2013).

[42] J. Haines, J. Leger, G. Bocquillon, Synthesis and design of superhard materials, Annual Review of Materials Research 31 (1) (2001) 1–23 (2001).

[43] W. H. Wang, Correlations between elastic moduli and properties in bulk metallic glasses, Journal of Applied Physics 99 (9) (2006) 093506 (2006).

[44] H.-Y. Chung, M. B. Weinberger, J.-M. Yang, S. H. Tolbert, R. B. Kaner, Correlation between hardness and elastic moduli of the ultraincompressible transition metal diborides ru b 2, os b 2, and re b 2, Applied Physics Letters 92 (26) (2008) 261904 (2008).

[45] J. Schroers, W. L. Johnson, Ductile bulk metallic glass, Physical Review Letters 93 (25) (2004) 255506 (2004).

[46] K. Gschneidner Jr, A. Russell, A. Pecharsky, J. Morris, Z. Zhang, T. Lograsso, D. Hsu, C. C. Lo, Y. Ye, A. Slager, et al., A family of ductile intermetallic compounds, Nature Materials 2 (9) (2003) 587 (2003).

[47] S. Pugh, Xcii. relations between the elastic moduli and the plastic properties of polycrystalline pure metals, The London, Edinburgh, and Dublin Philosophical Magazine and Journal of Science 45 (367) (1954) 823–843 (1954).

[48] L. Tricarico, R. Spina, D. Sorgente, M. Brandizzi, Effects of heat treatments on mechanical properties of Fe/Al explosion-welded structural transition joints, Materials & Design 30 (7) (2009) 2693–2700 (2009).

[49] H. Titrian, U. Aydin, M. Friák, D. Ma, D. Raabe, J. Neugebauer, Self-consistent scale-bridging approach to compute the elasticity of multi-phase polycrystalline materials, in: MRS Proc, Vol. 1524, 2013 (2013).

[50] M. Friák, W. A. Counts, D. Ma, B. Sander, D. Holec, D. Raabe, J. Neugebauer, Theory-guided materials design of multi-phase Ti-Nb alloys with bone-matching elastic properties, Materials 5 (10) (2012) 1853–1872 (2012).

[51] L.-F. Zhu, M. Friák, L. Lymperakis, H. Titrian, U. Aydin, A. M. Janus, H.-O. Fabritius, A. Ziegler, S. Nikolov, P. Hemzalová, et al., Ab initio study of single-crystalline and polycrystalline elastic properties of Mg-substituted calcite crystals, Journal of the mechanical behavior of biomedical materials 20 (2013) 296–304 (2013).

[52] S. Bozzi, A. Helbert-Etter, T. Baudin, B. Criqui, J. Kerbiguet, Intermetallic compounds in al 6016/if-steel friction stir spot welds, Materials Science and Engineering: A 527 (16-17) (2010) 4505–4509 (2010).

[53] F. Mouhat, F. m. c.-X. Coudert, Necessary and sufficient elastic stability conditions in various crystal systems, Phys. Rev. B 90 (2014) 224104 (Dec 2014). doi:10.1103/PhysRevB.90.224104.
URL https://link.aps.org/doi/10.1103/PhysRevB.90.224104

Paper III

Khalid M. Z., Friis J., Ninive P. H., Marthinsen K., Strandlie A. (2019). Ab-initio study of atomic structure and mechanical behaviour of Al/Fe intermetallic interfaces, Computational Materials Science, 174 (2020): 109481.

Paper III

Ab-initio study of atomic structure and mechanical behaviour of Al/Fe intermetallic interfaces

Khalid M. Z., Friis J., Ninive P. H., Marthinsen K., Strandlie A.

Abstract

First-principles virtual tensile and shear test calculations have been performed to Al(00$\bar{3}$)//α-AlFeSi(001) and Al(0$\bar{1}$4)//Fe_4Al_{13}(10$\bar{1}$) interfaces by the ab-initio pseudo potential density functional theory method. Work of separation, ultimate tensile strength and shear strength of bulk and interface structures were calculated. The Al(00$\bar{3}$)/α-AlFeSi(001) interface showed higher tensile strength than the Al(0$\bar{1}$4)//Fe_4Al_{13}(10$\bar{1}$) interface structure. Moreover, interface calculations revealed a charge depletion region in the second layer of the Fe_4Al_{13} structure, which caused lower work of separation. Furthermore, shear calculations showed stronger shear strength for the Al(0$\bar{1}$4)//Fe_4Al_{13}(10$\bar{1}$) interface than for the Al(001)//α-AlFeSi(001) interface structure.

Keyword Mechanical strength; Fe-Al joining; Intermetallics compounds interfaces; First-principles calculations; UBER

1 Introduction

Steel and aluminum alloys have been regarded as some of the most promising combinations of alloys in industrial applications due to the possibility of combining high strength and low weight. Thus joining of aluminum and steel has gained immense industrial interest in several sectors such as, aeronautics [1], automotive [2], tooling [3], power generation [4] and marine applications [5]. However, the main challenge is the ability to efficiently join this combination of metals due to the differences in the physical and chemical properties of aluminum and steel. Due to the phase diagram of the Al-Fe system with several intermetallic phases, it is also impossible to avoid the development of Fe-Al Intermetallic Compounds (IMCs) [6, 7]. Based on the temperature reached during the welding process in addition to alloy types and cooling rates, a large variety of IMCs can be created at the interface [8, 9]. Hence, it is necessary to explore the effect of these IMCs on the joint strength to achieve a better understanding and overview of different welding methodologies.

Several studies have investigated the role and formation of intermetallic layers at aluminum and steel joints [10–13]. It has been generally reported that Fe-rich IMCs such as FeAl and Fe_3Al are less brittle than Al-rich IMCs, like Fe_4Al_{13} [10]. Although it has been generally accepted that the presence of IMC layers at the interface has detrimental effects on the joint strength, some of the studies have nevertheless reported that Fe-rich IMCs may improve the mechanical properties and therefore do not have a detrimental effect on the strength of joints [11–13]. Assuming role of IMCs can have both negative and positive effects on the mechanical properties of joints.

Liu et al. [9] studied the intermetallic phases including Fe_4Al_{13}, bcc α-AlFeSi, $FeAl_m$, q_1-AlFeSi and q_2-AlFeSi. They determined the crystallographic orientation relationships between Fe_4Al_{13}, bcc α-AlFeSi, and q_n-AlFeSi (n=1,2) with Al using electron diffraction.

Chen et al. [14] reported three different types of failure modes: (i) button pullout failure, which is failure caused by shear displacement, (ii) bulk IMCs failure, and (iii) interfacial failure, i.e. failure at the interface of the aluminum and steel joint. In general, the understanding of the role of IMCs on the joint strength is ambiguous and far from complete. One of the reasons for the lack of detailed information about interfacial strength is the difficulty in characterizing the individual interfacial layers due to their small size. Over the years, many researchers have tried to identify and characterize the layers using Scanning Electron Microscopy (SEM), X-ray diffraction, and Transmission Electron Microscopy (TEM) [9, 15–17]. McDevitt et al. [15] characterized the commercially produced hot-dip

galvanized steel by using a combination of analytical TEM, SEM, and X-ray diffraction. They reported the presence of Fe_2Al_5 and Fe_4Al_{13} IMCs at the Al//steel interface and concluded that X-ray diffraction is best suited for characterizing the interfacial layers. Recently, Arbo et al. [17] reported three distinct phases: α-AlFeSi, Fe_4Al_{13} and Fe_2Al_5 at an aluminum-steel joint by TEM.

All these experiments reported that several possible phases may exist between aluminum alloys and steel, but little work has been done on quantifying the interfacial strength of these IMCs. As mentioned above, this is mainly due to the small size of the intermetallic layers. Due to experimental limitations and challenges, there has been a growing interest in computational approaches. To predict the mechanical and bonding strength, a wide range of theoretical methodologies have been applied, including semi-empirical and tight binding atomistic calculation methods, thermodynamic models, image models, and ab-initio calculations using Hartree-Fock (HF) and Density Functional Theory (DFT) [18]. Some researchers performed atomistic simulations to calculate the mechanical and structural properties of the Fe-Al bulk intermetallic compounds [19–22]. All these methods show good agreement with available experiments, in particular, the DFT approaches. But, according to our knowledge, nobody has studied the interfacial characteristics of the Al//Fe_4Al_{13} and Al//α-AlFeSi interfaces.

In this work, we have studied the interfacial structure and mechanical strength of Fe_4Al_{13} and cubic α-AlFeSi intermetallic phases with pure aluminum through atomistic simulations using DFT. We have developed the interface structures by finding the minimum misfit orientation between Al//α-AlFeSi and Al//Fe_4Al_{13} interface structures.

This paper is organized as follows. First, we discuss the methods, which comprise the computational methodology and the method to produce interface structures. In this part, we first make comparisons of bulk calculations of individual bulk phases with experiments and literature, which we further use for interface building. We then discuss the tensile and shear strength of the relevant interfaces, which comprise the most interesting feature of this work, followed by a discussion of the implications and significance of these results. We finally make a summary and present conclusions of our work.

2 Methods

2.1 Computational Method

We performed first-principles calculations based on density functional theory using the Vienna Ab-initio Simulation Package (VASP) code [23] using the Generalized

Table 1: Lattice constants of the Al, Fe_4Al_{13} and b.c.c. α-AlFeSi phases, as calculated in this work and from literature.

Compound	Space group	a (Å)	b (Å)	c (Å)	Angle
Al	Fm-3m	4.04	4.04	4.04	$\alpha = \beta = \gamma = 90°$
Fe_4Al_{13}	C2/m	15.49 15.532 [20] 15.069 [19] 15.49 [9]	8.08 8.010 [20] 7.864 [19] 8.083 [9]	12.48 12.398 [20] 12.083 [19] 12.476 [9]	$\alpha = 90°, \beta = 107.7°,$ $\gamma = 90°$
α-AlFeSi	Im3	12.69 12.56 [9] 12.589 [28]	12.69 12.56 [9] 12.589 [28]	12.69 12.56 [9] 12.589 [28]	$\alpha = \beta = \gamma = 90°$

Gradient Approximation (GGA) by Projector Augmented-Wave method (PAW) [24] employing the Perdew-Burke-Ernzerhof (PBE) approach [25]. For Al, Fe and Si atoms, the electronic states $3s^2 3p^1$, $3d^6 4s^2$ and $3s^2 3p^2$, respectively, were treated as valence electrons. For calculations, a cutoff of 550 eV for the plane wave expansion of the wave function was used to obtain accurate forces. Automatic k-points were generated by using the method by Monkhorst and Pack [26]. The electronic convergence criteria were set to 1×10^{-5} eV, and maximum forces on each ion during relaxation were 0.005 eV/Å for bulk and 0.01 eV/Å for the interface structures.

2.2 Interface structures

The atomic positions and lattice constants of α-AlFeSi and Fe_4Al_{13} were directly taken from a study published by Cooper et al. [27] and Liu et al. [9]. The DFT-relaxed bulk structures were used further for interface building. The lattice parameters used for the building of interface structures are given in Table 1. Following a face-to-face matching technique, we found the following low misfit orientation relationships:

$[010]_{Fe_4Al_{13}} \,||\, [200]_{Al}$
$[101]_{Fe_4Al_{13}} \,||\, [041]_{Al}$
$(10\bar{1})_{Fe_4Al_{13}} \,||\, (0\bar{1}4)_{Al}$
and
$[100]_{\alpha} \,||\, [310]_{Al}$
$[010]_{\alpha} \,||\, [1\bar{3}0]_{Al}$
$(001)_{\alpha} \,||\, (00\bar{3})_{Al}$

The corresponding Al$(0\bar{1}4)$//$Fe_4Al_{13}(10\bar{1})$ and Al$(00\bar{3})$//α-AlFeSi(001) bulk and overlapped interface structures are shown in Fig. 1.

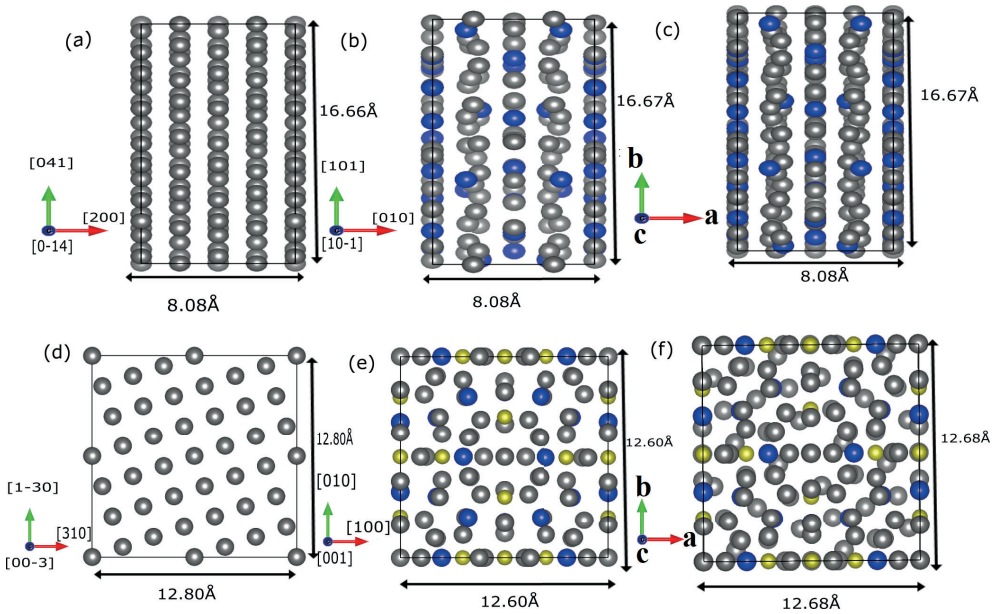

Figure 1: The atomic arrangement of Al (a,d), Fe_4Al_{13} (b) and b.c.c. α-AlFeSi (e). Overlapping structures of Al and Fe_4Al_{13}, (c) and α-AlFeSi, (f) are shown according to the orientation relationship of the bulk phases.

A vacuum layer of >10 Å was introduced along the z-direction to avoid periodic interaction between interfaces. At least 6 layers of aluminum and the relevant intermetallic compound were considered in our calculations to reduce surface effects.

Liu et al. [9] also studied and reported Orientation Relationships (OR) for Al//Fe_4Al_{13} interfaces and claimed $[020]_{\mathrm{Al}}$ // $[010]_{\mathrm{Fe_4Al_{13}}}$ to be the lowest mismatch direction due to the higher possible symmetry of the intersection group (2/m). They reported a mismatch of 0.18% along the $[020]_{\mathrm{Al}}$ // $[010]_{\mathrm{Fe_4Al_{13}}}$ direction.

In the case of the Al(001)//α-AlFeSi(001) interface, both lattice directions were equally strained. The lattice mismatch between Al and α-AlFeSi was found to be 0.89 % for the OR studied in this paper (Table 2). Due to the small lattice mismatch, this Al(00$\bar{3}$)//α-AlFeSi(001) interface orientation is a likely OR for the Al//α-AlFeSi interface structure.

The matched interface structures are shown in Fig. 2. Fig. 2(a) and (c) show the un-relaxed strained interface structures. The DFT optimized structures are shown in Fig. 2 (b), and (d), and these were used further for the virtual tensile and shear tests.

Table 2: Lattice strain for Al//Fe_4Al_{13} and Al//α-AlFeSi interfaces. In the table the angles are defined as $\Delta\gamma = \gamma_2 - \gamma_1$.

	Strain along a (%)	Strain along b (%)	Difference in angle ($\Delta\gamma$)
Al(100)//Fe_4Al_{13}(100)	0.0	0.10	$\Delta\gamma = 0.0°$
Al(001)//α-AlFeSi(001)	0.89	0.89	$\Delta\gamma = 0.0°$

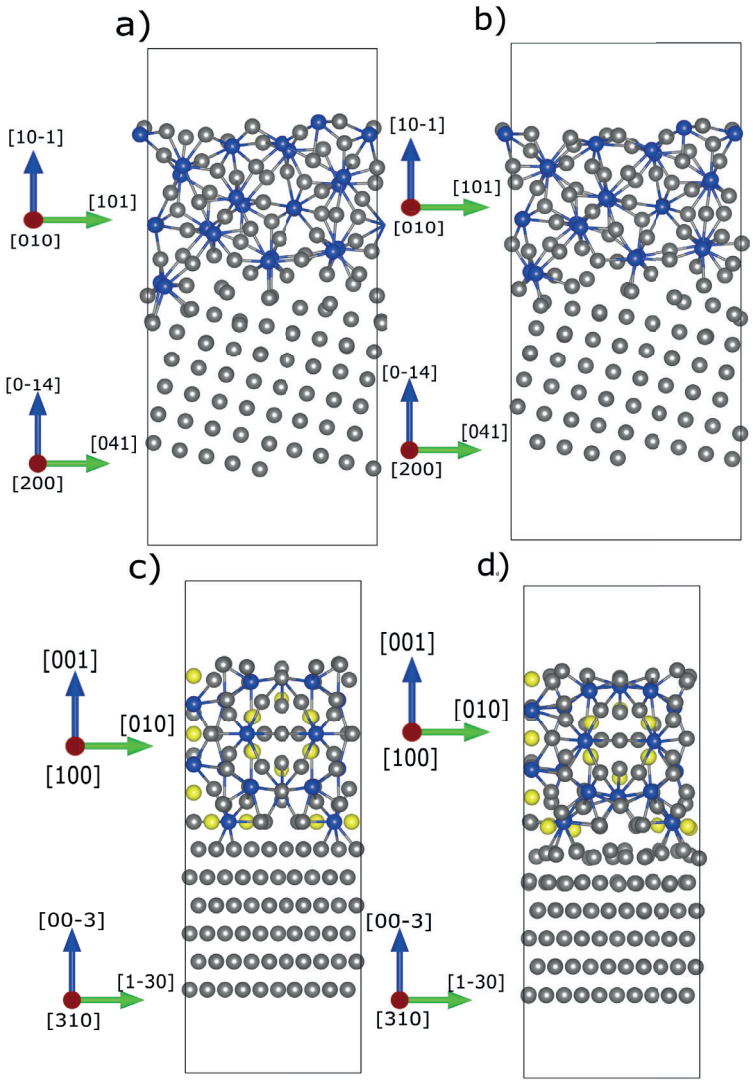

Figure 2: The interface structure of Al//Fe_4Al_{13} (a,b) and Al//α-AlFeSi (c,d). (a,c) show the interface structures before relaxation, while (b,d) show the structures after relaxation, for which the minimum forces on ions were reduced to < 0.01eV/Å^2.

Table 3: The ideal work of separation, W_{sep}, of the Al//α-AlFeSi and Al//Fe_4Al_{13} interfaces and bulk in units of J/m^2. (0) represent the crack opening at the interface, and $(+1)$, $(+2)$, and $(+3)$ and (-1), (-2), and (-3) represent the crack opening at the at the 1st, 2nd and 3rd atomic layers of Al and IMC (α-AlFeSi and Fe_4Al_{13}), respectively, counting from the interface (0), while bulk Al, bulk IMC are the W_{sep} of pure Al and IMCs, respectively.

	Al // α-AlFeSi	**Al // Fe_4Al_{13}**	**Al // Fe**
bulk IMC	2.90 (α-AlFeSi)	3.17 (Fe_4Al_{13})	-
-3	3.42 (α-AlFeSi)	3.46 (Fe_4Al_{13})	-
-2	3.64 (α-AlFeSi)	1.15 (Fe_4Al_{13})	-
-1	3.20 (α-AlFeSi)	4.08 (Fe_4Al_{13})	-
0	2.26	2.21	5.84^a
+1	1.90 (Al)	1.997 (Al)	-
+2	1.82 (Al)	2.06 (Al)	-
+3	1.94 (Al)	2.21 (Al)	-
bulk Al	2.07 (1.8^b)	2.10 (2.10^b)	1.8^b

^{a} [31] ^{b} [32]

3 Interface Strength Calculations

3.1 Ideal work of separation.

The ideal work of separation is the reversible work required to separate the interfaces into free surfaces, ignoring the plastic and diffusion degrees of freedom. It is defined as [29, 30]:

$$W_{sep} = \frac{E_1^{tot} + E_2^{tot} - E_{12}^{tot}}{A} \tag{1}$$

where E_i^{tot} is the total energy of the constituent slab, E_{12}^{tot} is the total energy of the interface, and A is the interface area. To make consistent comparisons of constituent slabs and the interface, the shape and volume of the slabs and interface remain the same. Table 3 lists the work of separation of Al(00$\bar{3}$)//α-AlFeSi(001) and Al(0$\bar{1}$4)//Fe_4Al_{13}(10$\bar{1}$) interfaces.

Under tensile load, a fracture can occur at the different interface layers. Thus it is necessary to calculate the work of separation W_{sep} inside the different layers and compare it with the work of separation W_{sep} at the interface. W_{sep} at the interface and different interface layers are defined as 0 and ±1, ±2, ±3, respectively, while bulk Al and bulk IMC are W_{sep} for pure bulk Al and IMCs. An illustration is shown in Fig. 3. Since the interfacial strength is defined at the weakest point of

the interface structure, this comparison will give indications of the location of the most vulnerable zone [30].

W_{sep} was calculated for both Al metal and the IMCs α-AlFeSi and Fe_4Al_{13}. We calculated W_{sep} for the fracture between Al//IMC counting from interfaces between first, second and third layers, represented as +1, +2, and +3 from the Al side and -1, -2 and -3 from the IMC side, respectively. Generally, the IMCs were found to have higher W_{sep} than Al except for the second layer of Fe_4Al_{13} (1.15 J/m^2). Therefore, the second layer (-2) of Fe_4Al_{13} can be assumed to be the weakest zone of the overall Al//Fe_4Al_{13} interface. This weakening effect of Fe_4Al_{13} can be caused by charge depletion from the second layer towards the interface side. The charge density plot in Subsection 3.6 further explains the reason for this lower value of W_{sep}. Overall, Fe_4Al_{13} showed higher W_{sep} than the α-AlFeSi phase, with the highest value reported to be 4.08 J/m^2 at the -1 side of the IMC.

For the Al//α-AlFeSi interface, W_{sep} is larger at the interface than in Al, implying that the fracture is more likely to occur inside the Al metal. The W_{sep} at +2 was noted to be the smallest compared to the other layers of metal. For the Al//Fe_4Al_{13} interface, W_{sep} was also found to be larger at the interface, implying that the interfacial strength of Al//Fe_4Al_{13} is higher at the interface than in the Al side. For both interface structures, W_{sep} showed a lower value for the bulk IMC and bulk Al, as compared to W_{sep} at the interface.

Moreover, to define a baseline, Al // IMC values were compared with the pure Al // Fe interface structure. Al // Fe interface showed a higher value of W_{sep} (5.84 J/m^2) [31] than Al // IMC interfaces, which indicates the presence of IMCs have a detrimental effect on the aluminum and steel joint.

3.2 Virtual tensile test calculations

Ab-initio tensile calculations of Al//Fe_4Al_{13} and Al//α-AlFeSi interfaces were carried out in the framework of the Rigid Grain Shift (RGS) and RGS+relaxation methodologies [33–35]. In this approach, the equilibrium structures were first shifted along the direction normal to the interface. At each displacement, a vacuum layer was added between the relevant IMC and Al at the interface. For each displaced structure, two kinds of calculations were performed: (1) RGS without any atomic relaxations, and (2) RGS+relaxation, where atomic positions were allowed to relax with the cell size fixed. For the RGS+relaxation methodology, the interface structure was separated along the normal direction by introducing a vacuum, and then DFT calculations were performed by allowing relaxation of atomic positions. The introduced strain between the two surfaces was increased with equal steps until the two phases fractured and split into two free surfaces. During the relaxation

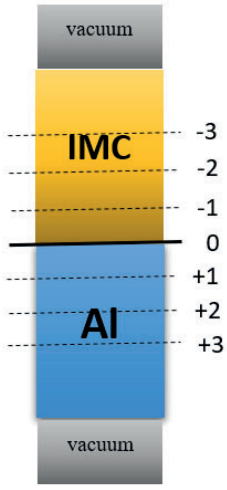

Figure 3: Schematic illustration of W_{sep}. W_{sep} is calculated for fracture taking place at the interface (0), at the first layer $(+1)$ of the Al side or the IMC side (-1), as well as at the second and third layers, W_{sep} is defined at +2(Al), -2 (IMC), and +3 (Al), -3(IMC) respectively.

process for the RGS+relaxation methodology, the top two layers of Al and IMCs were fixed, such that during relaxation, atoms will not converge into another interface structure by relaxation of atomic positions into the vacuum layer introduced at the top of the structures. Fig. 4 illustrates the procedure for the tensile separation for the RGS+relaxation methodology. Each interface structure is divided into three regions. In the first region atoms are fixed and do not move during atomic relaxation, while in the second region, atoms are allowed to relax. The third region is defined as the tensile elongation region, where the vacuum layer is introduced between the two phases to mimic tensile behavior. Ideally, tensile calculations should be performed by introducing strain and allowing the structure to relax by optimizing the lateral lattice parameters to consider Poisson's effect. However, this methodology is very time-consuming and computationally expensive. Besides, the structural relaxation becomes difficult to converge for large strain values [35]. For these reasons, we did not consider Poisson's effect in this study.

The energy-displacement data obtained from the virtual tensile tests were fitted with the so-called Universal Binding Energy Relationship (UBER) [32, 36, 37]. Rose et al. [38] suggested that the binding energy of metals has a universal form of the kind given as;

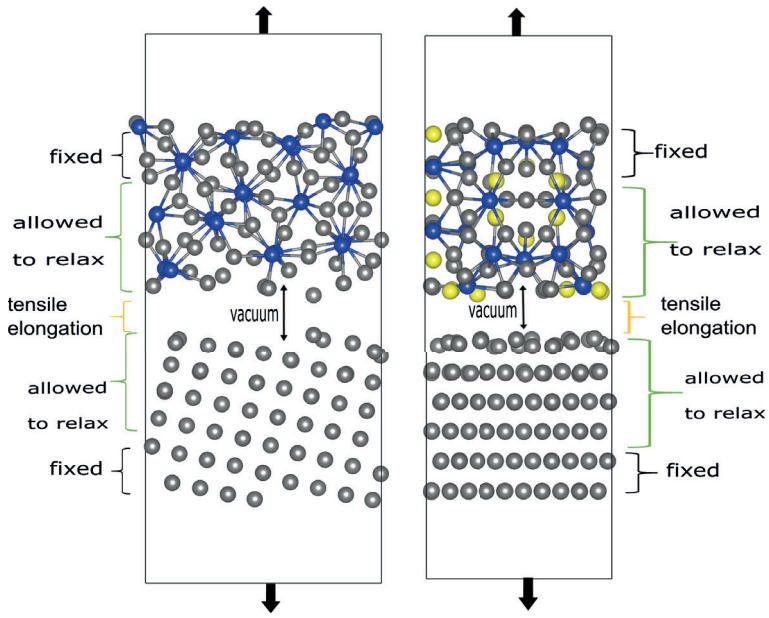

Figure 4: Schematic illustration of the tensile elongation for the RGS+relaxation methodology. for the compression test, equilibrium structures are moved toward each other.

$$E_b(d) = |E_b^e| \cdot g(a) \tag{2}$$

where E_b^e is the binding energy of the equilibrium structure, d is the displacement and a is the re-scaled displacement given as, $a = d/l$, where l is a characteristic length, depending on the curvature of the energy-volume curve at its minimum,

$$l = \sqrt{\frac{|E_b^e|}{E_b^{''}(0)}} \tag{3}$$

If the functional form $g(a)$ is known, we can determine the theoretical strength and critical displacement of any material from the parameters E_b^e and $E_b^{''}$. For the hydrostatic compression/expansion, $g(a)$ is determined to have the following mathematical form [39]:

$$g(a) = -(1 + a + P(a))e^{-a-Q(a)} \tag{4}$$

where P and Q are polynomials of order two or larger. This expression for $g(a)$ ensures that $g(0) = -1$, $g(a \to \infty) = 0$ and $g'(0) = 0$. The first-order terms

are excluded from P and Q since they are related to each other as well as to the characteristic length [39].

By differentiating Eq. (2), the theoretical tensile strength of the atomic structures can be evaluated [36];

$$\sigma_{th} = \frac{\partial E_b}{\partial d} \tag{5}$$

The maximum value of the theoretical strength σ_{th} is defined as the Ultimate Tensile Strength (σ_{UTS}), and the displacement at which σ_{UTS} is achieved is defined as the critical length d_c.

For the Al//α-AlFeSi interface, a good fit was found during RGS calculations. During RGS+relaxation calculations, higher-order polynomials were also considered. Although we found a reasonable fit using a fifth order polynomial, it does not fit the data for higher displacements. To find a good fit at higher displacements, we included an additional odd-order term for the RGS+relaxation methodology. Appendix Tables 6 and 7 list the terms and coefficient values for both methodologies.

Similarly, for the case of the Al//Fe_4Al_{13} interface, higher-order polynomials were used to fit the RGS+relaxation curve. The results obtained from the UBER fit are explained in the following subsections.

3.3 Rigid virtual tensile tests

Starting from the optimized structures, virtual compression and virtual tensile tests were performed as mentioned in Subsection 3.2 without atomic relaxation. The energy increase for the compression tests was also calculated. Fig. 5 (a) and (b) shows the virtual tensile test results for Al//α-AlFeSi and Al//Fe_4Al_{13} interface structures strained along the normal [100] and [10$\bar{1}$] directions, respectively. Values of E_b^e and l as defined by the UBER form in Eq. (2) for the Al//α-AlFeSi interface are 2.26 J/m^2 (0.14 eV/Å^2 = 2.26 J/m^2) and 0.317 Å, respectively, and those for Al//Fe_4Al_{13} are 2.21 J/m^2 and 0.643 Å, respectively (Table 4). As can be seen in Fig. 5(a), at small tensile separations, a parabolic dependence of the binding energy is observed. With increasing displacement, there is a continuous increase in binding energy. The rate of this increase gets lower as the tensile displacement increases until it saturates at larger displacements of the fracture surfaces. Moreover, the UBER results fit well for the RGS methodology. From Fig. 5(a), we can see that the Al//α-AlFeSi interface has a slightly lower binding energy value (0.14 eV/Å^2) than Al//Fe_4Al_{13} (0.1376 eV/Å^2), which indicates marginally stronger resistance to interfacial fracture for the Al//α-AlFeSi interface as com-

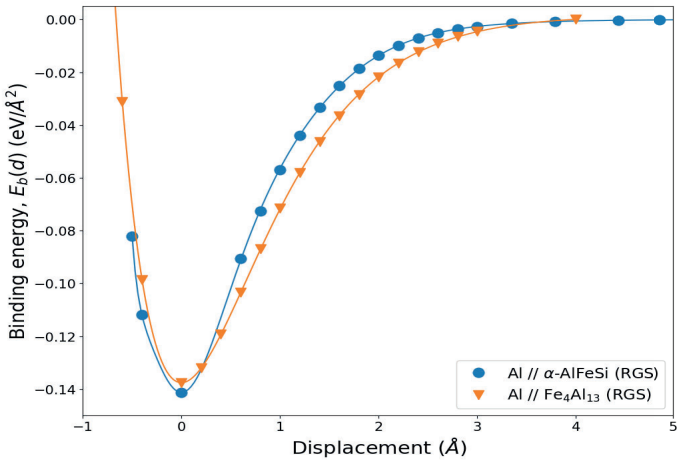

(a) Binding energy versus interfacial separation.

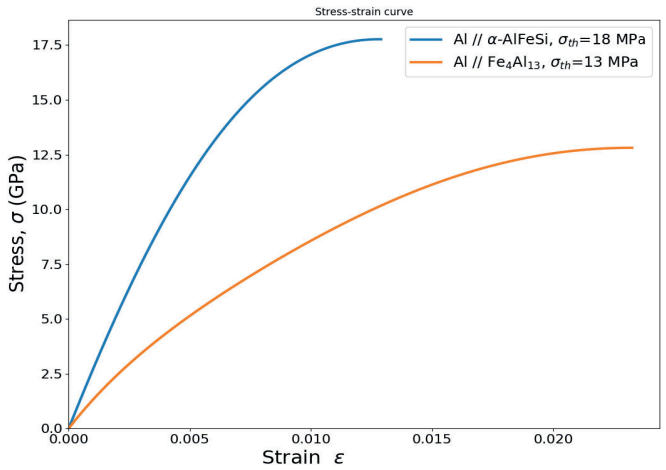

(b) Stress-strain curve

Figure 5: (a) RGS virtual tensile tests for the Al//α-AlFeSi and the Al//Fe_4Al_{13} interface structures. The solid curve represents the fitting of the universal binding-energy relation (UBER) (b) Stress-strain curve plotted by differentiating the UBER curves given in (a), up to the value of the strain corresponding to σ_{UTS}.

pared to Al//Fe_4Al_{13}. The theoretical strength can be calculated from the fitted binding energy curve.

The theoretical stress-strain relations of the Al//α-AlFeSi and Al//Fe_4Al_{13} interfaces are plotted in Fig. 5(b). To make comparisons with other studies, we performed additional virtual tensile tests for Al (210) bulk as well. As given in Table 4, σ_{UTS} for Al (210) bulk was found to be lower than σ_{UTS} of both Al//Fe_4Al_{13} and Al//α-AlFeSi interface structures. This shows that during virtual tensile testing, the fracture is more likely to occur in the bulk aluminum side than at the interface. Since RGS virtual tensile testing was performed by rigidly separating the two surfaces from the interface, this result is consistent with our previous calculations.

Since Fe_4Al_{13} and α-AlFeSi IMCs are stronger than aluminum, bonding of these strong IMCs with Al could be the reason for the higher interfacial strength. Furthermore, Al//Fe_4Al_{13} showed lower σ_{UTS} (12.81 GPa) than Al//α-AlFeSi (17.76 GPa). Generally, the trend in σ_{UTS} follows the W_{sep} values: the higher W_{sep}, the higher σ_{UTS} value [37]. The same trend can be found for Al//Fe_4Al_{13} and Al//α-AlFeSi interface structures. However, σ_{UTS} obtained from RGS virtual tests are most probably overestimated, which is why relaxed-type RGS virtual tensile tests were also performed. Such virtual tests are discussed in the following subsection.

3.4 Relaxed virtual tensile tests

In the relaxed-type virtual tensile tests, atoms were allowed to relax during the virtual tensile tests. Fig. 6 (a) and (b) show the binding energy versus displacement curve for the Al//Fe_4Al_{13} and Al//α-AlFeSi interfaces, evaluated by the RGS+relaxation methodology. Close to the 0 eV/Å^2 binding energy where the interface structures are separated into slabs, bulk atoms relax into minimum energy configuration in the RGS+relaxation methodology, hence the reference structure is different for RGS and RGS+relaxation methodologies at the same tensile displacement.

The equilibrium binding energy E_b^e during RGS virtual tensile tests can also be characterized as the energy required to separate an interface structure into two free surfaces ($E_b(0)$=- W_{sep}). In the case of RGS+relaxation virtual tests, this energy corresponds to the energy needed to separate an interface into two relaxed surfaces. As the interfaces are separated along the normal direction, we see that the binding energy asymptotically reaches separating energy. From the RGS+relaxation methodology, we can also determine the tensile limit beyond which the pre-crack introduced during tensile displacement can no longer be healed.

The binding energy curve is divided into three distinct regions [36]: Region I: ($d < d_c$): the pre-crack introduced during tensile separation is healed up by elastic

relaxations for small displacements, and surfaces will be reconnected, Region II ($d_c < d < d_f$): the so-called instability region, where the crack can neither be healed nor are the interface structures completely separated, and Region III ($d > d_f$): at larger displacements, the interface structure is fractured and the corresponding surfaces are completely separated.

Table 4 lists d_c and d_f for both interface structures. There is no unique way of defining final fracture length d_f, but we define it to be the displacement where the binding energy reaches -0.003 eV/Å^2. The range of the instability region gives indications of the brittleness and ductility of the interface structures and is defined by the difference between d_f and d_c. Al//α-AlFeSi has a lower range of the instability region (0.86 Å) as compared to Al//Fe_4Al_{13} (1.43 Å), which indicates that the former interface is more brittle than the latter one.

3.5 Theoretical tensile strength

Table 4 lists all the calculated values of σ_{UTS} for the Al//Fe_4Al_{13} and Al//α-AlFeSi interface structures, obtained by both the RGS and RGS+relaxation methodologies. The RGS+relaxation type tensile calculations show a lower tensile strength than the RGS tensile calculations. This is due to the fact that increased degrees of freedom during the atomic relaxation increases the possibility of failure initiation.

The maximum value of the stress-strain curve i.e. σ_{UTS} for Al//Fe_4Al_{13} is 13.17 GPa as compared to 17.27 GPa for the Al//α-AlFeSi interface structure in the RGS methodology. As expected, the RGS+relaxation type virtual tensile tests show lower tensile strength at larger critical length values. The larger d_c value for the RGS+relaxation methodology is caused by the stretching of the whole system [40]. The Al//Fe_4Al_{13} interface shows higher critical length than the Al//α-AlFeSi interfaces for both methodologies. As given in Table 4, d_c is significantly higher in the case of RGS+relaxation methodology than the RGS method for all structures.

Similarly, the Al//Fe_4Al_{13} interface shows lower σ_{UTS} (9.85 Å) than the Al//α-AlFeSi (10.92 Å) interface during RGS+relaxation. As discussed in the previous subsection, the higher strength is caused by the movement of Al atoms during elastic relaxation. Generally, the failure should preferentially initiate at the interfacial Al-Al in the Al//Fe_4Al_{13} interface (region I in Fig. 8) and at Si-Al for the Al//α-AlFeSi interface (region I in Fig. 7) due to the weak bonding zone. This crack formation mechanism will be further elucidated in the next subsection.

The tensile strength of the Al(210) plane was calculated separately, and the results are reported in Table 4. It is worth noting that our RGS+relaxation calculations show good agreement with Zhang et al. [41] and Cerny et al. [42]. Comparing the bulk Al mechanical strength with IMC interfaces show that the Al bulk side is the

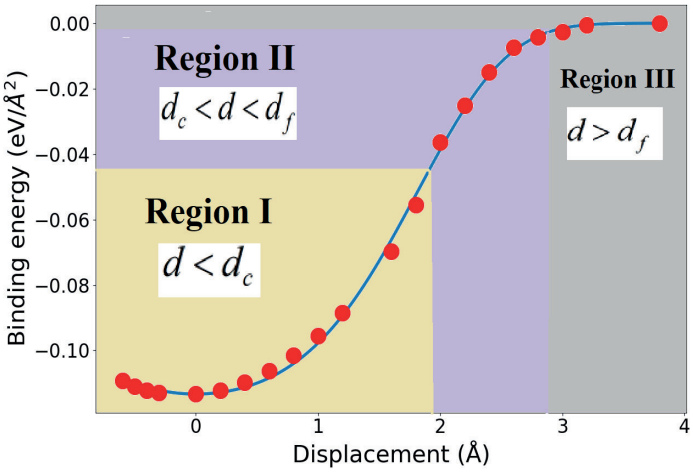

(a) Al//α-AlFeSi interface.

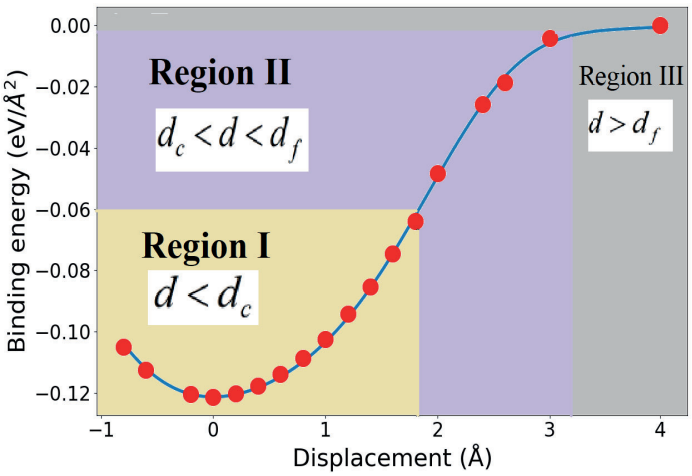

(b) Al//Fe_4Al_{13} interface.

Figure 6: Binding energy versus tensile displacement of (a) Al//α-AlFeSi and (b) Al//Fe_4Al_{13} interfaces in RGS+relaxation type virtual tensile tests.

Table 4: Ultimate tensile strength and fitting parameters of Al(210) bulk, Al//α-AlFeSi and Al//Fe_4Al_{13} calculated by RGS and RGS+relaxation methodologies. d_c, d_f and l are the critical length, final fracture length and characteristic length.

Interface	Rigid shift (RGS) σ_{UTS} (GPa)	RGS+relaxation σ_{UTS} (GPa)	d_c (Å)	l (Å)	d_f (Å)
Al(210)	10.11 11.96 [36]	8.99 9.39 [36] 8.40 [41]	1.45^a 3.03^b	1.471^a 2.810^b	6.20^b
Al//Fe_4Al_{13}	13.17	9.85	0.6^a 1.80^b	0.643^a 1.483^b	3.18^b
Al//α-AlFeSi	17.27	10.92	0.43^a 1.94^b	0.317^a -1.180^b	2.86^b

^{a} RGS
^{b} RGS+relaxation

weakest zone of the overall interface structure. Incorporation of Poisson's effect in uniaxial tensile tests will most probably reduce σ_{UTS}. However, as mentioned earlier, due to the limited number of atoms and the computational costs associated with it, we did not consider Poisson's contraction in our ab-initio tensile calculations.

3.6 Charge density

The fracture behavior of the RGS+relaxation type virtual tensile tests can be analyzed further by the electronic charge density of the interface structures. As shown in Fig. 7, in the stable configuration, the interfacial Si atoms face Al and Fe atoms, and the charge density between Si and Fe atoms is relatively high on the upper layers of α-AlFeSi. There is a charge depletion region between interfacial Al-Si atoms, as shown in region I in Fig. 7. This charge depletion region increases with the increase in tensile displacement. At 2.4 Å displacement of Al//α-AlFeSi interface, the charge density between interfacial Al-Al atoms is higher than that of the interfacial Si-Al pair. This indicates that bonding between interfacial Si-Al is weaker than the interfacial Al-Al bonding. As the tensile displacement increases, interfacial Si atoms move towards α-AlFeSi, and charge depletion region I increase, until the interface structure splits into two surfaces at a displacement of $\sim$2.8 Å.

In the case of the Al//Fe_4Al_{13} interface structure shown in Fig. 8, we can see higher charge density regions between Fe-Al atoms at the equilibrium configuration (0 Å) on the second layer of Fe_4Al_{13}. The charge depletion region at zero displacements can be seen between interfacial Al-Al atoms as well. Charge depletion regions are marked as regions I and II at 1.8 Å. As the tensile displacement increases, these depletion regions grow in size. The depletion region marked as II, which can also

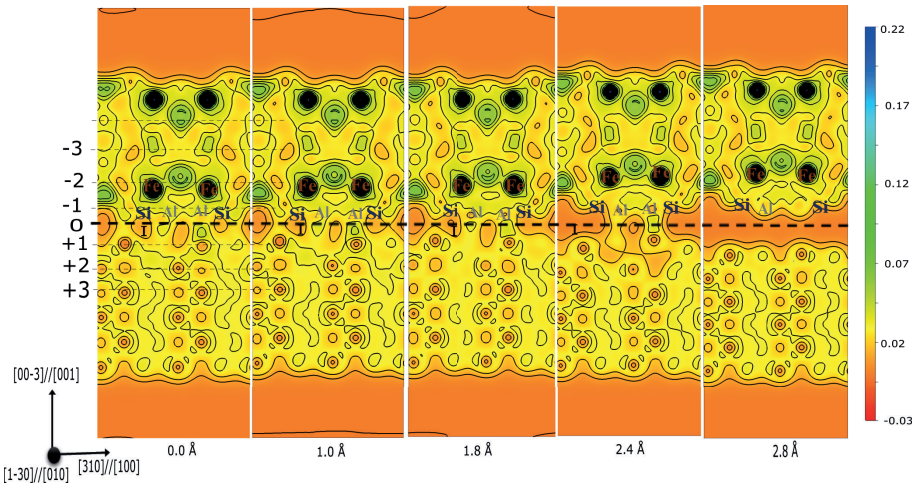

Figure 7: Calculated charge density of the Al//α-AlFeSi interface during increased displacement (d), evaluated in the RGS+relaxation methodology in units of e/Å^3. Atomic layers ($\pm$1, $\pm$2, $\pm$3) are marked as per the definition of Fig. 3.

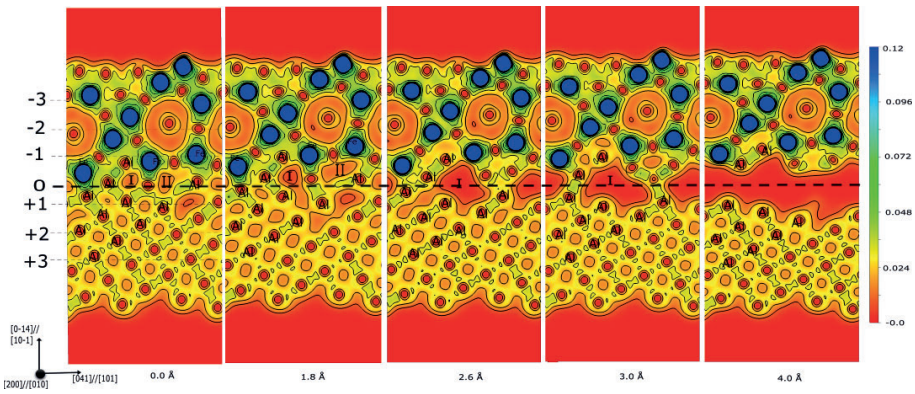

Figure 8: Calculated charge density of Al//Fe_4Al_{13} interface during increased displacement (d), evaluated in the RGS+relaxation methodology in units of e/Å^3. Atomic layers ($\pm$1, $\pm$2, $\pm$3) are marked as per the definition of Fig. 3.

be seen at 0.0 Å and 1.8 Å, is reconnected by elastic relaxation at a displacement of 2.6 Å, but depletion region I still grow in size. This shows that the Al atoms move towards the Fe atoms during tensile separation. At a tensile displacement of 3.0 Å, we can see that the depletion regions have become wide, but still, the charge density is relatively large between interfacial Al-Al atoms, which exhibit large resistance to complete interfacial separation. The Al//Fe_4Al_{13} interface structure splits up into two free surfaces at d_f (∼3.13 Å).

On the Fe_4Al_{13} side in Fig. 8, we can see a spherically shaped charge depletion region at the second layer. This depletion region can explain the lower W_{sep} value at the second layer of the Fe_4Al_{13} side, as discussed in Subsection 3.1. This is also a very interesting observation, which shows that Fe_4Al_{13} could be very anisotropic and brittle due to the existence of such weak zones. Comparing Fig 7 and Fig. 8, the Al//Fe_4Al_{13} interface splits up at a larger tensile displacement than the Al//α-AlFeSi interface, which again confirms the longer range of the instability region for the Al//Fe_4Al_{13} interface structure.

The long range of charge decay at the atomic scale for the Al//Fe_4Al_{13} interface allows atoms to find alternate modes of energy dissipation, such as atomic stretching to bridge the void. At the macroscopic level, this behavior can result in the formation of dislocation planes over crack-tip propagation [43].

3.7 Ideal shear strength

To calculate the ideal shear strength of Al//IMC interfaces, a series of incremental strains were introduced along the x- and y-directions, respectively. For the Al(001)//α-AlFeSi(001) interface, the atoms of α-AlFeSi were rigidly moved along the [010] and [100] directions by keeping the cell size fixed. Similarly for the Al//Fe_4Al_{13} interface, Fe_4Al_{13} layers were moved along the [010] and [101] directions, respectively, as shown in Fig. 9 (a,b,c and d). During shear calculations, atoms were allowed to relax along the normal direction to the interface. Furthermore, to avoid periodic interaction between structures, a vacuum layer of >10 Å was added for all interfaces. Shear stress was calculated and plotted as a function of shear displacement along the defined slip directions according to the following Fourier series expression,

$$E_s(d) = E_0 + \sum_{i=1}^{\infty}[A_i cos(k_i d) + B_i sin(k_i d)] \tag{6}$$

where $E_s(d)$ and E_0 are the energy of the displaced and reference structure respectively, and k_i=$\frac{2\pi i}{\lambda}$, where λ is the periodicity along the shear direction.

Due to the periodicity of the crystal structure along the shear direction, a Fourier

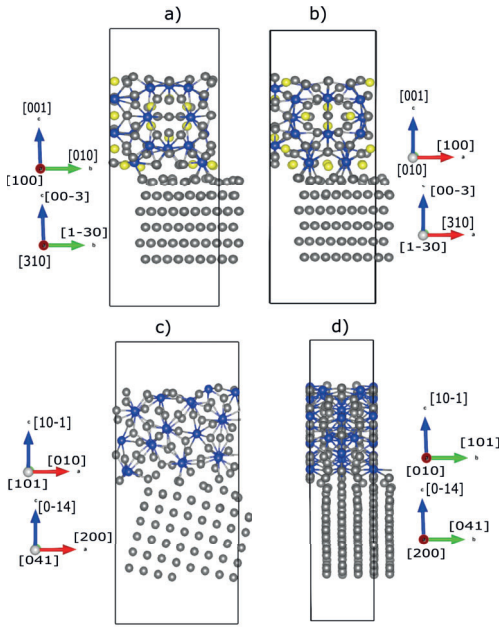

Figure 9: Schematic illustration of the directions of shear for Al//α-AlFeSi (a, b) and Al//Fe_4Al_{13} (c, d).

Table 5: Ideal shear strength of the Al//α-AlFeSi and Al//Fe_4Al_{13} interfaces. Direction of shear is defined with respect to Al along $< 101 > < 010 >$ and $< 100 >$ direction.

Interface	$\gamma_{max} < 101 >$ (GPa)	$\gamma_{max} < 010 >$ (GPa)	$\gamma_{max} < 100 >$ (GPa)
Al//α-AlFeSi	-	2.23	3.14
Al//Fe_4Al_{13}	5.11	7.65	-

series was used to fit shear stress-displacement data. The shear stress is calculated as;

$$\gamma_s = \frac{1}{A}\frac{\partial E_s}{\partial d} \tag{7}$$

where A is the area of the interface structures.

We used a Fourier series of order $n = 3$ to fit the shear stress-displacement curve. The shear stress-displacement curve fits well with the Fourier series Eq. (6), as can be seen in Fig. 10 (a) and (b) for both interface structures.

Fig. 10 shows the stress-displacement curves for the Al//α-AlFeSi and Al//Fe_4Al_{13} interface structures as a function of shear displacement along the shear directions. Table 5 summarizes the shear strength of various slip systems of interface struc-

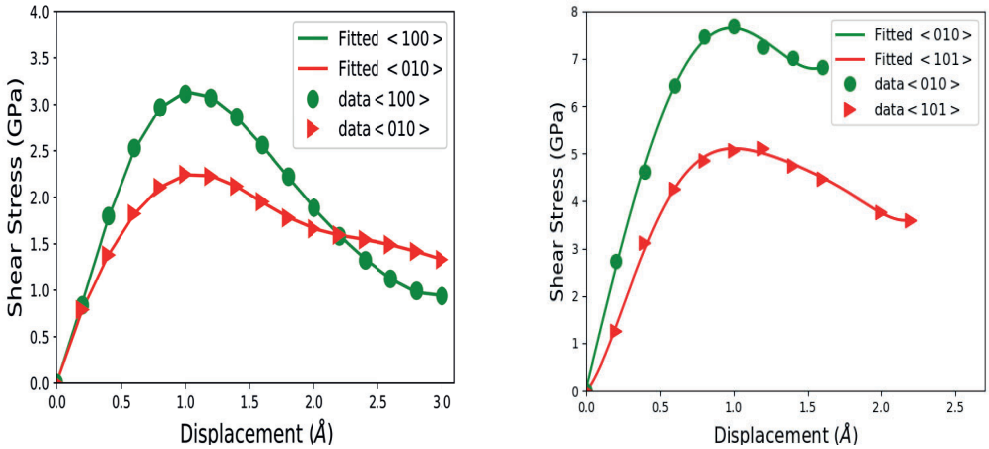

(a) Al (001)//α-AlFeSi(001) interface

(b) Al $(0\bar{1}4)$//Fe_4Al_{13} $(10\bar{1})$

Figure 10: Shear stress-displacement curve of the Al$(00\bar{3})$//α-AlFeSi(001) and Al$(0\bar{1}4)$//Fe_4Al_{13} $(10\bar{1})$ interfaces during the shear strength simulations as a function of shear displacement along different shear directions.

tures considered in this study. As can be seen in Fig. 10, the stress increases initially until it reaches a maximum value. The maximum is defined as the ideal shear strength of the interface structures in this study (γ_{max}). For the Al//α-AlFeSi interface, the most favorable slip direction is found to be along $< 010 >$ with the ideal shear strength value of 2.23 GPa, while higher strength was found along the $< 100 >$ shear direction (3.14 GPa). The Al//Fe_4Al_{13} interface shows higher strength with the highest value found along the $< 010 >$ direction (7.65 GPa) while lower along $< 101 >$ direction (5.11 GPa). Based on these values, it can be concluded that the Al//Fe_4Al_{13} interface has higher shear strength as compared to the Al//α-AlFeSi interface.

The atoms at the Al//α-AlFeSi interface are aligned in a straight line, as can be seen in Fig. 9 (a) and (b). During the shearing process along the [010] and [100] directions, these atoms do not face any energy barrier caused by other atoms. However, in the case of the Al//Fe_4Al_{13} interface, atoms are aligned in a zig-zag manner at the interface along the [010] direction (Fig. 9 (c)), which creates a barrier during the shearing process. The maximum shear strength is achieved when this energy barrier has been overcome by the shearing displacement along the particular slip direction. This causes the higher shear strength for the Al//Fe_4Al_{13} interface along the [010] direction. Lower strength has been found along the [101] direction due to the straight alignment of atoms at the interface.

4 Discussion

Virtual tensile and shear calculations were performed to selected Al//IMC structures and thereby obtaining insights into the governing mechanisms of Fe_4Al_{13} and α-AlFeSi intermetallics at aluminum and steel joints. To our best knowledge, this paper contains the first detailed first-principles study of Al//Fe_4Al_{13} and Al//α-AlFeSi intermetallic interfaces.

Calculations of W_{sep} gave indications of the location of the weakest zone of the interface and the bulk sides. Interestingly, the second layer of Fe_4Al_{13} was found to be the weakest zone of the whole Al//Fe_4Al_{13} structure, as discussed in Sec. 3.1. Charge density plots indicated a charge depletion region around Fe atoms at the second layer of the Fe_4Al_{13} intermetallic side (Fig. 8). Although Fe_4Al_{13} seems to have the highest strength, the presence of this weak zone is a possible explanation of the highly anisotropic behavior of the Fe_4Al_{13} layers. Therefore, it can be suggested from these calculations that micro-cracks are more likely to develop in Fe_4Al_{13} due to the presence of charge depletion regions. On the other hand, α-AlFeSi showed consistent values of W_{sep} (Table 3). The α phase showed a higher W_{sep} values, which indicates that this phase has stronger bonding characteristics as compared to the Fe_4Al_{13} phase and less likely to induce micro-cracks. Generally, the Al side was found to be softer than the intermetallic layers except for the second layer of Fe_4Al_{13}. At the interface, the Al//α-AlFeSi interface showed a higher W_{sep} value (2.26 J/m^2) than Al//Fe_4Al_{13}, which is an indication of higher mechanical strength.

Tensile calculations of these interface structures also agree with the W_{sep} values. The Al//α-AlFeSi interface showed higher interfacial strength as compared to the Al//Fe_4Al_{13} interface structure. Charge density plots indicated that the Si atoms at the interface tend to induce cracks at the interface side, while Al atoms seem to have stronger bonding with interfacial Al atoms. Similarly for the Al//Fe_4Al_{13} interface, Fe atoms of the Fe_4Al_{13} phase seem to have stronger bonding strength with the interfacial Al atoms. Hence it is reasonable to suggest that the presence of Fe atoms at the interface produces stronger bonding than Al and Si atoms. Al atoms tend to show more ductile behavior than Fe atoms, which produce an energy barrier along the shearing direction. To have a shear along the particular shearing direction, the energy barrier created by the interfacial bonding has to be overcome by the shearing process. Al atoms create a higher energy barrier, and there are more Al atoms at the Al//Fe_4Al_{13} interface than at the Al//α-AlFeSi interface, which is why the Al//Fe_4Al_{13} interface shows a higher shear strength. From these calculations, it can be suggested that the presence of Fe atoms at the interface produces stronger tensile strength, while higher shear strength is achieved by the

Al atoms at the interface.

5 Conclusions and Outlook

We have developed and performed ab-initio calculations of Al//Fe_4Al_{13} and Al//α-AlFeSi interface structures. To characterize the interfacial strength, we calculated W_{sep} to find the weak zone of the interface structure. The Al//α-AlFeSi interface was found to have a higher W_{sep} value than the Al//Fe_4Al_{13} interface. Besides, the W_{sep} values show that during uni-axial tension, the interface is most likely to fracture from the Fe_4Al_{13} side with the lowest value reported to be 1.15 J/m^2 for the Al//Fe_4Al_{13} interface. This low value of W_{sep} is caused by the spherical charge depletion region in the second layer (-2) in Fe_4Al_{13}.

Furthermore, a series of tensile calculations were performed in the framework of the RGS methodology both with and without the relaxation of atomic positions at each shift. These tensile simulations yielded energy-displacement data, which were fitted by the UBER curve. Based on these calculations, the Al//Fe_4Al_{13} interface structure has a lower ultimate tensile strength than the Al//α-AlFeSi interface. Shear strength calculations were also performed for the Al//Fe_4Al_{13} structure along the $< 101 >$ and $< 010 >$ shear directions, and for Al//α-AlFeSi along $< 100 >$ and the $< 010 >$ directions. As displayed in Tables 4 and 5, the Al//α-AlFeSi interface showed higher tensile and lower shear strength as compared to the Al//Fe_4Al_{13} interface structure.

It should be emphasized that the effects of temperature, boundaries, cracks, and dislocations have not been taken into account in this study. These defects dominate the failure behavior in reality. At the macroscopic level, the actual strain and stress values are usually small as compared to the ideal stress and strain values. Therefore it is necessary to find strategies to link ab-initio calculations with the macroscopic failure process by Finite Element Modeling (FEM) and molecular dynamics simulations methods [44, 45]. This study is part of a larger project aiming at characterizing the role of IMCs at aluminum-steel joints, and we plan to use ab-initio calculations as input for FEM simulations to predict the macroscopic behavior of aluminum-steel joints.

6 Acknowledgements

The work reported in this paper was based on activities within the centre for research-based innovation SFI Manufacturing in Norway and is partially funded by the Research Council of Norway under contract number 237900. UNINETT Sigma2 AS (The Norwegian Metacenter for High Performance Computing) provided computational resources through Project NN9466K and NN9158K.

7 Appendix

Table 6: The fitting coefficient binding energy E_b(d) values of the Al//Fe_4Al_{13} interface.

Terms	1	2	3	4	5	7	9
RGS	0.0	-0.00542	-0.0247	0.00427	-0.000706	-	-
RGS+relaxation	1.7954	-	-	-	-0.324	0.0681	0.148

Table 7: The fitting coefficient binding energy E_b(d) values of the Al // α-AlFeSi interface.

Terms	1	2	3	4	5	7	9
RGS	0.0	0.305	-0.00145	-0.0125	0.0.00359	-	-
RGS+relaxation	6.232	-	-	-	-40.9955	4.029	47.229

References

[1] H. Wargnier, F. Kromm, M. Danis, Y. Brechet, Proposal for a multi-material design procedure, Materials & Design (1980-2015) 56 (2014) 44–49 (2014).

[2] T. Netland, J. Ravn, G. Knutstad, L. Skjelstad, Idealfactory@ xps: A manufacturing concept for high-tech norwegian companies (2011).

[3] J. Pflug, I. Verpoest, Sandwich materials selection charts, Journal of Sandwich Structures & Materials 8 (5) (2006) 407–421 (2006).

[4] G. N. Levy, R. Schindel, J.-P. Kruth, Rapid manufacturing and rapid tooling with layer manufacturing (LM) technologies, state of the art and future perspectives, CIRP Annals-Manufacturing Technology 52 (2) (2003) 589–609 (2003).

[5] M. Bahraminasab, B. Sahari, K. Edwards, F. Farahmand, T. S. Hong, M. Arumugam, A. Jahan, Multi-objective design optimization of functionally graded material for the femoral component of a total knee replacement, Materials & Design 53 (2014) 159–173 (2014).

[6] M. Pourali, A. Abdollah-Zadeh, T. Saeid, F. Kargar, Influence of welding parameters on intermetallic compounds formation in dissimilar steel/aluminum friction stir welds, Journal of Alloys and Compounds 715 (2017) 1–8 (2017).

[7] J. M. Piccini, H. G. Svoboda, Effect of pin length on friction stir spot welding (FSSW) of dissimilar Aluminum-Steel joints, Procedia Materials Science 9 (2015) 504–513 (2015).

[8] K. Martinsen, S. Hu, B. Carlson, Joining of dissimilar materials, CIRP Annals 64 (2) (2015) 679–699 (2015).

[9] P. Liu, G. Dunlop, Crystallographic orientation relationships for Al-Fe and Al-Fe-Si precipitates in aluminium, Acta Metallurgica 36 (6) (1988) 1481–1489 (1988).

[10] M. Potesser, T. Schoeberl, H. Antrekowitsch, J. Bruckner, The characterization of the intermetallic Fe-Al layer of steel-aluminum weldings, in: EPD Congress, Vol. 1, San Antonio Texas, USA, 2006, p. 167 (2006).

[11] X. Liu, S. Lan, J. Ni, Analysis of process parameters effects on friction stir welding of dissimilar aluminum alloy to advanced high strength steel, Materials & Design 59 (2014) 50–62 (2014).

[12] S. Bozzi, A. Helbert-Etter, T. Baudin, B. Criqui, J. Kerbiguet, Intermetallic compounds in Al 6016/IF-steel friction stir spot welds, Materials Science and Engineering: A 527 (16-17) (2010) 4505–4509 (2010).

[13] Y. Sun, H. Fujii, N. Takaki, Y. Okitsu, Microstructure and mechanical properties of dissimilar Al alloy/steel joints prepared by a flat spot friction stir welding technique, Materials & Design 47 (2013) 350–357 (2013).

[14] N. Chen, H.-P. Wang, B. E. Carlson, D. R. Sigler, M. Wang, Fracture mechanisms of Al/steel resistance spot welds in lap shear test, Journal of Materials Processing Technology 243 (2017) 347–354 (2017).

[15] E. McDevitt, Y. Morimoto, M. Meshii, Characterization of the Fe-Al interfacial layer in a commercial hot-dip galvanized coating, ISIJ international 37 (8) (1997) 776–782 (1997).

[16] K.-K. Wang, L. Chang, D. Gan, H.-P. Wang, Heteroepitaxial growth of Fe_2Al_5 inhibition layer in hot-dip galvanizing of an interstitial-free steel, Thin Solid Films 518 (8) (2010) 1935–1942 (2010).

[17] S. M. Arbo, T. Bergh, H. Solhaug, I. Westermann, B. Holmedal, Influence of thermomechanical processing sequence on properties of AA6082-IF steel cold roll bonded composite sheet, Procedia Manufacturing 15 (2018) 152–160 (2018).

[18] M. Finnis, The theory of metal-ceramic interfaces, Journal of Physics: Condensed Matter 8 (32) (1996) 5811 (1996).

[19] C.-H. Zhang, S. Huang, J. Shen, N.-X. Chen, Structural and mechanical properties of Fe-Al compounds: An atomistic study by EAM simulation, Intermetallics 52 (2014) 86–91 (2014).

[20] Y. Liu, X. Chong, Y. Jiang, R. Zhou, J. Feng, Mechanical properties and electronic structures of Fe-Al intermetallic, Physica B: Condensed Matter 506 (2017) 1–11 (2017).

[21] M. Z. Khalid, J. Friis, P. H. Ninive, K. Marthinsen, A. Strandlie, DFT calculations based insight into bonding character and strength of Fe_2Al_5 and Fe_4Al_{13} intermetallics at Al-Fe joints, Procedia Manufacturing 15 (2018) 1407–1415 (2018).

[22] P. G. Gonzales-Ormeño, H. M. Petrilli, C. G. Schön, Ab-initio calculations of the formation energies of bcc-based superlattices in the Fe-Al system, Calphad 26 (4) (2002) 573–582 (2002).

[23] G. Kresse, J. Furthmüller, Vienna ab-initio simulation package (vasp), Vienna: Vienna University (2001).

[24] P. E. Blöchl, Projector augmented-wave method, Physical review B 50 (24) (1994) 17953 (1994).

[25] J. P. Perdew, K. Burke, M. Ernzerhof, Generalized gradient approximation made simple, Physical Review Letters 77 (18) (1996) 3865 (1996).

[26] H. J. Monkhorst, J. D. Pack, Special points for brillouin-zone integrations, Physical review B 13 (12) (1976) 5188 (1976).

[27] M. Cooper, The crystal structure of the ternary alloy α (AlFeSi), Acta Crystallographica 23 (6) (1967) 1106–1107 (1967).

[28] A. M. F. Muggerud, Y. Li, R. Holmestad, Composition and orientation relationships of constituent particles in 3xxx aluminum alloys, Philosophical Magazine 94 (6) (2014) 556–568 (2014).

[29] I. G. Batyrev, A. Alavi, M. W. Finnis, Equilibrium and adhesion of Nb/sapphire: The effect of oxygen partial pressure, Physical Review B 62 (7) (2000) 4698 (2000).

[30] H. Guo, Y. Qi, X. Li, Adhesion at diamond/metal interfaces: A density functional theory study, Journal of applied physics 107 (3) (2010) 033722 (2010).

[31] M. Z. Khalid, J. Friis, P. H. Ninive, K. Marthinsen, A. Strandlie, A First-Principles Study of the Al (001)/Fe (0-11) Interface, in: Materials Science Forum, Vol. 941, Trans Tech Publ, 2018, pp. 2349–2355 (2018).

[32] P. Lazar, R. Podloucky, Cleavage fracture of a crystal: Density functional theory calculations based on a model which includes structural relaxations, Physical Review B 78 (10) (2008) 104114 (2008).

[33] G. Zhang, M. Chen, Y. Shi, J. Huang, F. Yang, Analysis and modeling of the growth of intermetallic compounds in aluminum–steel joints, RSC Advances 7 (60) (2017) 37797–37805 (2017).

[34] A. Tahir, R. Janisch, A. Hartmaier, Hydrogen embrittlement of a carbon segregated $\sigma 5$ (310)[001] symmetrical tilt grain boundary in α-Fe, Materials Science and Engineering: A 612 (2014) 462–467 (2014).

[35] M. Yamaguchi, First-principles study on the grain boundary embrittlement of metals by solute segregation: Part i. iron (Fe)-solute (B, C, P, and S) systems, Metallurgical and Materials Transactions A 42 (2) (2011) 319–329 (2011).

[36] D. Zhao, O. M. Løvvik, K. Marthinsen, Y. Li, Segregation of Mg, Cu and their effects on the strength of Al $\sigma 5$ (210)[001] symmetrical tilt grain boundary, Acta Materialia 145 (2018) 235–246 (2018).

[37] R. Janisch, N. Ahmed, A. Hartmaier, Ab initio tensile tests of al bulk crystals and grain boundaries: Universality of mechanical behavior, Physical Review B 81 (18) (2010) 184108 (2010).

[38] J. H. Rose, J. R. Smith, J. Ferrante, Universal features of bonding in metals, Physical review B 28 (4) (1983) 1835 (1983).

[39] I. J. Jensen, J. Friis, C. D. Marioara, I. G. Ringdalen, The role of grain boundary precipitates during intergranular fracture in 6xxx series aluminium alloys, In preparation.

[40] R. Yang, S. Tanaka, M. Kohyama*, First-principles study on the tensile strength and fracture of the Al-terminated stoichiometric α-Al_2O_3 (0001)/Cu (111) interface, Philosophical Magazine 85 (25) (2005) 2961–2976 (2005).

[41] S. Zhang, O. Y. Kontsevoi, A. J. Freeman, G. B. Olson, Sodium-induced embrittlement of an aluminum grain boundary, Physical Review B 82 (22) (2010) 224107 (2010).

[42] M. Černỳ, P. Šesták, P. Řehák, M. Všianská, M. Šob, Ab initio tensile tests of grain boundaries in the fcc crystals of ni and co with segregated sp-impurities, Materials Science and Engineering: A 669 (2016) 218–225 (2016).

[43] E. A. Jarvis, R. L. Hayes, E. A. Carter, Effects of oxidation on the nanoscale mechanisms of crack formation in aluminum, ChemPhysChem 2 (1) (2001) 55–59 (2001).

[44] J. Pask, P. Sterne, Finite element methods in ab initio electronic structure calculations, Modelling and Simulation in Materials Science and Engineering 13 (3) (2005) R71 (2005).

[45] C. D. Berweger, W. F. van Gunsteren, F. Müller-Plathe, Molecular dynamics simulation with an ab initio potential energy function and finite element interpolation: the photoisomerization of cis-stilbene in solution, The Journal of chemical physics 108 (21) (1998) 8773–8781 (1998).

Paper IV

Khalid M. Z., Friis J., Ninive P. H., Marthinsen K., Ringdalen I.G., Strandlie A. (2019). First-principles study of tensile and shear strength of an Fe_2Al_5//Fe interface, Submitted to Modelling and Simulation in Materials Science and Engineering.

Paper IV

First-principles study of tensile and shear strength of an Fe_2Al_5//Fe interface

Khalid M. Z., Friis J., Ninive P. H., Marthinsen K., Ringdalen I.G., Strandlie A.

Abstract

Based on density functional theory, we study the bulk Fe_2Al_5 and interfacial strengths of a novel low misfit Fe_2Al_5//Fe interface structure found at the aluminum-steel joints. An interface between Fe and Fe_2Al_5 was selected based on the criteria of low lattice misfit and number of atoms. We show that virtual tensile testing of bulk Fe_2Al_5 and the interface structures result in an energy-displacement curve, which can be well described by including extra polynomial terms in the spirit of well known Universal Binding Energy Relation (UBER). It turns out that the Fe_2Al_5//Fe interface has a higher tensile strength than the bulk Fe_2Al_5 phase. We also find that the shear deformation process can potentially be initiated from the Fe-terminated interface.

Keyword Fe-Al intermetallics; mechanical strength; atomistic simulations; face-to-face matching; welding

1 Introduction

Owing to the increased interest in light-weight and environmental-friendly technology, Fe-Al compounds have been gaining increased industrial interest due to their light-weight, corrosion resistance and high-temperature resistance behavior [1–3].

However, the joining of aluminum and steel by traditional fusion welding techniques has been considered a main challenge due to the significant differences between their physical and chemical properties [4, 5]. The intermetallic compounds (IMCs) developed at the interface are normally not wanted, but unavoidable when welding aluminum and steel.

Various methods have been proposed and studied to join aluminum and steel [3, 6]. For any method which requires high temperatures, a brittle layer of different types of Fe-Al IMCs is developed at the joint, making it difficult to obtain the desired joint strength. Although solid-state welding techniques can suppress the formation of Fe-Al IMCs at joints due to the low temperature, these methods can still not completely limit the formation of IMCs and can thus only produce Fe-Al joints with limited strength.

The thickness of the IMC layers also plays an important role in the strengthening of Fe-Al joints. It has been reported that the thickness of Fe-Al IMC layers formed in a brazed interface can be limited to less than 10 μm, which is considered as the critical thickness of a Fe-Al IMC layer for Fe-Al joints with good mechanical strength [7]. Analyses of Fe-Al joints suggest that the micro-structures and distribution of Fe-Al IMCs at the interface are dependent on heat input, and play an important role in determining the mechanical and/or corrosion behavior of the joints [8, 9]. In general, most of the experimental and theoretical studies on Fe-Al IMC layers focus on, (i) heat input and thickness of IMC layer [10] (ii) welding methodology [11, 12] (iii) tensile and shear strength of IMC layers at the joint [3] and (iv) extended isothermal treatment [13–15].

Despite all these studies, the interfacial strength of intermetallics such as Fe_2Al_5//Fe has not been studied much in literature. Since it is thermodynamically possible to produce a range of Fe-Al compounds at the interface [16, 17], it is necessary to understand the basic mechanical and interfacial strength of all these compounds to establish their roles in the joining process. The lack of convincing results for the interfacial strength is not due to a lack of academic and industrial interests on this important subject. However, due to the small thickness (2.3 ± 0.6 μm) of the IMC layers [18], it is very difficult to experimentally predict the interface strength of these compounds.

The above brief review indicates that the understanding of the behavior and strength of the individual interfaces of these compounds is far from complete, and it is evident that an atomistic study of these interfaces could provide useful new insight. The lack of atomistic studies is due to the complex atomic structure of the intermetallic compounds. It is, therefore, challenging to develop an interface model which is periodic, simple and has a low lattice misfit. In this work, we have used

a face-to-face matching technique to predict a possible Orientation Relationship (OR) between Fe_2Al_5 and Fe suitable for atomistic calculations.

The scope of this paper is limited to establish and test the modeling methodology to find a good atomistic interface structure and to study the mechanical and interfacial properties of the Fe_2Al_5//Fe interface. The study of more complex, but just as vital interface structures such as Fe_4Al_{13}//Al, Al//α-AlFeSi, Fe_4Al_{13}//α-AlFeSi and Fe_2Al_5 // Fe_4Al_{13} will be explored in future work. The structure of the paper is as follows. First, we present the procedure for finding a low misfit interface structure between Fe and Fe_2Al_5. In Sec. 3 we present the calculation methodology and procedure for performing virtual tensile calculations. In Sec. 4, we present results of the strength of the bulk Fe_2Al_5 as well as the Fe//Fe_2Al_5 interface structure. In the last section, we discuss the results before presenting a summary and conclusions.

2 Method for Interface building

2.1 Prediction of orientation relationships

The first step in creating the interface structure is to establish an OR between the two phases in question. We modeled the interface as an atomically sharp defect-free interface between two crystals 1 (Fe) and 2 (Fe_2Al_5). To find possible ORs, a large number of possible sets of crystallographic directions were explored. The possible interface planes in Fe are defined by all pairs of lattice vectors, $\mathbf{u}_1$ and $\mathbf{v}_1$, in Fe. Similarly, $\mathbf{u}_2$ and $\mathbf{v}_2$ define all possible interface planes of Fe_2Al_5. To obtain a periodic interface, the following relations must be fulfilled:

$$\begin{aligned} |\mathbf{u}_1| &= |\mathbf{u}_2| \\ |\mathbf{v}_1| &= |\mathbf{v}_2| \\ \gamma_1 &= \gamma_2 \end{aligned} \tag{1}$$

where $\angle\, \gamma_n = \angle(\mathbf{u}_n, \mathbf{v}_n)$, with $n = 1, 2$ for crystal 1 and 2, respectively, and it is defined as the angle between vector directions **u** and **v**. We have added a vacuum layer along the normal direction to avoid periodic interaction. For this reason, angles $\angle\, \alpha_n = \angle(\mathbf{v}_n, \mathbf{w}_n)$ and $\angle\, \beta_n = \angle(\mathbf{u}_n, \mathbf{w}_n)$ are not relevant, as the interface structures do not need to be periodic along the normal direction to the interface.

In the general case, it is not possible to find an OR satisfying these conditions exactly. The resulting interface structure depends on how well these conditions are fulfilled using the strains along direction **u** and direction **v**:

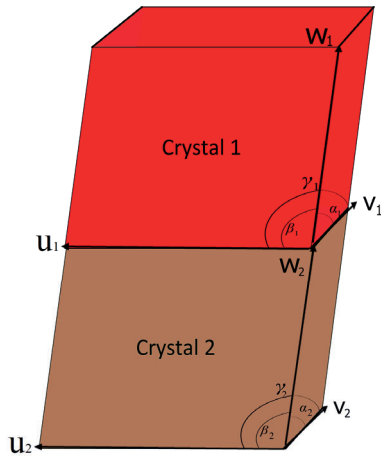

Fig. 1: A possible 3D interface model between crystal 1 and crystal 2. The crystals are slightly strained for them to match.

$$\epsilon_u = \frac{||\mathbf{u}_2| - |\mathbf{u}_1||}{|\mathbf{u}_1|} \tag{2}$$

$$\epsilon_v = \frac{||\mathbf{v}_2| - |\mathbf{v}_1||}{|\mathbf{v}_1|} \tag{3}$$

and the difference in angles γ between lattice directions;

$$\Delta\gamma = |\gamma_2 - \gamma_1| \tag{4}$$

These angles between two crystals are illustrated in Fig. 1. The two structures (red and brown) are strained to match the angles to form a coherent interface structure ($\gamma_{1,2} \neq 90°$).

In general an interface structure has 9 degrees of freedom (3 degrees related to the possible OR, 2 degrees for the possible interface plane, 2 for lateral translation along the interface plane and 2 degrees for position of where the interface cuts each phase). Ideally, $\Delta\gamma = 0$, but when these conditions are not fulfilled, the minimum difference between angles (min $\Delta\gamma$) can be considered.

To construct good interface models, ORs are obtained by looping through all possible combinations of orientations up to a given crystal lattice vector length and testing them against the criteria listed above. We can thereby choose an interface

structure with a low misfit and a corresponding supercell structure with low enough number of atoms so that DFT calculations are feasible.

By using the methodology presented above, we predicted the possible interface structures between Fe_2Al_5 and Fe. The DFT-relaxed bulk structure of Fe_2Al_5 was used as input for finding the interface structures. To reduce computational cost, we only considered the interface structure where the number of atoms and misfit is relatively small (see Appendix Table 4). We finally selected the interface structure that has a low misfit, the least number of atoms and which contains the experimentally reported $Fe_2Al_5(0\bar{2}0)$ plane [19], which turned out to be $Fe_2Al_5(0\bar{2}0)$//Fe$(\bar{1}21)$. For these reasons it was assumed to be a good representation of the Fe_2Al_5 // Fe interface.

2.2 Determination of bulk Fe_2Al_5

Fe_2Al_5 has an orthorhombic unit cell which contains single crystallographic Fe sites (four per cell) and three Al sites [20]. The Al1 site, which contains eight atoms per cell, is fully occupied, while Al2 and Al3 are too close to be occupied simultaneously, resulting in a partial occupancy factor of 1/6 each [21]. We performed ground state energy calculations to find the stable crystal structure and used this structure further for bulk and interfacial calculations. Results of the bulk strength calculations of Fe_2Al_5 have been reported in previous work [22].

2.3 $Fe_2Al_5(0\bar{2}0)$//Fe$(\bar{1}21)$ interface

The atomic structure of Fe_2Al_5//Fe was constructed using the procedure described above (Sec. 2.1). To ensure the bulk-like interior of atomic interfaces, six layers of Fe and Fe_2Al_5 were tested. It is worth mentioning that Fe_2Al_5 can be terminated either by Al or Fe at the interface. Both terminations were tested for the interfaces shown in Fig. 2. To avoid periodic interactions, a vacuum layer of >10 Å was added along the normal direction to remove the effect of the two artificial interfaces. Fig. 2 shows the tensile fracture procedure of DFT-relaxed interface structures with both terminations. For the strength calculations, DFT-relaxed interface structures were used as an input for virtual tensile and shear test calculations.

3 Calculation Methods and Model

3.1 First principles calculations

The first-principle calculations based on DFT were performed using the Vienna ab-initio Simulation Package (VASP) [23]. The exchange-correlation energy was evaluated using the Generalized Gradient Approximation (GGA) by Perdew, Burke and Ernzerhof (PBE) [24] and with the Projector Augmented Wave (PAW) [25]

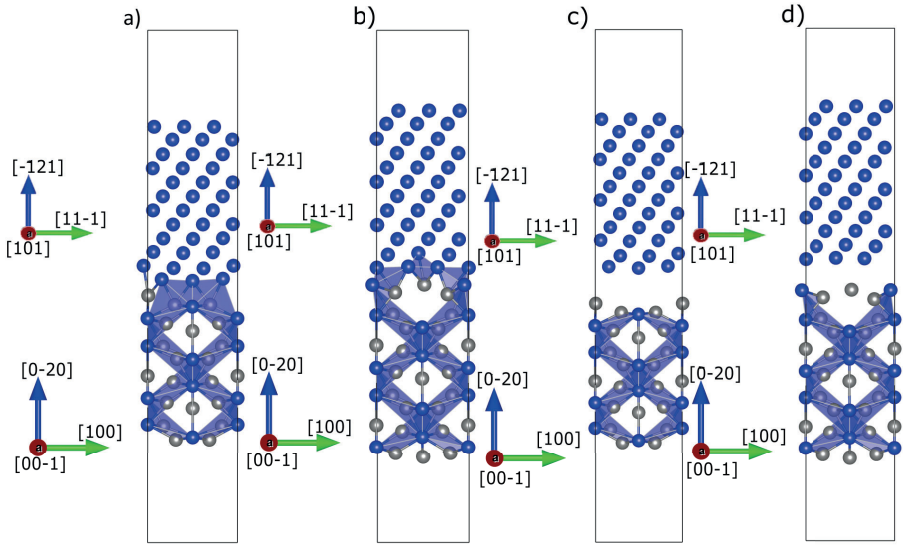

Fig. 2: Virtual tensile tests for the Fe_2Al_5(020) // Fe (-121) interface structure: (a, b) shows the Fe and Al-terminated relaxed equilibrium structures, (c) Fe-terminated virtual tensile test, and (d) Al-terminated virtual tensile test.

method. Automatic k-points were generated by using the method proposed by Monkhorst-Pack to characterize energy integration as the first irreducible Brillouin zone [26] with a maximal k-point distance of 0.18 $Å^{-1}$. In our calculations, a maximum energy cutoff value of 450 eV was used for the plane wave expansion in reciprocal space. During the optimization process, the total energy changes were set to 1×10^{-5} eV. Furthermore, the average force per atom was reduced to 0.009 eV/Å using a smearing factor of 0.2 and a first-order Meth -Fessel-Paxton for the smearing of the partial occupation. Due to the magnetic behavior of Fe atoms, spin-polarized calculations were performed for the interface structures and bulk Fe by specifying the initial local magnetic moment of Fe.

3.2 Virtual tensile test calculations

Ab-initio virtual tensile calculations of the Fe_2Al_5//Fe interface were carried out in the framework of Rigid Grain Shift (RGS) and RGS+relaxation methodology [10, 27, 28]. In this approach, the equilibrium structure was separated along the $[0\bar{2}0]$ direction. For each displacement, two kinds of calculations were performed: (1) RGS, without any atomic relaxation, and (2) RGS followed by atomic relaxation with a fixed supercell. We did not consider Poisson's effect in this study [28].

In the RGS approach, the interface structure was modeled by rigidly separating

the two blocks of material and performing static calculations without any relaxation, while in the RGS+relaxation method, atoms were allowed to relax. These calculations provide an energy-displacement curve, which can be fitted using the universal binding energy relationship (UBER) [29–31]. Rose et al [32] observed that the separation energy of metals has a universal form;

$$E_b(d) = |E_b^e| \cdot g(a) \tag{5}$$

where E_b^e is the separation energy of the equilibrium structure, d is the displacement defined with respect to the equilibrium structure and a is the re-scaled displacement, given by $a = d/l$, where l is a characteristic length which can be approximated by the curvature of the energy-displacement curve at its minimum. Eq. (6) is used as a starting point for the fitting procedure,

$$l = \sqrt{\frac{|E_b^e|}{E_b''(0)}} \tag{6}$$

If the functional form $g(a)$ is known, we can determine the theoretical strength and critical displacement of any material from the parameters E_b^e, and E_b''. This virtual tensile testing provides separation energy versus tensile displacement. The results obtained from these calculations can then be fitted to the UBER curve using Eq. (5) and (7). As Rose et al. observed, the metallic bonding-energy curve can be approximately scaled into the universal binding energy relation for the following cases: (i) metallic or bimetallic adhesion (ii) chemisorption on a metal surface, and (iii) cohesion of bulk metals [32]. Although UBER describes well separation energy versus displacement for un-relaxed metal surfaces, it is unable to describe the behavior of tightly bound intermetallics [33]. To find a good fit which captures the behavior of the separation energy versus displacement curve, we generalized it by including two polynomials [34, 35]:

$$g(a) = -(1 + a + P(a))e^{-a-Q(a)} \tag{7}$$

where a is the rescaled displacement and P and Q are polynomials of order two or larger with positive (leading) coefficients. This expression for $g(a)$ ensures that $g(0) = -1$, $g(a \to \infty) = 0$ and $g'(0) = 0$. The first-order terms are excluded from P and Q since they are related to each other as well as to the characteristic length.

To ensure that the fitting behaves well, one should only include odd-order terms in the polynomials P and Q and make sure that all coefficients are zero or positive.

By differentiating the fitted energy-displacement curve, the theoretical tensile strength of the atomic structures can be evaluated [29];

$$\sigma_{th} = \frac{\partial E_b}{\partial d} \tag{8}$$

The theoretical strength σ_{th} at its maximum value is defined as the Ultimate Tensile Strength (σ_{UTS}). The value of d at σ_{UTS} is defined as the critical length d_c.

4 Results and Discussion

4.1 Bulk strength

To compare the bulk and interface structures, we also calculated the tensile properties of $Fe_2Al_5(0\bar{2}0)$ using the rigid shift (RGS) and RGS+relaxation methodology as explained in Sec. 3.1. We studied the virtual tensile strength of both the Al- and the Fe-terminated Fe_2Al_5 structures as shown in Fig. 3.

Fig. 4 (a) and (b) show the separation energy versus tensile displacement curve for Al and Fe-terminated fracture using the RGS and RGS+relaxation methodologies. In the stable configuration of the Fe_2Al_5 phase, the Fe-Al bond distance is 2.50 Å and the Fe-Fe bond distance is 2.96 Å. During the virtual tensile testing, this bond distance at the cutting plane is stretched further until the bulk structure fractures and separates into two free surfaces. Fig. 3 (b) and (c) show the procedure for introducing a crack with Al and Fe-terminations. Table 1 lists the work of separation (W_{sep}) and the work of adhesion (W_{ad}). The former is defined as the work needed to separate a bulk phase without atomic relaxation, and the latter is the energy needed to separate a bulk interface into two relaxed surfaces [36].

The binding energy increases with tensile displacement. RGS without atomic relaxation produces a steeper curve which was fitted using Eq. (5) and (7). During tensile displacement, the separation energy increases sharply until it stabilizes at larger displacements ($> \sim$5 Å).

Table 1 lists the calculated σ_{UTS}. Fig. 5 shows the stress-strain curves for Fe_2Al_5 along with bulk strengths for the RGS and RGS+relaxation methodologies. As can be seen, with increasing tensile strain, the tensile stress increases until its maximum value (σ_{UTS}). One can note that σ_{UTS} calculated with the RGS+relaxation methodology is lower than that for the RGS methodology. For comparisons, we also reported the strength of the bulk Fe (111) plane. The Al-terminated Fe_2Al_5 bulk phase shows higher strength (20.09 GPa for RGS and 15.48 GPa for RGS+relax ation) as compared to the Fe-terminated structure (17.72 GPa for RGS and 13.28 GPa for RGS+relaxation). Moreover, bulk Fe atoms showed higher values of W_{sep}

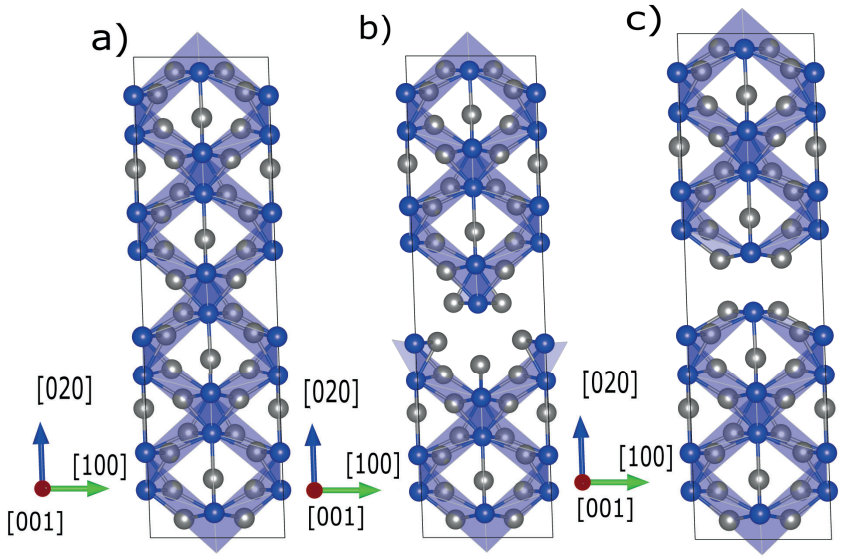

Fig. 3: Virtual tensile tests for the bulk Fe_2Al_5(020) structure: (a) relaxed equilibrium structure (b) Al-terminated virtual tensile test, and (c) Fe-terminated virtual tensile test.

Table 1: Calculated virtual tensile strength, W_{sep} and W_{ad} of bulk Fe_2Al_5 and bcc Fe.

Structure	σ_{UTS} (RGS) (GPa)	σ_{UTS} (RGS+relaxation) (GPa)	W_{sep} (J/m^2)	W_{ad} (J/m^2)
Al-terminated Fe_2Al_5	20.09	15.48	6.16	5.81
Fe-terminated Fe_2Al_5	17.72	13.28	5.54	5.16
Fe	27.7^a <111> $28.5^{b,c}$ <111>	-	6.09 <121>	-

^{a} [37] ^{b} [38] ^{c} [39]

and σ_{UTS}, which signify the higher strength for bulk Fe than the Fe_2Al_5 phase. A lower strength of the Fe-terminated bulk Fe_2Al_5 indicates a weaker bonding between Fe-Fe atoms which will be discussed in sub-section 4.3. Besides, the long bonding distance between Fe-Fe also contributes to the weakening of the bond.

4.2 Interface strength

Energy-displacement curves

Energy-displacement curves are shown in Fig. 6 for Al-terminated and Fe-terminated interface structures using the above mentioned fitting technique. Fig. 6 (a) and (c) show the energy-displacement curve for RGS and Fig. 6 (b) and (d) show the same curves for the RGS+relaxation methodology. A steep and continuous curve is obtained for the RGS methodology without any atomic relaxations, which can

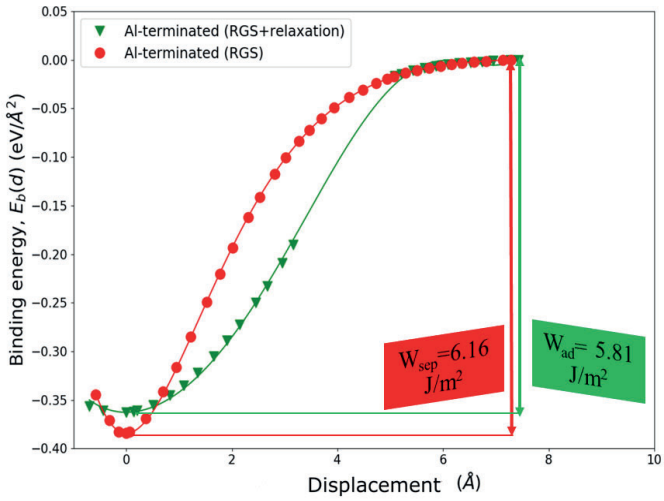

(a) Al-terminated bulk Fe_2Al_5.

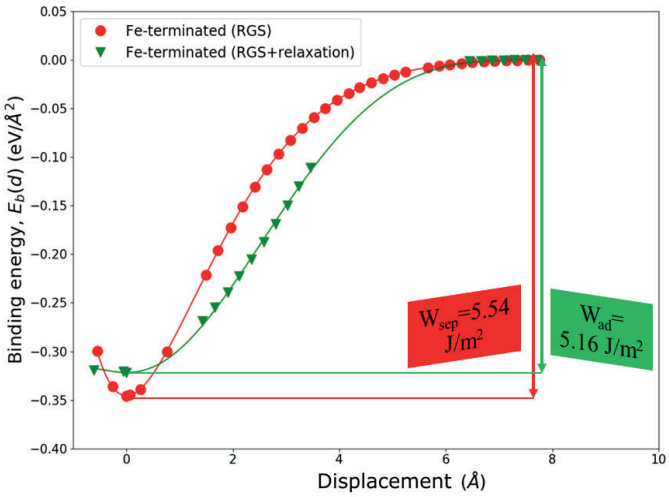

(b) Fe-terminated bulk Fe_2Al_5.

Fig. 4: Separation energy versus displacement for virtual tensile tests of the bulk Fe_2Al_5(020) structure: (a) Al-terminated virtual tensile test, and (b) Fe-terminated virtual tensile test.

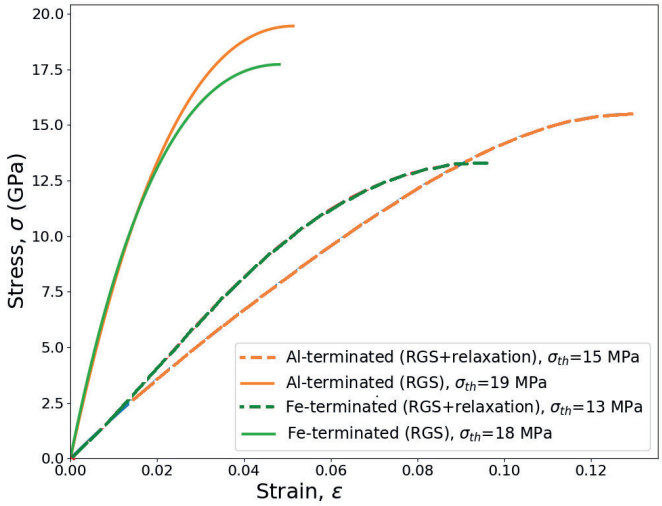

Fig. 5: Virtual tensile tests stress-strain curve for the bulk Fe_2Al_5(020) structure with both Al and Fe-terminations calculated with the RGS and RGS+relaxation methods.

be fitted well by using Eq. (5). As can be seen from Fig. 6(b) and (d), with the increase in tensile displacement, the energy required to fracture the interface structure decreases until the structure separates into two surfaces at larger displacements (>3 Å). The separation length at that point is defined as the final fracture length (d_f). Even though there is no unique way of determining d_f, we define it to be at the point where the binding energy curve reaches -0.003 eV/Å^2 [35].

The minimum value of the binding energy gives -$E_b(0) = W_{sep}$ for RGS and -$E_b(0) = W_{ad}$ for the RGS+relaxation methodology. Table 2 lists the W_{sep} and W_{ad} values for the Fe_2Al_5//Fe interface. As given in Table 2, the Al-terminated interface shows higher W_{sep} (4.45 J/m^2) as compared to the Fe-terminated interface (3.82 J/m^2). Lazar [30] postulated the rough approximation that W_{sep}= 1.06W_{ad} by linear fitting of DFT results of RGS and RGS+relaxation methodologies for different compounds and materials. This fits perfectly for the Al-terminated interface but less so for the Fe-terminated interface.

An optimal fit for the relaxed surfaces is shown in Fig. 6 (b) and (d). For the relaxed-type virtual tensile tests, crack opening is initiated by separating two blocks by introducing vacuum and subsequently allowing atoms to relax while keeping the plane area fixed. The initial crack introduced during RGS can potentially be healed by atomic relaxation if the separation between two blocks is smaller than

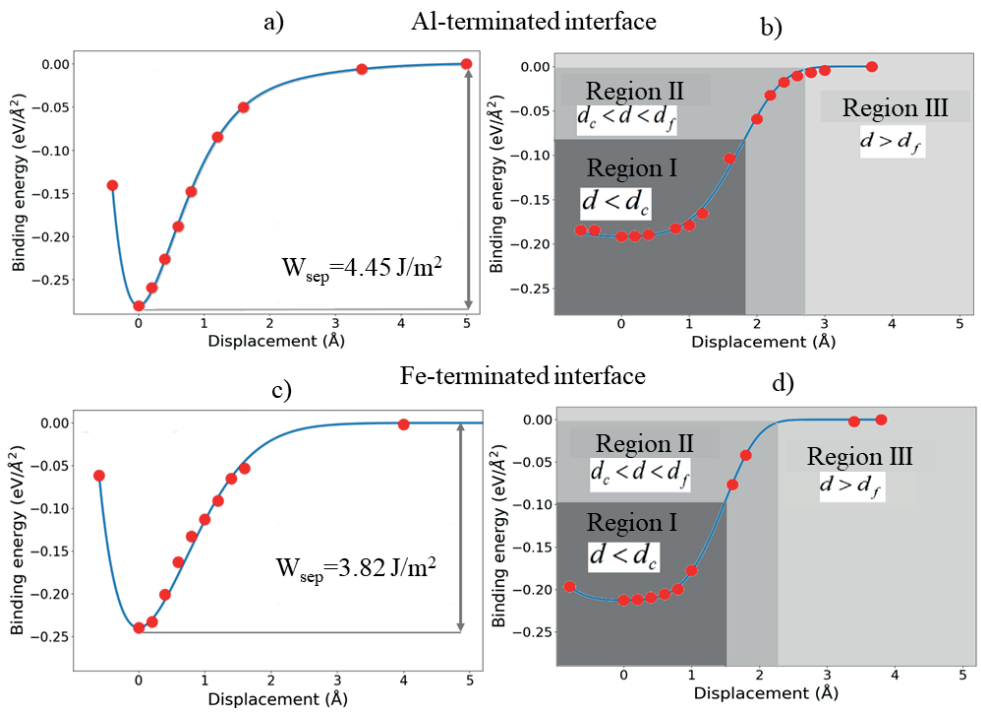

Fig. 6: Energy-displacement curves resulting from virtual tensile tests for the Fe_2Al_5(020)//Fe interface structure with both Al and Fe terminations, (a) and (c) show the virtual tensile test results for the RGS methodology and (b) and (d) for the RGS+relaxation methodology. Red points show DFT calculation results and the blue solid line is the fitted curve.

the critical length (d_c) [29]. In Fig. 6 (b) and (d), d_c is located at the border of Region I ($d < d_c$). Table 2 lists the critical (d_c) and fracture lengths (d_f) for the two relevant interface structures.

Region II is defined for separation $d_c < d < d_f$. In this region, the structure is neither separated nor being able to heal by elastic relaxations, which is why it is defined as the instability region. The range of this instability region is determined by taking the difference between d_f and d_c. The width of Region II is related to the brittleness/ductility of the interface structure [30]. For the Al-terminated interface structure, the length of the instability region is approximated to be 0.84 Å, while for the Fe-terminated interface, it is 0.79 Å. The shorter-range of instability region for the Fe-terminated interface indicates a more brittle fracture than that of the Al-terminated interface.

At longer separation distances ($d > d_f$), the interface structures are completely separated into two relaxed bulk surfaces. This region is defined as Region III in light grey color (Fig. 6 (b) and (d)). In this region, there is no interaction at the interface, and relaxation of the atomic position relaxes the bulk surfaces into stable configurations. For this reason, the binding energy versus separation curve stabilizes, and no further increase in binding energy can be seen.

Tensile strength

Table 2 lists σ_{UTS} of Fe_2Al_5 // Fe interface structures for both terminations. Since RGS+relaxation calculations were performed with atomic relaxations, σ_{UTS} calculated from this approach provides more realistic values than those for the RGS calculations. Based on the RGS+relaxations virtual tensile tests, the Al-terminated interface shows lower strength (23.88 GPa) as compared to the Fe-terminated interface (31.48 GPa). Overall, the interface structures show higher σ_{UTS} values than bulk Fe_2Al_5. The Fe-terminated interface showed the highest strength (31.48 GPa) and Fe-terminated bulk Fe_2Al_5 the lowest strength (17.72 GPa).

In order to elucidate the bonding characteristics of the interfacial and bulk atoms, total charge density isosurfaces were drawn at 0.03 eV/Å^3 for all surfaces as shown in Fig. 7. A high charge density cloud (labeled as B in Fig. 7(b)) can be seen for the Fe-terminated interface as compared to the Al-terminated interface (labeled as A in Fig. 7(a)). This high charge density at B indicates stronger bonding between interfacial Fe-Fe atoms at the Fe-terminated interface, which explains the higher σ_{UTS} for this interface as compared to the Al-terminated interface.

For the bulk Fe_2Al_5 structure as shown in Fig. 7(c), Fe-Fe bonding (labeled as C) was found to be weaker than the Al-Fe bonding (labeled as D). This observation is consistent with the lower σ_{UTS} for the Fe-terminated bulk structure. Generally,

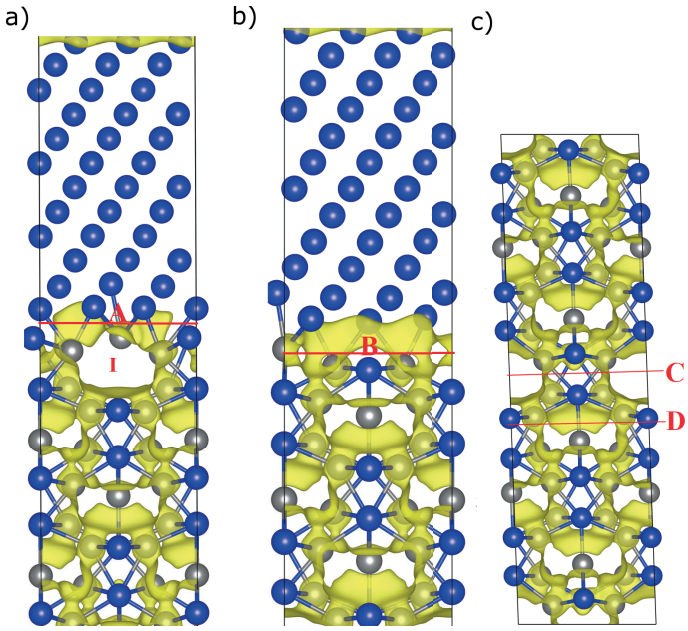

Fig. 7: Calculated total charge density isosurfaces for (a) Al-terminated interface, (b) Fe-terminated interface and (c) bulk Fe_2Al_5 drawn at 0.03 eV/Å^3. A, B, C, and D define the cutting planes for virtual tensile testing and I indicates the weak fracture plane for the Al-terminated interface.

Fe-Al atoms are found to have higher charge density regions in the interfaces and the bulk structures. However, in the Al-terminated interface, the Al atom moves towards the Fe atoms and develops a bond at the interface by compromising the bonding strength on the first layer of the Fe_2Al_5 side, labeled as I in Fig. 7(a). This fracture plane can be a weak link of the overall Al-terminated interface structure.

Ideal shear strength

To calculate the ideal shear strength a series of incremental shear strains were applied to the Fe_2Al_5//Fe supercell. We moved the Fe surface along the <001> and <001> shear direction. For these calculations, six layers of Fe were sheared

Table 2: Calculated virtual tensile strengths, W_{sep} and W_{ad} values of the Fe//Fe_2Al_5 interface structure.

Structure	σ_{UTS} (RGS) (GPa)	d_c (Å)	d_f (Å)	σ_{UTS} (RGS+relaxation) (GPa)	W_{sep} (J/m^2)	W_{ad} (J/m^2)
Al-terminated interface	29.56	1.80	2.64	23.88	4.45	3.04
Fe-terminated interface	24.50	1.51	2.30	31.48	3.82	3.36

along the defined shear directions with respect to the Fe_2Al_5 atoms at the interface. Atoms were allowed to relax along the normal direction to the interface to remove any strain along that direction. The shear energies are defined in terms of a Fourier series;

$$E_s(d) = E_0 + \sum_{n=1}^{\infty}[A_n cos(k_n d) + B_n sin(k_n d)] \tag{9}$$

where $E_s(d)$ and E_0 are the energy of the displaced and unsheared structure, respectively, d is the shear displacement, and k_n=$\frac{2\pi n}{\lambda}$, where λ is the periodicity along the shear direction. Appendix Table 5 and 6 gives the Fourier series coefficient values and the value of λ for both interface structures.

The shear stress is given by

$$\gamma_s = \frac{1}{A}\frac{\partial E_s}{\partial d} \tag{10}$$

where A is the interface area. The maximum value in the resulting shear-displacement curve corresponds to the ideal shear strength, which is defined as the interface resistance to the shear displacement after which it starts to deform.

Fig. 8 shows the stress-displacement curve for the shear stress as a function of shear displacement for both Al- and Fe-terminations. Initially, stress increases with the increase in the shear displacement until it reaches a maximum value for both cases, which is taken as the ideal shear strength of the interface structure. Table 3 summarizes the ideal shear strength of the Fe_2Al_5//Fe interface structure for all cases discussed in this work. Results are quite different for both interface terminations. The Fe-terminated interface shows low shear strength (0.97 GPa) along <001> and larger shear strength along the <100> (4.74 GPa), while the Al-terminated interface shows high shear strength (2.51 GPa) along <100> direction and a slightly lower shear strength along <001> (3.97 GPa). The Al-terminated structure shows higher shear strength than the Fe-terminated interface structure. These calculations, therefore, indicate that the Fe-terminated $< 001 >$ interface is more prone to shear than the Al-terminated interface.

Comparing shear strength with tensile strength indicates that the Al-terminated interface shows higher tensile and shear strength than the Fe-terminated interface. From Table 2 and 3, it can be seen that shear instability can occur earlier than normal decohesion. This is consistent with the experimental observations of the Al-Fe welded system [40]. The shear strength calculated in this study for loading parallel to the interface is lower than the perpendicular loading direction (σ_{UTS}).

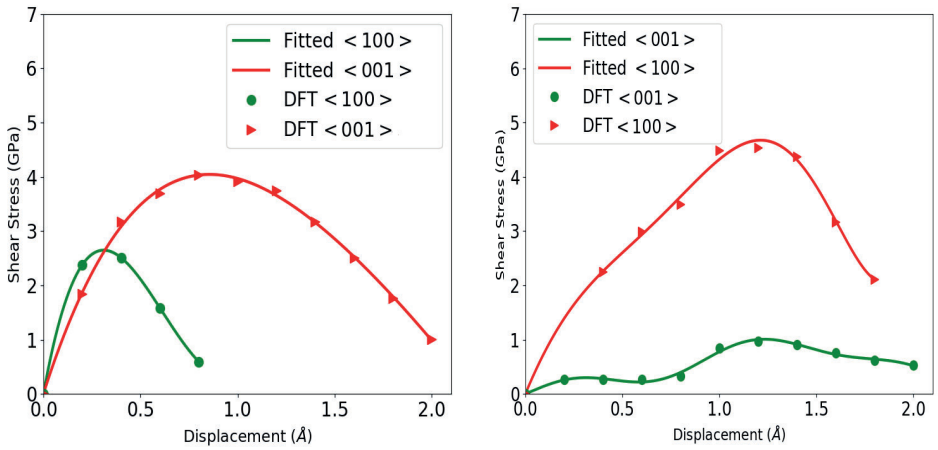

(a) Al-terminated **(b)** Fe-terminated

Fig. 8: Fitted shear stress-displacement curve of the Fe_2Al_5//Fe interface for (a) Al- and (b) Fe-terminations during the shear strength simulations as a function of shear displacement along the <001> and <100> shear directions.

Table 3: Calculated Ideal shear strength values of Fe_2Al_5 $(0\bar{2}0)$//Fe$(\bar{1}21)$ interface, directions are defined with respect to Fe_2Al_5.

Interface	<001>(GPa)	<100>(GPa)
Fe-termination	0.97	4.74
Al-termination	3.97	2.51

The same trend has been observed experimentally and theoretically in the literature [16, 40, 41].

5 Discussion

Before discussing the implications of these results, some limitations are worth to be mentioned. These simulations have performed without considering dislocations, micro-voids, and other effects occurring at larger length scales, that will influence the strength subsequently. Hence, the calculated strengths are overestimated. Still, these calculations provide important insights about the crack formation mechanism of the interface structure at the atomic scale. The role of crystal defects on the mechanical properties is proposed to be a subject of future studies.

In this work we have studied the effect Fe_2Al_5 intermetallics have on the strength of aluminium-steel joints. It is a very difficult task to identify the fractured layer of

aluminum and steel joint by experiments. For this reason, to predict the weak zone of the Fe_2Al_5 // Fe interface structure, two zones were studied: (i) bulk Fe_2Al_5 and (ii) Fe_2Al_5 //Fe interface. Based on bulk and interface calculations, the interface between Fe_2Al_5 // Fe showed higher strength as compared to bulk Fe_2Al_5 and smaller than bulk Fe [37]. Virtual tensile testing, therefore, indicates that bulk Fe_2Al_5 is more prone to induce fracture than the interface and bulk Fe side. Mechanical strength inferred from the virtual tensile calculations indicates that fracture is most likely to be initiated from the Fe-terminated side of the bulk Fe_2Al_5 due to weak bonding between Fe-Fe atoms. Shear strength is seen to be lower than the tensile strength, which is also consistent with the experimental observation of Fe_2Al_5 [42].

These results have a particular significance for the welding of aluminum and steel joints for different welding methodologies, where the presence of an Fe_2Al_5 intermetallic layer has been reported along the steel side. However, the defects at the IMC layers also play a significant role in deteriorating the joint strength and have to be included in the calculations to give more reliable predictions for real systems.

6 Summary and conclusions

To summarize, we have performed DFT calculations of tensile and shear strength of the Fe_2Al_5//Fe interface. The interface structure with the lowest lattice misfit and number of atoms was selected for the DFT calculations of this work. Virtual tensile tests were performed with the rigid grain shift (RGS) methodology without atomic relaxations and RGS+relaxation methodology with atomic relaxations. Polynomial terms were introduced into the UBER to find a reasonable fit for the tensile stresses. Based on RGS calculations, the Al-terminated interface showed higher strength than bulk Fe_2Al_5 and the Fe-terminated interface structure. During the relaxation of atomic positions in the RGS+relaxation methodology, the tensile strength decreased for all structures except for the Fe-terminated interface. Moreover, the charge densities indicated a weaker bonding between Fe-Fe atoms in the bulk Fe_2Al_5 structure, which contributed to a lower tensile strength. We also analyzed the shear strength for the interface along <001> and <100> directions. We found that [001] has lower shear strength for the Fe-terminated interface while it showed higher strength for the Al-terminated interface along this direction.

Overall the Fe bulk side was found to be the strongest zone of the Fe_2Al_5//Fe interface structure followed by the interface and bulk Fe_2Al_5. Based on these calculations, it can be predicted that during a mechanical failure, fracture is most likely to be initiated at the bulk Fe_2Al_5 side. This study can potentially be the starting point for further investigations of the effects of crystal defects and temperature on the joint strength of aluminum-steel.

7 Acknowledgements

The work reported in this paper was based on activities within the centre for research-based innovation SFI Manufacturing in Norway and is partially funded by the Research Council of Norway under contract number 237900. UNINETT Sigma2 AS (The Norwegian Metacenter for High Performance Computing) provided computational resources through Project NN9466K and NN9158K.

8 Appendix

Appendix Table 4 lists the predicted ORs between Fe and Fe_2Al_5 by the face-to-face matching technique. In Table 4, m_1, m_2 and m_3 are the components of a linear combination of vector $\mathbf{u}_1$ of crystal 1, similarly n_1, n_2 and n_3 are defined for crystal 2, and is given as;

$$\begin{aligned} \mathbf{u}_1 &= m_1\mathbf{a}_1 + m_2\mathbf{b}_1 + m_3\mathbf{c}_1 \\ \mathbf{u}_2 &= n_1\mathbf{a}_2 + n_2\mathbf{b}_2 + n_3\mathbf{c}_2 \end{aligned} \tag{11}$$

normally m_1, m_2, m_3 and n_1, n_2, n_3 are integers, but due to sub-lattice translations in the conventional cell, fractions are also possible.

Table 5 and 6 lists the Fourier series coefficient values for the shear strength calculations for both interface structures.

Table 4: Some of the predicted ORs between Fe_2Al_5 and Fe atoms. m_1, m_2 and m_3 are the direction vectors for Fe_2Al_5 phase and n_1, n_2 and n_3 for Fe atoms. length and strain (%) are the length of supercell and misfit percentage (as defined in Eq. (2) and (3)) of the interface structures respectively.

#	d	m_1	m_2	m_3	length (Å)	$\angle\gamma$	n_1	n_2	n_3	length (Å)	$\angle\gamma$	strain (%)	# atoms
1	**u**	0	0	-1	4.10	90°	1	0	1	4.06	90°	0.89	64
	v	1	0	0	7.40	90°	1.5	1.5	-1.5	7.46	90°	0.79	
	w	0	-2	0	12.88	90°	-2	4	2	14.06	90°		
	h	0	-2	0			-1	2	1			0.56	
2	**u**	0	0	0	4.10	119.9°	1	0	1	4.06	119.8°	0.89	130
	v	2	0	0	14.80	90°	3.5	1.5	-3.5	14.84	90°	0.33	
	w	-1	-2	0	14.86	90°	-3	4	3	16.73	90°		
	h	0	-1	0			-3	14	3			0.52	
3	**u**	0	0	1	4.10	119.9°	1	0	1	4.06	119.8°	0.89	130
	v	1	2	0	14.86	90°	3.5	1.5	-3.5	14.84	90°	09	
	w	-2	0	0	14.80	90°	-3	4	3	16.73	90°		
	h	-2	1	0			-3	14	3			0.56	
4	**u**	0	0	1	4.10	119.9°	1	0	1	4.06	119.5°	0.89	116
	v	1	2	0	14.86	90°	3	3	-3	14.91	90°	0.38	
	w	-2	0	0	14.80	90°	-3	2	3	13.46	90°		
	h	-2	1	0			-1	2	1			0.63	
5	**u**	0	0	1	4.10	101.1°	1	0	1	4.06	101.4°	0.89	98
	v	0.5	1.5	0	10.35	90°	0.5	3.5	-0.5	10.25	90°	0.96	
	w	-2.5	0.5	0	18.77	90°	-3	0	3	12.18	90°		
	h	-3	1	0			-7	2	7			0.71	
6	**u**	0	0	1	4.10	101.1°	1	0	1	4.06	101.4°	0.89	98
	v	0.5	1.5	0	10.35	90°	2.5	0.5	-2.5	10.25	90°	0.96	
	w	-2.5	0.5	0	18.77	90°	-1	4	1	12.18	90°		
	h	-3	1	0			-1	10	1			0.71	
7	**u**	0	0	1	4.10	110°	1	0	1	4.06	110.3°	0.89	165
	v	1	2	0	14.86	90°	1	5.0	-1	14.91	90°	0.38	
	w	-2.5	0.5	0	18.77	90°	-4.5	-0.5	4.5	18.32	90°		
	h	-2	1	0			-5	2	5			0.60	
8	**u**	0	0	1	4.10	97.9°	1	0	1	4.06	98.0°	0.89	41
	v	0.5	0.5	0	4.90	90°	1	1	-1	4.97	90°	1.35	
	w	-1.5	1.5	0	14.71	90°	-2	3	2	11.83	90°		
	h	-1	1	0			-1	2	1			0.80	
9	**u**	0	0	1	4.10	115.8°	1	0	-1	4.06	115.2°	0.89	56
	v	1	0	-1	8.46	90°	-1.5	2.5	0.5	8.49	90°	0.40	
	w	-1	2	0	14.86	119.0°	3	-1	3	12.51	118.6°		
	h	0	1	0			5	2	5			0.87	
10	**u**	0	0	1	4.10	105.2°	1	0	1	4.06	105.9°	0.89	98
	v	1.5	-0.5	-1	12.26	90°	-1	4	-1	12.18	90°	0.67	
	w	0	2	0	12.88	109.5°	3.5	-1.5	3.5	14.84	109.5°		
	h	1	3	0			-1	0	1			0.84	
11	**u**	0	1	2	10.42	119.2°	3	0	-2	10.35	119.6°	0.68	192
	v	1	-1	1	10.63	92°	1	-3	2	10.74	91.8°	11	
	w	0.5	1.5	-2	13.20	94.1°	-2.5	-0.5	-3.5	12.43	94.3°		
	h	3	2	-1			-6	-8	-9				
12	**u**	1	0	0	7.40	95.8°	2.5	0.5	0.5	7.46	95.9°	0.79	215
	v	-0.5	1.5	2	13.19	90°	-0.5	0.5	-4.5	137	90°	0.92	
	w	0	-2	3	17.81	106.3°	-1	4	1	12.18	105.9°		
	h	0	-4	3			-5	22	3			0.69	
13	**u**	0	1	-2	10.42	109.4°	3	2-0	0	10.35	109.5°	0.71	230
	v	0.5	-1.5	-1	11.13	90°	-1.5	0-5	-3.5	112	90°	0.94	
	w	-2	0	0	19.38	104.3°	-2	3-0	3	13.46	104.6°		
	h	-8	-2	-1			-14	21	9			0.65	

Table 5: The fitting Fourier series coefficient values for the shear strength calculation of Al-terminated Fe_2Al_5//Fe interface.

Polynomial terms	A_0	A_1	A_2	A_3	B_1	B_2	B_3	λ
<100>	-1107.76	110.59	1864.90	-646.56	271.21	11115	-803.98	77.85
<001>	-1107.76	110.59	1864.90	-646.56	271.21	11115	-803.98	77.85

Table 6: The fitting Fourier series coefficient values for the shear strength calculation of Fe-terminated Fe_2Al_5//Fe interface.

Polynomial terms	A_0	A_1	A_2	A_3	A_4	A_5	B_1	B_2	B_3	B_4	B_5	λ
<100>	1660.13	-988.84	-3113.83	-1627.44	1624.54	-357.08	-299.39	1794.44	-4305.2	3842.35	-1144.45	106.08
<001>	0.415	-0.469	0.058	-0.0014	-	-	0.052	0.0699	0.0153	-	-	8.23

References

[1] A. Hotař, M. Palm, P. Kratochvíl, V. Vodičková, S. Daniš, High-temperature oxidation behaviour of Zr alloyed Fe_3Al-type iron aluminide, Corrosion Science 63 (2012) 71–81 (2012).

[2] B. L. Silva, A. Garcia, J. E. Spinelli, The effects of microstructure and intermetallic phases of directionally solidified Al-Fe alloys on microhardness, Materials Letters 89 (2012) 291–295 (2012).

[3] T. Sakiyama, G. Murayama, Y. Naito, K. Saita, Y. M. H. Oikawa, T. Nose, Dissimilar metal joining technologies for steel sheet and aluminum alloy sheet in auto body, Nippon Steel & Sumitomo Metal Corp., Tokyo, Nippon Steel Technical Report 103 (2013) 91–98 (2013).

[4] T. Ogura, Y. Saito, T. Nishida, H. Nishida, T. Yoshida, N. Omichi, M. Fujimoto, A. Hirose, Partitioning evaluation of mechanical properties and the interfacial microstructure in a friction stir welded aluminum alloy/stainless steel lap joint, Scripta Materialia 66 (8) (2012) 531–534 (2012).

[5] H. Das, S. Basak, G. Das, T. K. Pal, Influence of energy induced from processing parameters on the mechanical properties of friction stir welded lap joint of aluminum to coated steel sheet, The International Journal of Advanced Manufacturing Technology (2013) 1–9 (2013).

[6] S. Imaizumi, Welding of aluminium to dissimilar metals, Welding international 10 (8) (1996) 593–604 (1996).

[7] S. Yang, J. Zhang, J. Lian, Y. Lei, Welding of aluminum alloy to zinc coated steel by cold metal transfer, Materials & Design 49 (2013) 602–612 (2013).

[8] S. Niu, S. Chen, H. Dong, D. Zhao, X. Zhang, X. Guo, G. Wang, Microstructure and properties of lap joint between aluminum alloy and galvanized steel by CMT, Journal of Materials Engineering and Performance 25 (5) (2016) 1839–1847 (2016).

[9] Y. Shi, J. Li, G. Zhang, J. Huang, Y. Gu, Corrosion behavior of aluminum-steel weld-brazing joint, Journal of Materials Engineering and Performance 25 (5) (2016) 1916–1923 (2016).

[10] G. Zhang, M. Chen, Y. Shi, J. Huang, F. Yang, Analysis and modeling of the growth of intermetallic compounds in aluminum-steel joints, RSC Advances 7 (60) (2017) 37797–37805 (2017).

[11] S. Lan, X. Liu, J. Ni, Microstructural evolution during friction stir welding of dissimilar aluminum alloy to advanced high-strength steel, The International Journal of Advanced Manufacturing Technology 82 (9-12) (2016) 2183–2193 (2016).

[12] G. Sorger, H. Wang, P. Vilaça, T. G. Santos, FSW of aluminum AA5754 to steel DX54 with innovative overlap joint, Welding in the World 61 (2) (2017) 257–268 (2017).

[13] K.-K. Wang, L. Chang, D. Gan, H.-P. Wang, Heteroepitaxial growth of Fe_2Al_5 inhibition layer in hot-dip galvanizing of an interstitial-free steel, Thin Solid Films 518 (8) (2010) 1935–1942 (2010).

[14] A. Bouayad, C. Gerometta, A. Belkebir, A. Ambari, Kinetic interactions between solid iron and molten aluminium, Materials Science and Engineering: A 363 (1) (2003) 53–61 (2003).

[15] D. Naoi, M. Kajihara, Growth behavior of Fe_2Al_5 during reactive diffusion between Fe and Al at solid-state temperatures, Materials Science and Engineering: A 459 (1) (2007) 375–382 (2007).

[16] Y. Chen, A. Gholinia, P. Prangnell, Interface structure and bonding in abrasion circle friction stir spot welding: a novel approach for rapid welding aluminium alloy to steel automotive sheet, Materials Chemistry and Physics 134 (1) (2012) 459–463 (2012).

[17] W.-J. Cheng, C.-J. Wang, Study of microstructure and phase evolution of hot-dipped aluminide mild steel during high-temperature diffusion using electron backscatter diffraction, Applied Surface Science 257 (10) (2011) 4663–4668 (2011).

[18] L. Agudo, D. Eyidi, C. H. Schmaranzer, E. Arenholz, N. Jank, J. Bruckner, A. R. Pyzalla, Intermetallic Fe_xAl_y-phases in a Steel/Al-alloy fusion weld, Journal of Materials Science 42 (12) (2007) 4205–4214 (2007).

[19] L. Liu, L. Xiao, J. Feng, L. Li, S. Esmaeili, Y. Zhou, Bonding of immiscible Mg and Fe via a nanoscale Fe_2Al_5 transition layer, Scripta Materialia 65 (11) (2011) 982–985 (2011).

[20] U. Burkhardt, Y. Grin, M. Ellner, K. Peters, Structure refinement of the iron–aluminium phase with the approximate composition Fe_2Al_5, Acta Crystallographica Section B 50 (3) (1994) 313–316 (1994).

[21] Fe_2Al_5 (FeAl2.8) crystal structure: Datasheet from "pauling file multinaries edition – 2012" in springermaterials (https://materials.springer.com/isp/crystallographic/docs/sd_1201135), copyright 2016 Springer-Verlag Berlin Heidelberg & Material Phases Data System (MPDS), Switzerland & National Institute for Materials Science (NIMS), Japan.
URL https://materials.springer.com/isp/crystallographic/docs/sd_1201135

[22] M. Z. Khalid, J. Friis, P. H. Ninive, K. Marthinsen, A. Strandlie, DFT calculations based insight into bonding character and strength of Fe_2Al_5 and Fe_4Al_{13} intermetallics at Al-Fe joints, Procedia Manufacturing 15C (2018) 1407–1415 (2018).

[23] G. Kresse, J. Furthmüller, Vienna ab-initio simulation package (VASP), Vienna: Vienna University (2001).

[24] J. P. Perdew, K. Burke, M. Ernzerhof, Generalized gradient approximation made simple, Physical Review Letters 77 (18) (1996) 3865 (1996).

[25] P. E. Blöchl, Projector augmented-wave method, Physical review B 50 (24) (1994) 17953 (1994).

[26] H. J. Monkhorst, J. D. Pack, Special points for brillouin-zone integrations, Physical review B 13 (12) (1976) 5188 (1976).

[27] A. Tahir, R. Janisch, A. Hartmaier, Hydrogen embrittlement of a carbon segregated σ5 (310)[001] symmetrical tilt grain boundary in α-Fe, Materials Science and Engineering: A 612 (2014) 462–467 (2014).

[28] M. Yamaguchi, First-principles study on the grain boundary embrittlement of metals by solute segregation: Part i. iron (Fe)-solute (B, C, P, and S) systems, Metallurgical and Materials Transactions A 42 (2) (2011) 319–329 (2011).

[29] D. Zhao, O. M. Løvvik, K. Marthinsen, Y. Li, Segregation of Mg, Cu and their effects on the strength of Al $\sigma 5$ (210)[001] symmetrical tilt grain boundary, Acta Materialia 145 (2018) 235–246 (2018).

[30] P. Lazar, R. Podloucky, Cleavage fracture of a crystal: Density functional theory calculations based on a model which includes structural relaxations, Physical Review B 78 (10) (2008) 104114 (2008).

[31] R. Janisch, N. Ahmed, A. Hartmaier, Ab initio tensile tests of Al bulk crystals and grain boundaries: Universality of mechanical behavior, Physical Review B 81 (18) (2010) 184108 (2010).

[32] J. H. Rose, J. R. Smith, J. Ferrante, Universal features of bonding in metals, Physical review B 28 (4) (1983) 1835 (1983).

[33] E. A. Jarvis, R. L. Hayes, E. A. Carter, Effects of oxidation on the nanoscale mechanisms of crack formation in aluminum, ChemPhysChem 2 (1) (2001) 55–59 (2001).

[34] I. J. Jensen, J. Friis, C. D. Marioara, I. G. Ringdalen, The role of grain boundary precipitates during intergranular fracture in 6XXX series Aluminium alloys, In preparation.

[35] M. Z. Khalid, J. Friis, P. H. Ninive, K. Marthinsen, A. Strandlie, Ab-initio study of atomic structure and mechanical behaviour of Al/Fe intermetallic interfaces, Accepted in Computational Materials Science (2019).

[36] R. Yang, S. Tanaka, M. Kohyama*, First-principles study on the tensile strength and fracture of the Al-terminated stoichiometric α-Al_2O_3 (0001)/Cu (111) interface, Philosophical Magazine 85 (25) (2005) 2961–2976 (2005).

[37] M. Černỳ, J. Pokluda, Ideal tensile strength of cubic crystals under superimposed transverse biaxial stresses from first principles, Physical Review B 82 (17) (2010) 174106 (2010).

[38] S. Ogata, J. Li, N. Hirosaki, Y. Shibutani, S. Yip, Ideal shear strain of metals and ceramics, Physical Review B 70 (10) (2004) 104104 (2004).

[39] M. Černỳ, P. Řehák, Y. Umeno, J. Pokluda, Stability and strength of covalent crystals under uniaxial and triaxial loading from first principles, Journal of Physics: Condensed Matter 25 (3) (2012) 035401 (2012).

[40] P. Peyre, G. Sierra, F. Deschaux-Beaume, D. Stuart, G. Fras, Generation of aluminium-steel joints with laser-induced reactive wetting, Materials Science and Engineering: A 444 (1-2) (2007) 327–338 (2007).

[41] Y.-J. Wang, C.-Y. Wang, Influence of the alloying element re on the ideal tensile and shear strength of γ-Ni_3Al, Scripta Materialia 61 (2) (2009) 197–200 (2009).

[42] W. Qian, X.-s. Leng, T.-h. Yang, J.-c. Yan, Effects of Fe—Al intermetallic compounds on interfacial bonding of clad materials, Transactions of Nonferrous Metals Society of China 24 (1) (2014) 279–284 (2014).

Paper V

Khalid M. Z., Friis J., Ninive P. H., Marthinsen K., Strandlie A. (2019). "First-principles study of tensile and shear strength of α-AlFeSi // Fe_4Al_{13} and Fe_2Al_5 // Fe_4Al_{13} intermetallic interfaces, Aimed for Computational Materials Science.

Paper V

First-principles study of tensile and shear strength of α-AlFeSi // Fe_4Al_{13} and Fe_2Al_5 // Fe_4Al_{13} intermetallic interfaces

Khalid M. Z., Friis J., Ninive P. H., Marthinsen K., Strandlie A.

Abstract

First-principles virtual tensile and shear strength calculations were performed on the Fe_2Al_5 // Fe_4Al_{13} and α-AlFeSi // Fe_4Al_{13} interfaces. The Fast Inertial Relaxation Engine (FIRE) algorithm is found to be successful in optimizing these complex Intermetallic Compound (IMC) interface structures. To characterize the virtual tensile strength, an extended generalized Universal Binding Energy Relation (UBER) was used to fit the energy-displacement data. The virtual tensile strength was evaluated with a Rigid Grain Shift (RGS) methodology without atomic relaxations during tensile displacement and RGS+relaxation with atomic relaxations. Results for the RGS+relaxation-based approach indicates stronger tensile strength and more brittle crack formation for the Fe_2Al_5 // Fe_4Al_{13} interface as compared to the α-AlFeSi // Fe_4Al_{13} interface structure. Moreover, virtual shear strength calculations result in a lower shear strength for Fe_2Al_5 // Fe_4Al_{13} than for the α-AlFeSi // Fe_4Al_{13} interface structure.

Keyword Intermetallics; Interfacial properties; UBER; First-principles calculations

1 Introduction

Combining aluminum and steel is becoming increasingly popular in tailored applications including light-weight and strength in complex structures. At the aluminum/steel joint, a micrometer thick layer of Al-Fe intermetallic compounds (IMCs) is typically formed [1]. The presence of these compounds at the joint influences the mechanical properties of the joint. The most common IMCs found at aluminum and steel joints are Fe_2Al_5 (η) and Fe_4Al_{13} (θ) [2–4]. However, the formation of these compounds largely depends on the chemical composition of the alloys and temperature reached during the joining or post-treatment [2, 4].

Together with Fe-Al IMCs, Al-Fe-Si phases have also been observed at such joints [5, 6]. The potential presence of Fe-Al-Si IMCs at the joint depends on the composition of the aluminum alloys, typically seen in 3xxx, 6xxx and foundry alloys. There have been several studies of the thermodynamic and mechanical properties of Fe-Al and Al-Fe-Si systems [7–10].

Most of the investigations of the Fe-Al and Al-Fe-Si IMCs were mainly limited to the bulk structural and mechanical properties. For example, Liu et al. [9] studied the electronic and mechanical properties of Fe-Al binary compounds by ab-initio methods and found Fe_2Al_5 as the thermodynamically most stable of all Fe-Al IMCs. Zhang et al. [11] also studied the structural and mechanical properties of Fe-Al compounds by Embedded-Atom Method (EAM)-based simulations. The most commonly observed IMCs for the Al-Fe-Si system are β-AlFeSi and α-AlFeSi. The β-AlFeSi phase transforms into α-AlFeSi [12]. Several studies have investigated the morphology, contents and transformation kinetics of AlFeSi IMCs [12–14]. All these studies mainly focus on bulk structural and mechanical properties. According to our best knowledge, so far nobody has explored the interfacial characteristics of these IMC//IMC interface structures.

In this work, we study the virtual tensile and shear properties of Fe_2Al_5 // Fe_4Al_{13} and α-AlFeSi // Fe_4Al_{13} interface structures. These interfaces have recently been observed at the cold roll-bonded joint of AA6082 and IF steel [4]. These IMCs have a complex morphology, and it is hard to experimentally predict the influence of an individual IMC on the joint strength. For this reason, an atomistic study is carried out in this work to characterize the interfacial strength of IMC//IMC interfaces. It is worth mentioning that this study is performed without considering any crystallographic defects. Moreover, low lattice misfit and small unit cell size were the selection criteria for these complex IMC//IMC interfaces.

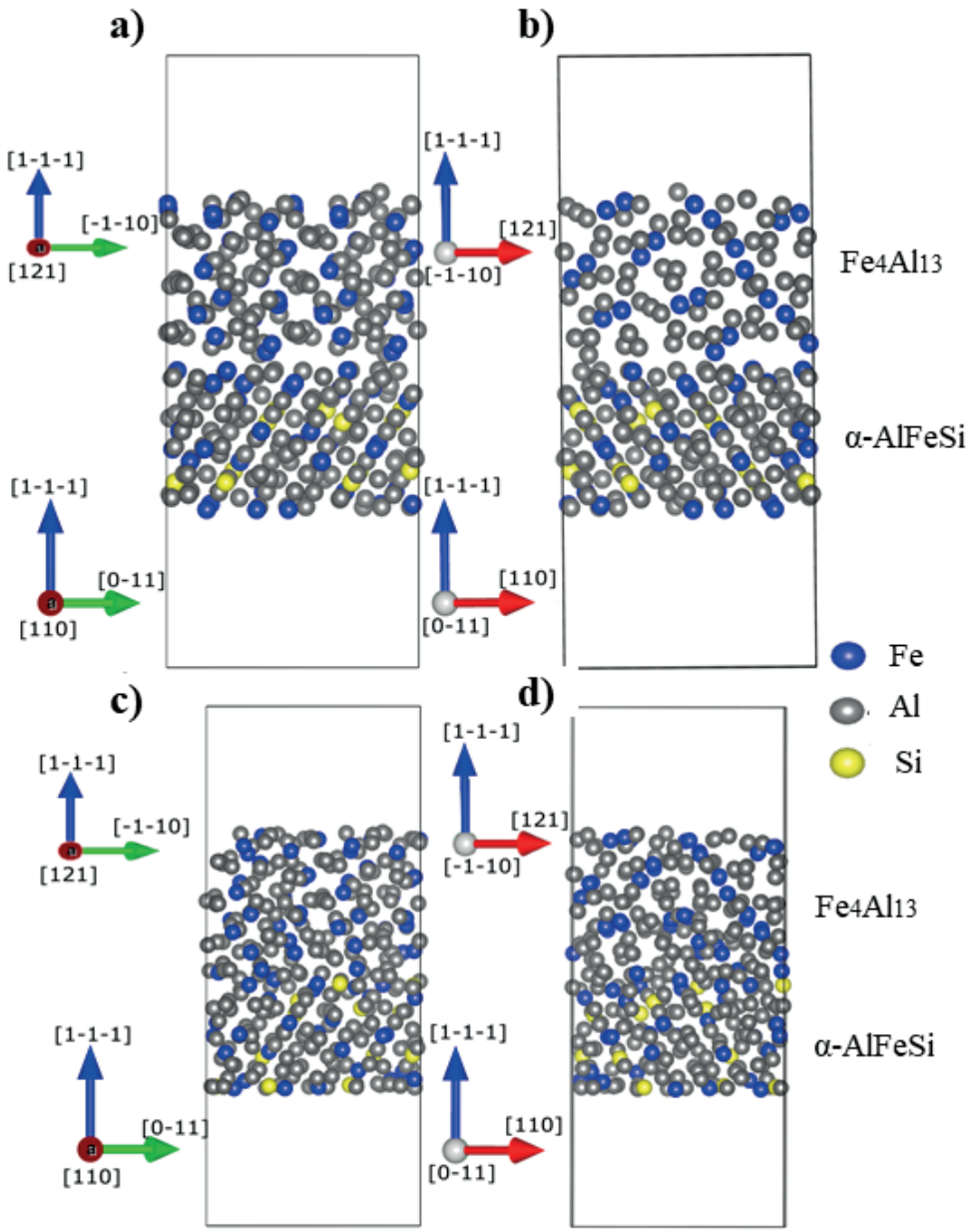

Fig. 1: The interface structures between α-AlFeSi // Fe_4Al_{13}, (a), (b) un-relaxed and (c), (d) DFT-relaxed.

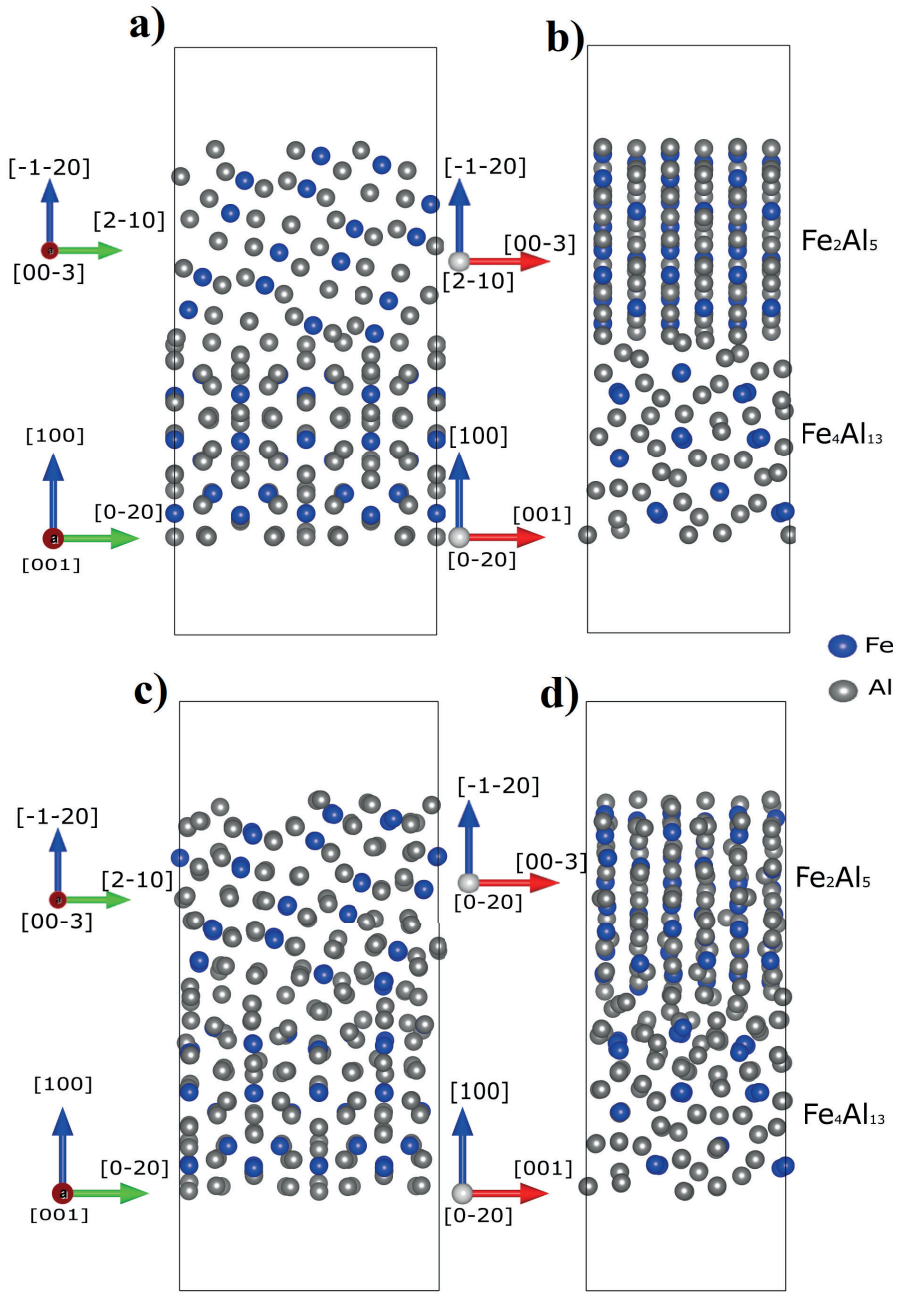

Fig. 2: The interface structures between Fe_2Al_5 // Fe_4Al_{13}, (a), (b) un-relaxed and (c), (d) DFT-relaxed.

Table 1: The ORs and lattice misfit for the IMC // IMC interface structures.

Interface	**d**	m_1	m_2	m_3	length (Å)	angle	n_1	n_2	n_3	length(Å)	angle	strain (%)
Fe_4Al_{13} // Fe_2Al_5	**u**	0	0	1	12.42		0	0	-3	12.29		1.12
	v	0	-2	0	16.05	90.0°	2	-1	0	16.14	90.0°	0.56
	w	1	0	0	-		-1	-2	0	-		-
α-AlFeSi // Fe_4Al_{13}	**u**	1	2	1	17.43		1	1	0	17.76		1.90
	v	-1	-1	0	17.47	121.5°	0	-1	1	17.76	121.5°	1.65
	w	1	-1	1	-		1	-1	-1	-		-

2 Interface models

Due to the large unit cell size and low symmetry of Fe_4Al_{13} (101 atoms, space group 12), α-AlFeSi (138 atoms, space group 204) and Fe_2Al_5 (14 atoms, space group 65), it is extremely challenging to build a representative interface model which has low lattice misfit and contains a low number of atoms. For the building of an interface structure, bulk Fe_4Al_{13} and α-AlFeSi atomic positions were taken from the study published by Liu et al. [15].

To reduce the computational cost and avoid the periodic interaction between two artificial interfaces, a vacuum layer of $>$10 Å was added along the normal direction of the interface. Besides, to ensure the bulk-like interior of phases, a bulk size of $>$ 10 Å was selected for both bulk phases of the interface structures. Fig. 1 and Fig 2 show un-relaxed and DFT-relaxed Orientation Relationships (ORs) and atomic configurations of the Fe_2Al_5 // Fe_4Al_{13} and α-AlFeSi // Fe_4Al_{13} interface structures. Table 1 shows the OR and lattices misfit for both interface structures.

3 Methods

The atomistic simulations were performed with density functional theory implemented in the Vienna Ab-initio Simulation Package (VASP) [16]. The exchange-correlation energy was evaluated using the Generalized Gradient Approximation (GGA) by Perdew, Burke and Ernzerhof (PBE) [17] and with the Projector Augmented Wave (PAW) [18] method for the electron-ion interaction, using standard Al, Fe and Si potentials with three, eight, and four valence electrons, respectively. The k-point integration was performed by using a Monkhorst-Pack grid with a smearing width of 0.2 eV for the first-order Meth-Fessel-Paxton smearing scheme [19]. The plane-wave cut-off energy was set to at least 450 eV in all calculations to ensure that total energies are converged with inaccuracies of less than a few meV/atom.

A major challenge is to relax the atom positions to minimize the total energy of these complex interface structures. To optimize these interfaces a force-based optimization method, FIRE was used [20]. FIRE was found to be surprisingly fast

and efficient for the optimization of these complex interface structures. Since these interfaces have large numbers of degrees of freedom, finding minimum energy paths are computationally expensive. FIRE was in particular found to be successful in finding minimum energy paths due to its ability to stop and steer based on the information of force and velocity. A more detailed description of this method can be found in the literature [20], and it is implemented in VASP [21, 22]. By using the FIRE optimization scheme, the average force per atom was reduced to 0.01 eV/Å^2, and total energy changes were converged to 1 $\times 10^{-5}$ eV. However, for the virtual tensile and shear strength calculations, the conjugate gradient optimization method was used to relax the ionic positions by keeping the cell size fixed.

For the virtual tensile strength calculations, two types of approaches were adopted. In the first approach, interface structures were separated by adding a vacuum at the interface, and static calculations were performed without any atomic relaxations. This approach is denoted Rigid Grain Shift (RGS). In the second approach, interface structures were initially separated in the same way as RGS, then allowed by relaxation of atomic positions to minimize the total energy. Therefore, this approach is denoted RGS+relaxation [23–25]. The energy calculated from these approaches were fitted by a generalized version of UBER proposed by Rose et al. [25, 26];

$$E_b(d) = |E_b^e| \cdot g(a) \tag{1}$$

where $|E_b^e|$ is the binding energy at the equilibrium volume, d is the interface separation and a is the rescaled separation given as $a = d/l$, where l is a characteristic length [25].

To fit the results for IMC interfaces in our virtual tensile tests, we use the following generalized functional form of $g(a)$ [27, 28]

$$g(a) = -(1 + a + P(a))e^{-a-Q(a)} \tag{2}$$

where P and Q are polynomials of order two or larger. This expression for $g(a)$ ensures that $g(0) = -1$, $g(a \rightarrow \infty) = 0$ and $g'(0) = 0$. The first-order terms are excluded from P and Q since they are related to each other as well as to the characteristic length.

By differentiating the binding energy data, the theoretical strength can be obtained,

$$\sigma_{th}(d) = \frac{\partial E_b}{\partial d} \tag{3}$$

The theoretical strength σ_{th} at maximum of its value is defined as the Ultimate

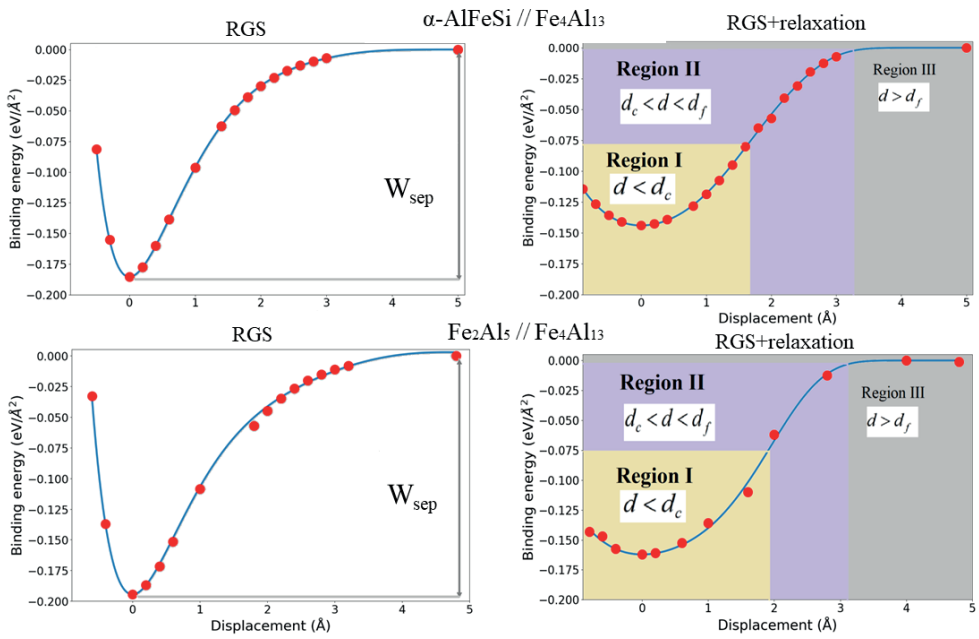

Fig. 3: Energy-displacement curves of the RGS and RGS+relaxation virtual tensile strength calculations for α-AlFeSi // Fe_4Al_{13} and Fe_2Al_5 // Fe_4Al_{13} interface structures. Red points show the DFT calculations data points and blue solid line is the fitted curve using Eqs. (1) and (2).

Tensile Strength (σ_{UTS}) of an interface structure. The value of d at σ_{UTS} is defined as critical length d_c.

4 Results

4.1 Virtual tensile tests

As discussed in Sec. 3, two types of calculations were performed for characterizing the virtual tensile strength, i.e, RGS and RGS+relaxation. These virtual tensile tests result in energy-displacement curves, that are fitted by Eq. (1). For both interface structures, the results of these virtual tensile tests are shown in

Table 2: Calculated ultimate tensile strengths of Fe_2Al_5 // Fe_4Al_{13} and α-AlFeSi // Fe_4Al_{13} interface structures.

Structure	σ_{UTS} (RGS) (GPa)	d_c (Å)	d_f (Å)	$d_{\text{instability}}$ (Å)	σ_{UTS} (RGS+relaxation) (GPa)	W_{sep} (J/m^2)	W_{ad} (J/m^2)
Fe_2Al_5 // Fe_4Al_{13}	17.32	1.97	3.07	1.10	14.48	3.11	2.60
α-AlFeSi // Fe_4Al_{13}	17.79	1.65	3.20	1.55	11.10	2.95	2.31

Fig. 3 for the RGS and RGS+relaxation approaches. The nominal value of the binding energy increases with increasing tensile displacement. W_{sep} is defined as the energy required to separate an interface structure into two rigid bulk surfaces ($-E_b(0)$=W_{sep}) [29]. Table 2 lists the W_{sep} values for both interface structures. W_{sep} for the Fe_2Al_5 // Fe_4Al_{13} interface is higher (0.194 eV/Å^2 = 3.11 J/m^2) than for the α-AlFeSi // Fe_4Al_{13} interface structure (0.184 eV/Å^2 = 2.95 J/m^2). Table 2 also lists σ_{UTS} for both interface structures. The α-AlFeSi // Fe_4Al_{13} interface shows an essentially equal σ_{UTS} (17.79 GPa) to that of the Fe_2Al_5 // Fe_4Al_{13} interface (17.32 GPa).

RGS+relaxation approach provides an opportunity of finding an elastic limit and allows an exploration of the brittleness and ductility of the interface structure. The energy-displacement curve obtained from this methodology is less steep than the RGS curve, and it is harder to find the best fit than with the RGS approach. As Rose pointed out, UBER does not describe well the binding energy versus displacement relationship with the RGS+relaxation methodology for tightly bound metals [30]. For this reason, the functional form of $g(a)$ proposed for this study is given in Eq. (2). Higher-order polynomial terms were taken into account to find the best fit. We also performed some virtual compression tests. To find a good fit for the compression/expansion virtual tensile tests, only odd-order polynomial terms were considered. The best fit found for these interfaces is shown in Fig. 3. The minimum value of the binding energy curve defines the work of adhesion W_{ad} in the RGS+relaxation approach, which is defined as the irreversible work required to separate an interface structure into relaxed surfaces [29].

For the RGS+relaxation virtual tensile tests, the energy-displacement curve is divided into three distinct regions, as shown with three different colors in Fig. 3. Region I is defined as the elastic region ($d < d_c$), where the crack introduced heals during elastic relaxation. This region is described well by Hooke's law. With an increase in tensile displacement, the nominal value of the binding energy increases until the tensile displacement reaches the critical length d_c, where the structure reaches maximum of its tensile strength. Table 2 lists the values of d_c for both interface structures. The Fe_2Al_5 // Fe_4Al_{13} interface has a higher d_c (1.97 Å) than the α-AlFeSi // Fe_4Al_{13} interface (1.65 Å).

Region II is defined as the instability region ($d_c < d < d_f$). In this region, atoms are neither able to heal by elastic relaxations nor are they completely separated into two surfaces. In this region, atoms experience forces from both bulk atoms and try to overcome the energy barrier until the structure is finally separated into two relaxed surfaces at the final fracture length d_f. There is no unique way of determining d_f, but we define the final fracture length as the displacement where the binding energy reaches -0.003 eV/Å^2 [28]. The range of the instability region

is determined by the difference between d_f and d_c ($d_{\text{instability}}$=d_f-d_c).

Materials having a short range of their instability regions tend to show a brittle nature, because they overcome the energy barrier for final fracture abruptly. Fe_2Al_5 // Fe_4Al_{13} showed lower $d_{instability}$ (1.10 Å) than the α-AlFeSi // Fe_4Al_{13} interface (1.55 Å), which indicates a more brittle nature of the former interface than the latter.

Region III is defined as the final fracture zone ($d > d_f$), where the interface structures are completely separated into two relaxed surfaces. In this region, bulk surfaces have no bonding at the interfaces, and the bulk IMCs relax independently. For this reason, the curve levels out. Fe_2Al_5 // Fe_4Al_{13} has higher W_{ad} than the α-AlFeSi // Fe_4Al_{13} interface (See Table 2).

4.2 Tensile strength

Table 2 lists σ_{UTS} for both interface structures. The Fe_2Al_5 // Fe_4Al_{13} interface has a higher value of σ_{UTS} than the α-AlFeSi // Fe_4Al_{13} interface structure. Moreover, the longer range of the instability region of the α-AlFeSi // Fe_4Al_{13} (1.55 Å) interface indicates a less brittle behaviour as compared to the Fe_2Al_5 // Fe_4Al_{13} interface (1.18 Å).

Generally, materials having higher W_{sep} and W_{ad} values have a higher σ_{UTS} value and the same trend has been found in this study. We have compared the W_{sep} values with that of the pure Al // Fe interface [31]. The Al // Fe interface showed a higher value of W_{sep} (5.84 J/m^2) than the α-AlFeSi // Fe_4Al_{13} (2.95 J/m^2) and Fe_2Al_5 // Fe_4Al_{13} (3.11 J/m^2) interfaces, which indicates that the presence of these IMCs at the aluminium and steel joint have detrimental effects on the joint strengths.

4.3 Virtual shear strength

To determine the shear strength, Fe_4Al_{13} and α-AlFeSi phases of the interface structures are shifted along **a** and **b** directions for Fe_2Al_5 // Fe_4Al_{13} and α-AlFeSi // Fe_4Al_{13} interface structures, respectively. The vector direction of **a** and **b** refer to the ORs between the interface structures. During the calculations, atoms were allowed to relax along the normal direction of an interface to remove strain. These calculations result in a energy-displacement curve, which was fitted with a Fourier series,

$$E_s(d) = E_0 + \sum_{n=1}^{\infty}[A_n cos(k_n d) + B_n sin(k_n d)] \tag{4}$$

Table 3: Ideal shear strength of IMC // IMC Interface.

Interface	<001>(GPa)	<020>(GPa)	<110>(GPa)	<011>(GPa)
Fe_2Al_5//Fe_4Al_{13}	5.92	5.15	-	-
α-AlFeSi // Fe_4Al_{13}	-	-	6.81	6.50

where d is the shear displacement, and $E_s(d)$ and E_0 are the energy of the displaced and equilibrium ground state structure, respectively. The periodicity of the structure is defined by λ, and therefore $k_n = \frac{2\pi n}{\lambda}$ (See Appendix Table A1 and A2 for the values of Fourier series coefficients and λ). The shear stress is calculated by differentiating Eq. (4),

$$\gamma_s = \frac{1}{A}\frac{\partial E_s}{\partial d} \tag{5}$$

where A is the unit cell interface area. The first three terms of the Fourier series are used in the fit of the energy-displacement curve. Except for a few outliers, the Fourier series fits nicely. The shear stress-displacement curve obtained from Eq. (5) is shown in Fig. 4.

With an increase in shear displacement, the shear stress increases until it reaches a maximum value, and then it starts to go down again. The shear strength is calculated at the maximum shear value of γ_s. Table 3 lists the shear strength for both interface structures along different slip directions. For the Fe_2Al_5 // Fe_4Al_{13} interface, the $< 020 >$ direction showed a lower shear strength (5.15 GPa) as compared to the $< 001 >$ slip direction (5.92 GPa). α-AlFeSi // Fe_4Al_{13} showed a higher shear strength than the Fe_2Al_5 // Fe_4Al_{13} interface. Moreover, there are no significant differences in shear strength values along $< 110 >$ and $< 011 >$ slip directions.

Overall, these calculations gave indications of a higher shear resistance for the α-AlFeSi // Fe_4Al_{13} interface.

5 Discussion

First-principles calculations were performed to quantify the virtual tensile and shear strengths of the Fe_2Al_5 // Fe_4Al_{13} and α-AlFeSi // Fe_4Al_{13} interface structures. These interfaces have been observed during the welding of aluminum and steel using the cold roll-bonded welding technique [4]. However, it is challenging experimentally to identify the strength of these interfaces due to the small thickness of the joint and the complex nature of the interface structure. This is why we have to resort to a computational approach as in this work.

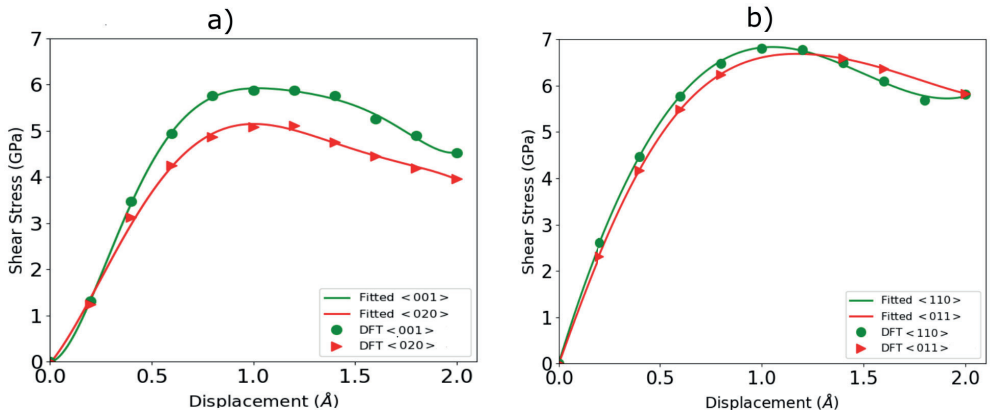

Fig. 4: Fitted shear strength curve of IMC // IMC interfaces between (a) Fe_2Al_5 // Fe_4Al_{13}, and (b) α-AlFeSi // Fe_4Al_{13} interface structures.

The first-principles calculations have shown that the Fe_2Al_5 // Fe_4Al_{13} interface exhibit a higher virtual tensile strength but lower shear strength than the α-AlFeSi // Fe_4Al_{13} interface structure. Moreover, bulk calculations of the Fe_4Al_{13} and Fe_2Al_5 IMCs have indicated that Fe_2Al_5 is a harder phase than Fe_4Al_{13} [10], while α-AlFeSi is found to be softer than Fe_4Al_{13} and Fe_2Al_5. These results indicate that harder phases develop stronger interfacial bonds. In terms of ductility and brittleness, Fe-Al bulk phases were found to be brittle in nature while α-AlFeSi bulk phase showed a ductile nature. However, the α-AlFeSi // Fe_4Al_{13} interface showed more brittle behaviour than the Fe_2Al_5 // Fe_4Al_{13} interface as indicated by the range of the instability region.

Our results contribute to a further understanding of the effects of Fe_2Al_5, Fe_4Al_{13} and α-AlFeSi IMCs have on the joint strength of aluminum and steel. It should be noted, however, that this study does not consider micro-structure effects (dislocations, precipitates, grain boundaries, textures, etc.) and the effect of temperature on mechanical properties. Moreover, the effects of impurities on mechanical strength should also be explored in future work.

6 Conclusions

Virtual tensile and shear calculations were performed on the Fe_2Al_5 // Fe_4Al_{13} and α-AlFeSi // Fe_4Al_{13} interface structures. Virtual tensile calculations were performed using the RGS and RGS+relaxation-based approaches. Virtual tensile strength calculated with the RGS method showed lower σ_{UTS} for the Fe_2Al_5 // Fe_4Al_{13} interface (17.32 GPa) than for the α-AlFeSi // Fe_4Al_{13} interface structure (17.79 GPa). However, the RGS approaches ignore atomic relaxations during

tensile displacement, which leads to over-estimated values of σ_{UTS}. To understand the fracture mechanism, a RGS+relaxation methodology was performed, indicating a higher σ_{UTS} for Fe_2Al_5 // Fe_4Al_{13} (14.48 GPa) and more brittle nature than the α-AlFeSi // Fe_4Al_{13} interface structure. However, virtual shear strength calculations indicated a higher shear strength for the α-AlFeSi // Fe_4Al_{13} interface as compared to the Fe_2Al_5 // Fe_4Al_{13} interface structure.

7 Acknowledgement

The work reported in this paper was based on activities within the centre for research-based innovation SFI Manufacturing in Norway and is partially funded by the Research Council of Norway under contract number 237900. UNINETT Sigma2 AS (The Norwegian Metacenter for High Performance Computing) provided computational resources through Project NN9466K and NN9158K.

8 Appendix

Table 4: The fitting Fourier series coefficient values for the shear strength calculation of Fe_2Al_5 // Fe_4Al_{13} interface.

Polynomial terms	A_0	A_1	A_2	A_3	B_1	B_2	B_3	λ
<001>	6215.51	-8100.5	1845.98	39.01	-4830.22	3446.72	-687.18	39.25
<020>	6215.51	-8100.5	1845.98	39.01	-4830.22	3446.72	-687.18	39.25

Table 5: The fitting Fourier series coefficient values for the shear strength calculation of α-AlFeSi // Fe_4Al_{13} interface.

Polynomial terms	A_0	A_1	A_2	A_3	B_1	B_2	B_3	λ
<110>	-2152.67	-3411.41	8854.29	-3290.28	8160.79	-3958.57	-31.32	192.24
<011>	-2152.67	-3411.41	8854.29	-3290.28	8160.79	-3958.57	-31.32	192.24

References

[1] T. Sakiyama, G. Murayama, Y. Naito, K. Saita, Y. Miyazaki, H. Oikawa, T. Nose, Dissimilar metal joining technologies for steel sheet and aluminum alloy sheet in auto body, Nippon steel technical report 103 (2013) 91–98 (2013).

[2] H. Springer, A. Kostka, J. Dos Santos, D. Raabe, Influence of intermetallic phases and kirkendall-porosity on the mechanical properties of joints between steel and aluminium alloys, Materials Science and Engineering: A 528 (13-14) (2011) 4630–4642 (2011).

[3] L. Xu, L. Wang, Y.-C. Chen, J. D. Robson, P. B. Prangnell, Effect of interfacial reaction on the mechanical performance of steel to aluminum dissimilar ultrasonic spot welds, Metallurgical and Materials Transactions A 47 (1) (2016) 334–346 (2016).

[4] S. M. Arbo, T. Bergh, H. Solhaug, I. Westermann, B. Holmedal, Influence of thermomechanical processing sequence on properties of AA6082-IF steel cold roll bonded composite sheet, Procedia Manufacturing 15 (2018) 152–160 (2018).

[5] S. Kobayashi, T. Yakou, Control of intermetallic compound layers at interface between steel and aluminum by diffusion-treatment, Materials science and engineering: A 338 (1-2) (2002) 44–53 (2002).

[6] A. Kurakin, Mechanism of the influence of silicon on the processes of the reaction diffusion of iron in aluminium, Physics of Metals and Metallography (Fiz. Metal. Metalloved.) 30 (1) (1970) 105–110 (1970).

[7] L. Amirkhanyan, T. Weissbach, T. Gruber, T. Zienert, O. Fabrichnaya, J. Kortus, Thermodynamic investigation of the τ_4-Al-Fe-Si intermetallic ternary phase: A density-functional theory study, Journal of Alloys and Compounds 598 (2014) 137–141 (2014).

[8] T. Klaver, G. Madsen, R. Drautz, A dft study of formation energies of Fe-Zn-Al intermetallics and solutes, Intermetallics 31 (2012) 137–144 (2012).

[9] Y. Liu, X. Chong, Y. Jiang, R. Zhou, J. Feng, Mechanical properties and electronic structures of Fe-Al intermetallic, Physica B: Condensed Matter 506 (2017) 1–11 (2017).

[10] M. Z. Khalid, J. Friis, P. H. Ninive, K. Marthinsen, A. Strandlie, DFT calculations based insight into bonding character and strength of Fe_2Al_5 and Fe_4Al_{13} intermetallics at Al-Fe joints, Procedia Manufacturing 15C (2018) 1407–1415 (2018).

[11] C.-H. Zhang, S. Huang, J. Shen, N.-X. Chen, Structural and mechanical properties of Fe-Al compounds: An atomistic study by EAM simulation, Intermetallics 52 (2014) 86–91 (2014).

[12] H. Becker, T. Bergh, P. Vullum, A. Leineweber, Y. Li, Effect of mn and cooling rates on α-, β-and δ-Al-Fe-Si intermetallic phase formation in a secondary al–si alloy, Materialia 5 (2019) 100198 (2019).

[13] N. C. Kuijpers, F. J. Vermolen, K. Vuik, S. van der Zwaag, A model of the β-AlFeSi to α-Al (FeMn) Si transformation in Al-Mg-Si alloys, Materials Transactions 44 (7) (2003) 1448–1456 (2003).

[14] J. M. Sanchez, I. Vicario, J. Albizuri, T. Guraya, J. C. Garcia, Phase prediction, microstructure and high hardness of novel light-weight high entropy alloys, Journal of Materials Research and Technology 8 (1) (2019) 795–803 (2019).

[15] P. Liu, G. Dunlop, Crystallographic orientation relationships for Al-Fe and Al-Fe-Si precipitates in aluminium, Acta Metallurgica 36 (6) (1988) 1481–1489 (1988).

[16] G. Kresse, J. Furthmüller, Vienna ab-initio simulation package (VASP), Vienna: Vienna University (2001).

[17] J. P. Perdew, K. Burke, M. Ernzerhof, Generalized gradient approximation made simple, Physical Review Letters 77 (18) (1996) 3865 (1996).

[18] P. E. Blöchl, Projector augmented-wave method, Physical review B 50 (24) (1994) 17953 (1994).

[19] H. J. Monkhorst, J. D. Pack, Special points for brillouin-zone integrations, Physical review B 13 (12) (1976) 5188 (1976).

[20] E. Bitzek, P. Koskinen, F. Gähler, M. Moseler, P. Gumbsch, Structural relaxation made simple, Physical review letters 97 (17) (2006) 170201 (2006).

[21] D. Sheppard, R. Terrell, G. Henkelman, Optimization methods for finding minimum energy paths, The Journal of chemical physics 128 (13) (2008) 134106 (2008).

[22] D. Sheppard, R. Terrell, G. Henkelman, Force based optimizers (2008). URL http://theory.cm.utexas.edu/vtsttools/optimizers.html

[23] D. Zhao, O. M. Løvvik, K. Marthinsen, Y. Li, Segregation of Mg, Cu and their effects on the strength of Al $\sigma 5$ (210)[001] symmetrical tilt grain boundary, Acta Materialia 145 (2018) 235–246 (2018).

[24] P. Lazar, R. Podloucky, Cleavage fracture of a crystal: Density functional theory calculations based on a model which includes structural relaxations, Physical Review B 78 (10) (2008) 104114 (2008).

[25] R. Janisch, N. Ahmed, A. Hartmaier, Ab initio tensile tests of Al bulk crystals and grain boundaries: Universality of mechanical behavior, Physical Review B 81 (18) (2010) 184108 (2010).

[26] J. H. Rose, J. R. Smith, J. Ferrante, Universal features of bonding in metals, Physical review B 28 (4) (1983) 1835 (1983).

[27] I. J. Jensen, J. Friis, C. D. Marioara, I. G. Ringdalen, The role of grain boundary precipitates during intergranular fracture in 6XXX series Aluminium alloys, In preparation.

[28] M. Z. Khalid, J. Friis, P. H. Ninive, K. Marthinsen, A. Strandlie, Ab-initio study of atomic structure and mechanical behaviour of Al/Fe intermetallic interfaces, Accepted in Computational Materials Science (2019).

[29] R. Yang, S. Tanaka, M. Kohyama*, First-principles study on the tensile strength and fracture of the Al-terminated stoichiometric α-Al_2O_3 (0001)/Cu (111) interface, Philosophical Magazine 85 (25) (2005) 2961–2976 (2005).

[30] E. A. Jarvis, R. L. Hayes, E. A. Carter, Effects of oxidation on the nanoscale mechanisms of crack formation in aluminum, ChemPhysChem 2 (1) (2001) 55–59 (2001).

[31] M. Z. Khalid, J. Friis, P. H. Ninive, K. Marthinsen, A. Strandlie, A First-Principles Study of the Al (001)/Fe (0-11) Interface, in: Materials Science Forum, Vol. 941, Trans Tech Publ, 2018, pp. 2349–2355 (2018).

Paper A

Khalid MZ, Friis J, Ninive PH, Marthinsen K and Strandlie A,"A First-Principles Study of the Al (001)/Fe(0-11) Interface," *Materials Science Forum,* vol. 941, 2018.

Appendix A

A First-Principles Study of the Al (001)/Fe(0-11) Interface

Khalid M. Z., Friis J., Ninive P. H., Marthinsen K. Strandlie A.

Abstract

Using a first-principles methodology we have investigated the interfacial and bonding characteristics of the Al(001)/Fe (0-11) interface. The Al/Fe interface model was developed using a face-to-face matching method. Among many possible interface structures, the Al (001)/ Fe(0-11) orientation relation gave the minimum lattice misfit along the a and b directions (a=b= -0.47%). Hence, this interface structure provided the minimum energy value and was used for this study. To predict the interface strength and stability, the work of separation and interfacial energy were calculated. Here, all systems were calculated under exactly the same conditions (k-point mesh, cutoff energy, lateral lattice strain etc). In order to predict the bonding nature at the interface, charge density difference plot was evaluated, which showed charge gain at the interface. The aim of this study is to describe the adhesive behavior between Al and Fe, provide some insights about strength and stability of this interface structure for galling, and provide reference interface system for Al/Fe welding.

Keyword Density functional theory; galling; Al-Fe welding; Interface energy; work of separation